Surface Deformation Analysis of the Houston Area: Investigating Contributions of Faults, Salt Domes, and Major Storms.

A Thesis Presented to the

Department of Earth and Atmospheric Sciences

University of Houston

In Partial Fulfillment

of the Requirements for the Degree

Master of Science

By

Wanda E. Crupa

August 2019

Surface Deformation Analysis of the Houston Area: Investigating Contributions of Faults, Salt Domes, and Major Storms.

_____

Wanda E. Crupa

APPROVED:

_____

Dr. Shuhab D. Khan, Chairman

_____

Dr. John Suppe

_____

Dr. Jiajia Sun

_____

Dr. Ning Cao

_____

Dr. Dan E. Wells, Dean, College of Natural Sciences and Mathematics

ACKNOWLEDGEMENTS

This study would like to thank Chris Florescu for his help with MATLAB, Python, and general programming. We also thank the GEORS Remote Sensing Laboratory at the University of Houston for their comments, insight, and support.

Surface Deformation Analysis of the Houston Area: Investigating Contributions of Faults, Salt Domes, and Major Storms.

A Thesis Presented to the

Department of Earth and Atmospheric Sciences

University of Houston

In Partial Fulfillment

of the Requirements for the Degree

Master of Science

By

Wanda E. Crupa

August 2019

ABSTRACT

The Houston area has undergone significant ground deformation in the last century, with the main factor being attributed to groundwater/natural gas withdrawal. However, subsidence can be due to groundwater withdrawal or excess loading brought about by heavy precipitation. Houston has recently been subjected to multiple flooding events which appear to be increasing in frequency. The Houston area is also home to faults and salt domes that contribute to surface deformation. The effect that these factors have had on ground deformation has not previously been studied; certain components of ground motion have been misinterpreted, or largely ignored in scientific studies and when making policies.

In this study we investigate the contributions of surface and groundwater to subsidence using data collected over the past 30 years to model/predict groundwater fluctuations and look at the correlation with faults/salt domes and GPS data to see how surface deformation patterns have changed in recent years. The high rate of salt motion coupled with CO_2 injection has resulted in uplift in southern Harris County, which acts to alleviate groundwater/gas withdrawal induced subsidence. Observed fault motion along the Long Point-Eureka Heights system is correlated with groundwater trends from 2006-20107. The northern Houston area shows strong subsidence of up to 16 mm/yr and an elongated subsidence bowl. The weakened aquifer systems in the north and southwest are more susceptible to intense subsidence and major flooding. These trends may be matched in the Woodlands and southwest Harris County in the future.

TABLE OF CONTENTS

LIST OF FIGURES

LIST OF TABLES

LIST OF EQUATIONS

Chapter 1: Introduction

1.1. Geologic Setting

The Houston area has undergone significant ground deformation in the last century, with the main factor being attributed to groundwater and natural gas withdrawal. However, the observed surface deformation is not purely anthropogenic in origin, with many geologic factors, such as faults and salt domes, playing a contributing role. During the Triassic period, the Gulf of Mexico experienced extensional rifting, which was followed by seafloor spreading in the middle Jurassic (Salvador, 1991; Bird et al., 2005). Large salt deposits also accumulated in this region in the late Triassic and Jurassic (Kupfer, 1974). Then throughout the Cretaceous and Cenozoic periods, deposition resulted in a prograding shelf margin. This series of events resulted in multiple growth faults across the Gulf Coast Region, most of which occur near the prograding shelf margin, and which divide the area into structural corridors (Winker, 1985). The Houston area is situated over three primary growth fault zones: 1) Hockley-Conroe Fault System, 2) Addicks Fault System, and 3) the Long Point-Eureka Heights Fault System (Figures 1 and 2). These faults cut through Holocene and Paleocene sediments and primarily move through aseismic creep, resulting in both spatial and temporal variation (Mastroianni, 1991; Englekemeir et al., 2010). The large salt deposits of the past have resulted in modern salt domes, which due to their low density, rise to the surface and fracture the surrounding regions in radial patterns (Khan et al., 2014).

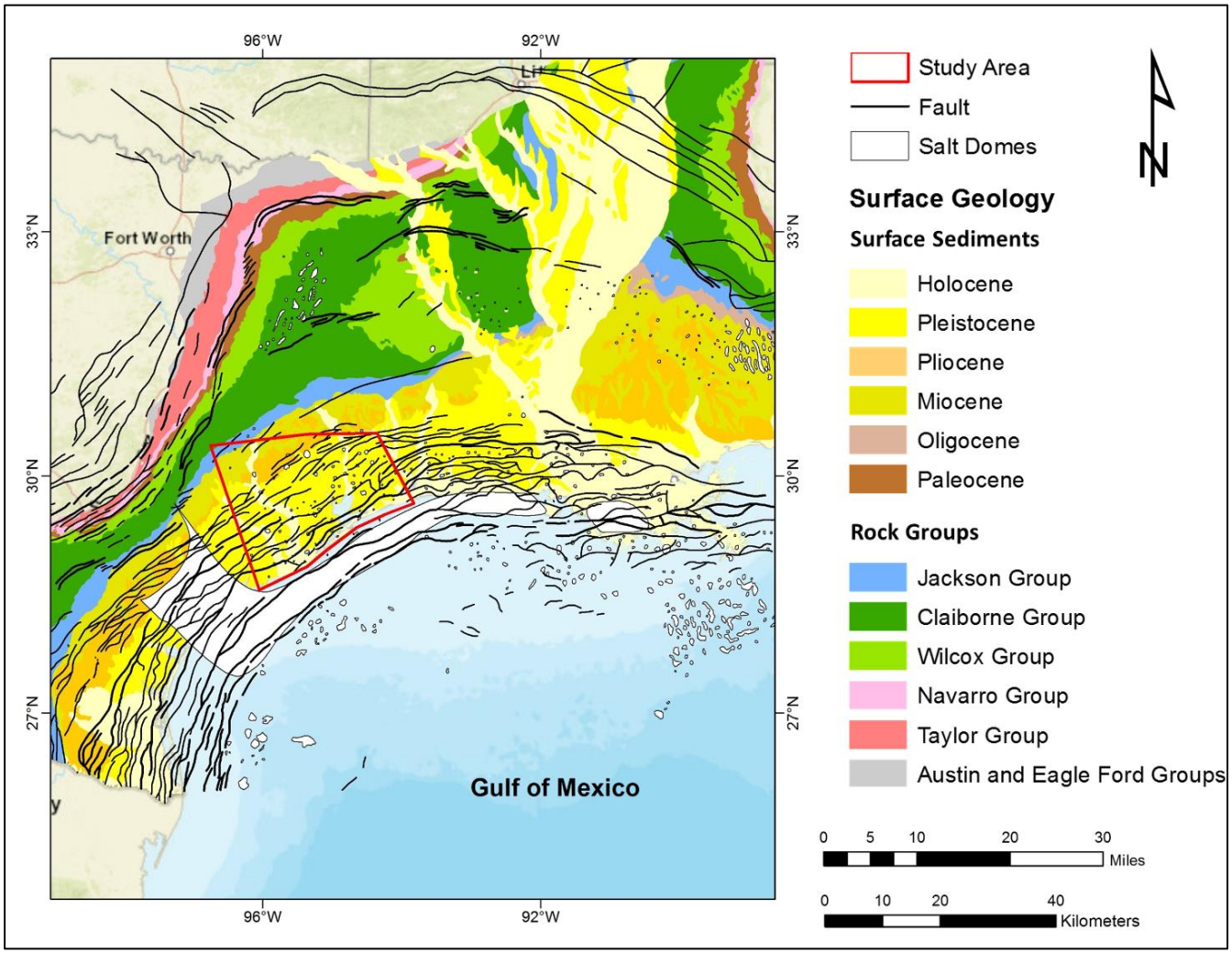

Figure 1: Regional faults in the Gulf Coast Region over surface geology, study area shown by a yellow polygon. Data courtesy of AAPG. Modified from Pitman, J. K. (2010). Reservoirs and petroleum systems of the Gulf Coast.

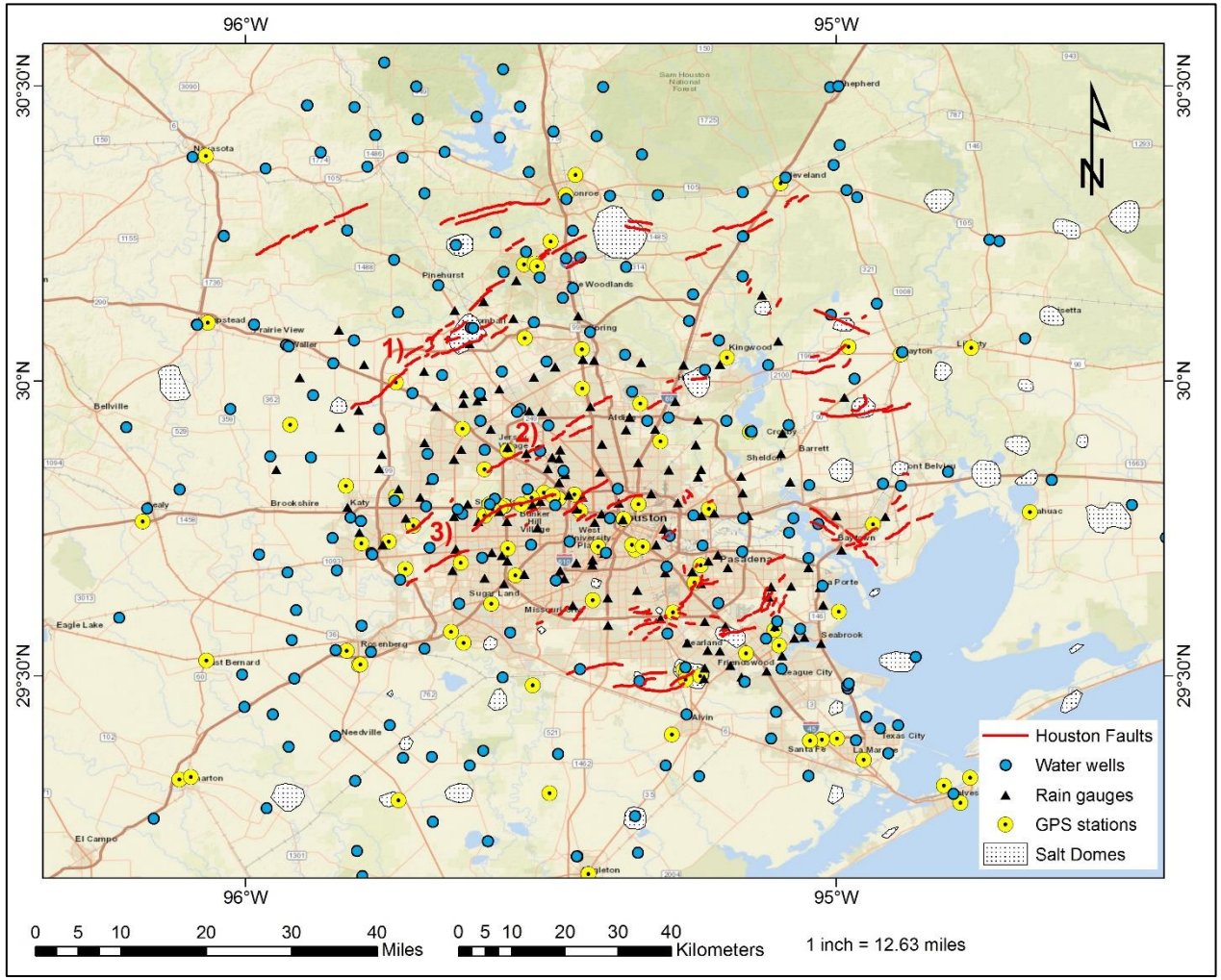

Figure 2: Map of Houston area fault and salt domes where 1) Hockley-Conroe Fault System, 2) Addick's Fault System, and 3) the Long Point-Eureka Heights Fault System. Faults associated with salt domes show radial patterns.

1.2. Subsidence

The Houston area has experienced some of the largest subsidence of any city, losing over 10 feet in elevation in certain areas from 1927-present (Kasmarek et al., 2009; Kasmarek, 2012; Kearns et al., 2015). There are two primary causes for ground subsidence that deal with ground and surface water respectively: 1) excessive water withdrawal, and 2) sediment compaction caused by an increased load (Kreitler, 1977; Galloway et al., 1999). The Houston area relies on alluvial aquifers made up of semi-consolidated silt, clay, and sand layers (aquitard) for its main water supply. As water levels decrease in these aquifer systems, the fluid pressure in the pores and cracks that make up the aquitard also decreases as they become filled with air. The air-filled pores/cracks reduce the strength of the aquifer skeletal system and cause surface deformation (Kreitler, 1977; Galloway et al., 1999). Under normal conditions, aquifer systems will only experience seasonal variation and cause reversible surface deformation on the scale of 1-5 cm (Galloway et al., 1999). However, excessive groundwater decline causes a drastic reduction in fluid pressure, where the now weakened skeletal system becomes compressed. This can result in a permanent reduction of porosity, the aquifer storage capacity, and non-reversible ground deformation (Galloway et al., 1999). The increased load is caused by the addition of extra weight above the aquifer system, as caused by heavy snow or rain precipitation. If this overhead weight remains under the maximum loading capacity previously experienced by the aquifer, it will only cause reversible seasonal variation (Galloway et al., 1999). Similarly, if the overhead weight exceeds this maximum value, there will be a permanent reduction in porosity, storage capacity, and the deformation will be non-reversible (Galloway et al., 1999).

Houston's subsidence has been primarily due to groundwater, where fluids are also thought to have reactivated and amplified fault movement (Kasmarek, 2012; Qu et al., 2015). While much less common than water withdrawal, increased load poses a real threat to the city's welfare as

exemplified by the 2016 Memorial Day floods and the 2017 hurricane Harvey. The additional water released by both events resulted in increased loading, whose effects on subsidence are still being evaluated. Unfortunately, precipitation data needed to assess the impact of increased loading lacks the temporal coverage of groundwater data, is far more limited due to incomplete records (and occasionally damaged gauges) and is more challenging to model. This has resulted in surface water often getting overlooked as a contributor to observed subsidence and a poor understanding of the environmental impact in the area. In this study we investigate the contributions of surface and groundwater to subsidence using potentiometric water surfaces to model and predict groundwater fluctuations in the Houston Area collected over the past 30 years, and look at the correlation with rainfall and GPS data subsidence rates to see how surface deformation patterns have changed in recent years over the Houston area. In addition, we also examine the flooding related to the 2017 Hurricane Harvey.

1.3. Hurricane Harvey

Hurricane Harvey struck the Texas coast on August 25, 2017, as a category 4 hurricane with winds above 150 miles per hour (Blake and Zelinsky, 2017; Watson et al., 2018). As the storm moved inland, it slowed considerably which allowed for an unprecedented level of rainfall during its 8-day trek. Historic flood levels were recorded across Southeast Texas, with some areas experiencing over 60 inches of rainfall. Hurricane Harvey was recorded as the most significant rainfall event in US history since the start of the 1880 rainfall records (Watson et al., 2018). The total wind and flood damage are estimated to be $125 billion with at least 68 direct casualties being linked to the storm. The worst flooding was recorded in Houston, Texas, a city previously notorious for large-scale subsidence (Kearns et al., 2015; Blake and Zelinsky, 2017; Watson et al., 2018). Since the 1900s, losses of up to 3 m in elevation have been reported in the city of Houston, due mainly to over-pumping of groundwater (Kasmarek

et al., 2009; Kasmarek, 2012; Kearns et al., 2015). This severe subsidence has increased the probability of flooding and created a negative feedback loop in affected areas. As flooding occurs, the overbearing weight of floodwater acts to compress sediments in the subsurface (Kreitler, 1977; Galloway et al., 1999; Kasmarek and Lanning-Rush, 2004). A healthy environment is elastic and will be able to spring back up after compaction. Areas that have undergone subsidence lack this quality; flooding will thus aid in further compacting the soil and drive subsidence (Kreitler, 1977). Flooding and subsidence are highly correlated, as has been shown by Milliner et al., 2018; this relationship necessitates accurate flood mapping.

Both during and following Harvey, multiple organizations such as the U.S. Geological Survey (USGS) and the Federal Emergency Management Agency (FEMA) set out to map the flooding extent, calculate the flood magnitude, and determine the probability of flood occurrence (Watson et al., 2018). Primary data for such studies include 74 streamflow-gaging stations, 34 National Oceanic and Atmospheric Administration (NOAA) meteorological stations, and in-situ high-water mark measurements located throughout Southeast Texas. However, the in-situ stations themselves were also affected by the storm with multiple failures being recorded across the station networks. At least 12 rain gauge stations were identified to have recorded erroneous data in the August report (Blake and Zelinsky, 2017; Watson et al., 2018; Harris County Flood Control District).

Additionally, while in-situ measurements in the form of high-water marks provide much needed data, they are slow to collect and generally lack a proper spatial distribution. High-water mark data are also a cumulative measurement that only shows the maximum water level. These data are unable to show any temporal variation associated with flooding events (Watson et al., 2018). Furthermore, most efforts are directed towards mapping the flooding associated with/or near rivers. However this approach ignores the floods associated with

urban environments, where poor drainage due to an abundance of impermeable surfaces is common.

Synthetic Aperture RADAR (SAR) is a spaceborne remote sensing technique that is ideal for mapping large areas and detecting water bodies. SAR data are unaffected by flooding conditions at the surface, and unlike optical techniques, it can readily penetrate through storm clouds and acquire data even during nighttime conditions (Kasischke et al., 1997; Giustarini et al., 2012). An additional benefit is the ability of SAR data to penetrate through the tree canopy and detect returns that would otherwise be hidden by vegetation, which is important to flood mapping where determining the amount of flooded vegetation can be a major challenge (Wegmuller and Werner, 1995; Kasischke et al., 1997; Giustarini et al., 2012). Moreover, the high temporal resolution of SAR data allows for additional information on floods, such as drainage patterns to be detected (ESA Online). The recent improvements in land coverage, data availability, and revisit frequency (6 days for Sentinel-1) of SAR data have shown its potential for land use mapping and natural hazard monitoring (Kasischke et al., 1997). Fully polarimetric radar data can readily distinguish between different endmembers; however, the limited availability of fully polarized datasets does not make their use common (Kasischke et al., 1997).

This work focuses on mapping simple land use maps following Hurricane Harvey in 2017 to assess the flooding using single polarized data. Output maps are divided into the following classes: 1) urban areas, 2) bare soil, 3) water, 4) vegetation, 5) flooded areas, and 6) flooded vegetation. This is done by obtaining a false color composite images made up of RGB: coherence, the mean backscatter, and the backscatter difference between a SAR image pair as described by Kasischke et al., 1997.

1.4. Synthetic Aperture Radar

1.4.1. Radar Background

In remote sensing applications, radar (**RA**dio **D**etection **A**nd **R**anging) uses wavelengths spanning the microwave region to image the Earth's surface actively. A radar wave can be described by the standard wave equation shown below where *A* is the wave amplitude, *Φ* (phi) is the phase, and *t* is the travel time (Kasischke et al., 1997; Henderson and Lewis, 1998).

Equation 1: (Wave Equation) $A*exp(\Phi t) = A*[cos(\Phi t) + i*sin(\Phi t)]$

The wave is described by both real and imaginary parts using the cos and sin function, respectively to capture the full energy spectrum. The amplitude and phase both change according to the surface target properties and can thus be used to identify the target, travel-time, and target range, as shown below (Figure 3).

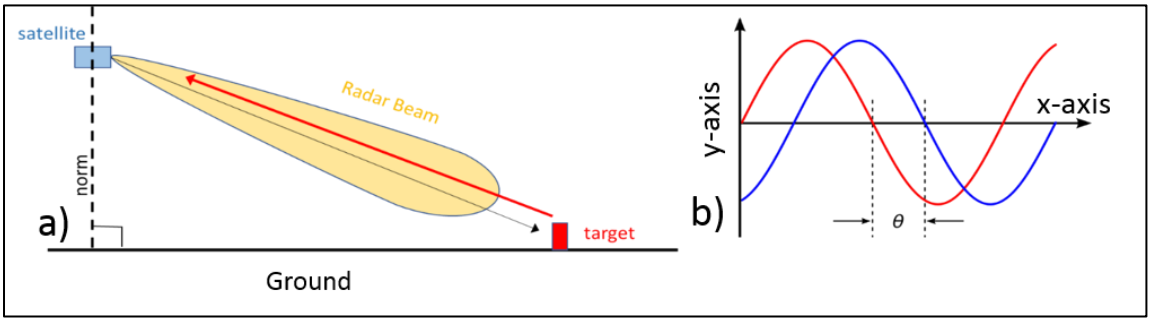

Figure 3: From right to left, ***a)*** *cross-section view of satellite imaging a target where the black arrow is the outgoing ray and red arrow is the incoming ray with changed amplitude and phase;* ***b)*** *example of phase change in cosine wave where the x-axis is time and the y-axis is amplitude. The change in phase can be correlated to a 2-way travel time (2WTT) and a distance/range to the target.*

Unlike most satellites, Synthetic Aperture Radar (SAR) is side-looking (Figure 3a), which results in stronger/brighter returns for rough surfaces with low dielectric constants (non-conductive materials). However, this geometry can lead to issues such as shadow, foreshortening, and

layover (Kasischke et al., 1997; Henderson and Lewis, 1998). The primary cause of noise in satellite radar imagery is speckle, which is caused by the constructive and destructive interference of sub-pixel targets. Speckle gives a 'salt-and-pepper' look, reduces the contrast in the image, and alters the observed radar backscatter.

There are 4 primary types of scatter as shown in Figure 4: 1) point – from a single point source, 1) specular/surface – from a flat surface, 3) volume – from multiple point sources, and 4) double bounce/dihedral – when the ray bounces off multiple surfaces (Kasischke et al., 1997; Henderson and Lewis, 1998). The type of scatter is depended on the satellite/target(s) geometry and the intrinsic properties of the material, which can change through time. Certain targets can change the direction/polarization of the RADAR wave, resulting in volume and double-bounce/dihedral scatter.

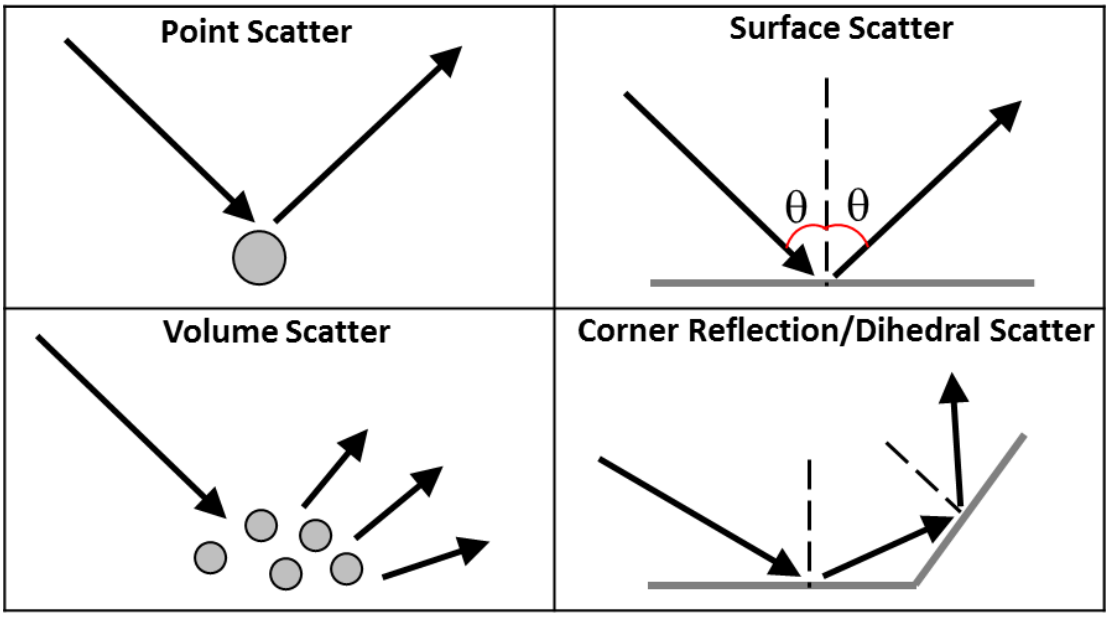

Figure 4: Types of scattering. Modified from https://earth.esa.int/handbooks/asar/CNTR1-1-2.html.

1.4.2. Radar Mapping

A common approach to natural hazard mapping with SAR data is to use a gray-threshold technique. Using two or more images, one before the incident known as the archive image and another taken either during or post the incident known as the crisis image, the gray-threshold technique creates a false color composite (Kasischke et al., 1997; White et al., 2015). When a natural hazard strikes, such as a flood, the backscatter becomes significantly altered in the affected areas. For example, flooded areas not obscured by vegetation or buildings will change to the scattering mechanism to specular reflectance and have decreased brightness. The abrupt change in backscatter can be used to define a threshold that delineates the affected areas. The affected area can then be estimated by multiplying the number of pixels by the pixel size (Kasischke et al., 1997; Martinis and Rieke, 2015; White et al., 2015). This technique is currently used by the Dartmouth Flood Observatory and the Advanced Rapid Imaging and Analysis (ARIA) team at NASA's Jet Propulsion Laboratory for global food monitoring. Milliner et al., 2018 have also used the gray-threshold to delineate the flooded extent of Hurricane Harvey.

While the gray-threshold technique is rather simplistic, it is widely used because of its computational efficiency and high effectiveness over simple targets. However, because of intrinsic variation between the images due to temporal decorrelation, geometric decorrelation, volume scattering, and processing errors, the gray-threshold technique may not successfully identify all pixels of interest (Kasischke et al., 1997; Shen et al., 2019). The threshold value is also user dependent and does not have strict rules. Moreover, this approach only gives users a measure of the intensity change, but no other information regarding the surface targets (White et al., 2015; Shen et al., 2019). It is primarily up to the user to interpret what is causing the change in backscatter using outside information, which may not always be available.

A more effective technique for SAR mapping would be to use fully polarimetric data (Kasischke et al., 1997; Henderson and Lewis, 1998; Lee and Pottier, 2009; White et al., 2015). Polarization is used to describe the way in which an electromagnetic wave oscillates as it travels. A vertically polarized (V) wave oscillates up and down as it moves forward, whereas a horizontally polarized (H) wave oscillates from side to side. Both vertically and horizontally polarized waves are said to have linear polarization (Lee and Pottier, 2009). There are four possible polarization combinations, HH, HV, VV, and VH, where HH, VV are called co-polarized, and HV,, VH are called cross-polarized. The different polarization modes can be thought of as the wavelength equivalent of multispectral data; fully polarized (having all four polarization modes) datasets can be used for in-depth textural analysis and identification/classification of end-members (Henderson and Lewis, 1998; Lee and Pottier, 2009). Unlike the gray-threshold method, polarimetric techniques do not require multiple images for target identification and classification (Lee and Pottier, 2009). However, the limited availability of fully polarized datasets does not make their use common. Instead, similar information may be extracted from two or more single polarized images using the backscatter and coherence changes (Kasischke et al., 1997).

The correlation of two images is called the coherence image, and it is a measure of how well related features are across the image pair, where the reference image (the older image) is known as the master and the comparative image (the younger image) is known as the slave (Henderson and Lewis, 1998; Chini et al., 2019). Areas of bare soil and urban areas, such as buildings or bridges, experience little motion and are typically stable over long periods. This behavior is called coherent, and it allows these features to be readily identified across multiple images, even if the images are taken years apart (Xia and Henderson, 1997; Henderson and Lewis, 1998; Chini et al., 2019; Li et al., 2019). Bare soil and urban areas are stable and thus have very high coherence, while features like vegetation and water, which change rapidly, have poor

coherence (Wegmuller and Werner, 1995; Xia and Henderson, 1997; Chini et al., 2019). A typical scene is made up of 1) water, 2) vegetation, 3) bare soil, and 4) urban areas. Each of these components has a distinct scatter type, return brightness, and coherence as summarized below in Table 1. Traditionally, the SAR coherence has been for urban mapping with over 95% accuracy, however recent work has shown its potential for food mapping in complex environments such as urban or vegetated areas (Chini et al., 2019; Li et al., 2019). The change in backscatter experienced by flooded areas is highly dependent on the SAR satellite and target geometry; subtle changes in backscatter associated with natural hazards are hard to identify which can lead to under detection in complex environments. Integrating both backscatter changes and coherence into a detection/classification scheme allows for detection of subtle features using a self-consistent approach (Kasischke et al., 1997; Chini et al., 2019).

Table 1: Summary of scatter, brightness, and coherence for common materials.

Material	Scatter Type	Return Brightness	Coherence
Water	Bragg/surface	Low	Low
Vegetation	Volume	High	Low
Bare Soil	Surface	Low	High
Urban Area	Dihedral/double-bounce	High	High
Flooded Area	Bragg/surface	Low	Low
Flooded Vegetation	Volume/Dihedral	High	Low

1.4.3. Sentinel-1

The Sentinel-1 mission is the joint effort of the European Commission (EC) and the European Space Agency (ESA). The mission is a constellation of two polar-orbiting satellites that share the same orbital plane, Sentinel-1A and Sentinel-1B, which provide continuous radar coverage of the Earth (ESA Online). Sentinel-1A was launched on April 3, 2014, with Sentinel-1B closely following on April 25, 2016 (Potin et al., 2016). The satellites operate in C-band frequency (central frequency of 5.405 GHz) and support dual polarization of either HH+HV or VV+VH through a switchable transmit chain (Torres et al., 2012). Sentinel-1 operates in 4 possible acquisition modes: stripmap (SM), interferometric wide-swath (IW), Extra-Wide swath (EW), and Wave mode (WV). The SM mode consists of a high-resolution (5x5 m) narrow swath that is similar to previous ERS and Envisat missions (Torres et al., 2012). The IW mode is comprised of three sub-swaths with resolution ranging from 5-20 m, which are acquired in Terrain Observation with Progressive Scans SAR (TOPSAR) mode. In TOPSAR mode the radar beam is steered both in range along the azimuth of each burst (Meta et al., 2008). The EW mode is similar to IW but is comprised of 5 sub-swaths rather than 3. The WV mode is designed for ocean applications and can determine the direction, wavelength, and height of waves on the ocean's surface (Torres et al., 2012).

Chapter 2: Methods

2.1 Water Data

To evaluate changes in water table this study implemented data from 144 rain gauges from 2011-2016 part of the Harris County Flood Warning System (FWS) and well-water depth from 268 stations from January, 1990 – March, 2017 from the Advisory Committee on Water Information (ACWI), Texas Water Development Board (TWDB), the National Ground-Water Monitoring Network (NGWMN), and the United States Geological Society (USGS) (Figure 2). By comparing surface and groundwater, we can directly observe if subsidence is related to increased loading or groundwater withdrawal.

Potentiometric surfaces were generated and used to calculate water level change and to visualize the areas most affected by water withdrawal and increased loading. Water data were first compiled into an Oracle database for easy sorting and grouped based on the year and season of acquisition to provide enough points for spatial interpolation. Data were then imported into ArcMap and potentiometric surfaces were generated for each season (spring, summer, fall, and winter) from winter 1990 to spring 2017. Interpolation was carried out using the ordinary Kriging interpolation with a variable search radius and 20 input points. Average seasonal groundwater level and average rain were then calculated to serve as baselines for ground and surface water levels, respectively (Figures 5 and 6). The potentiometric surfaces were then used to generate a time-series analysis and determine the total water level change in from 1) 1990-2017, 2) 2000-2017, and 3) 2006-2017. Figure 7c from 2006-2017 shows the best correlation with the recent GPS data as expected; hence this relationship was further analyzed.

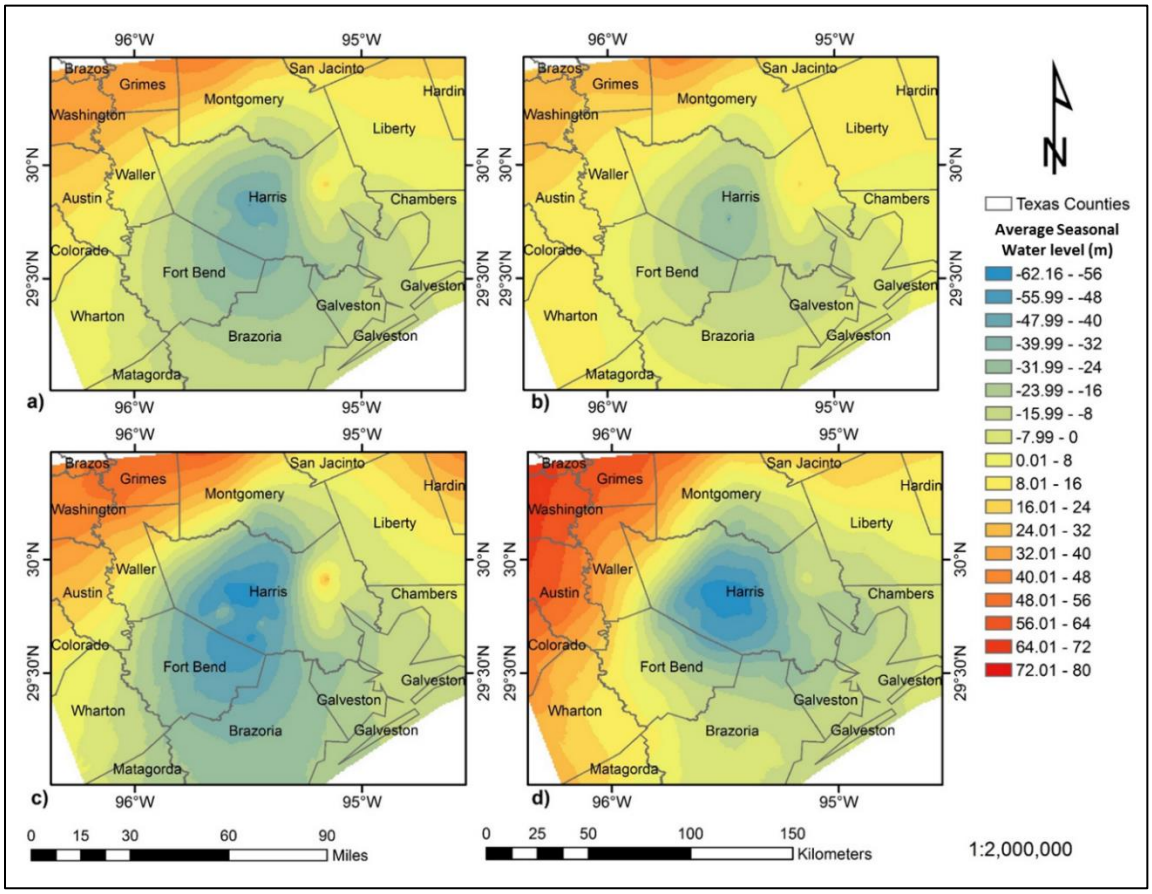

Figure 5: Seasonal water table trends for the Houston area showing the area of constant low water level in the center of Harris County associated with the city of Houston. a) Spring season showing the moderately sized area of low water level. b) Summer season showing the smallest area of low water level as most rain occurs during the summer months, c) Fall season showing the largest area of low water level, d) Winter season showing the enlarged area of low water level.

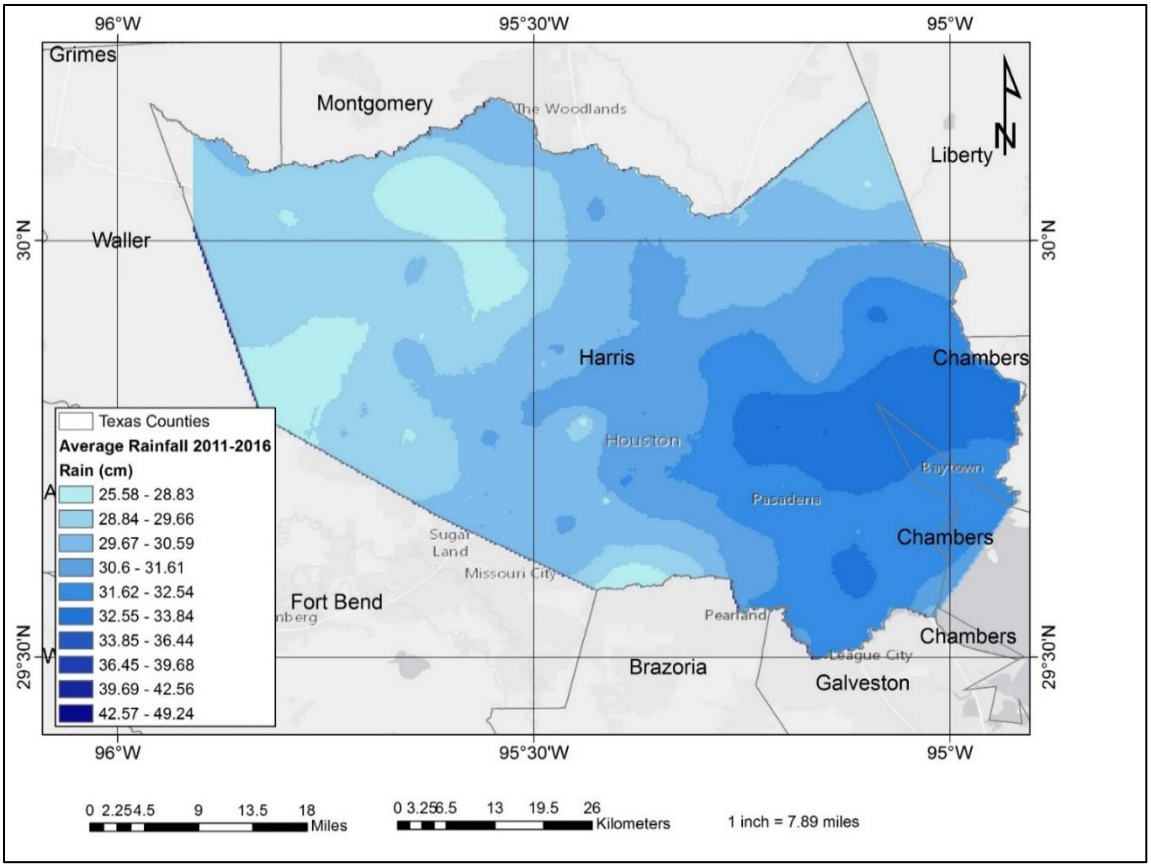

Figure 6: Average rainfall for Harris County from 2011-2016. Unlike the water level, surface water is concentrated towards the southeast along the Gulf Coast and responsible for increased load. Northwest Harris County experiences the least amount of rain, has the smallest loading capacity, and is the most susceptible to subsidence induced by heavy precipitation.

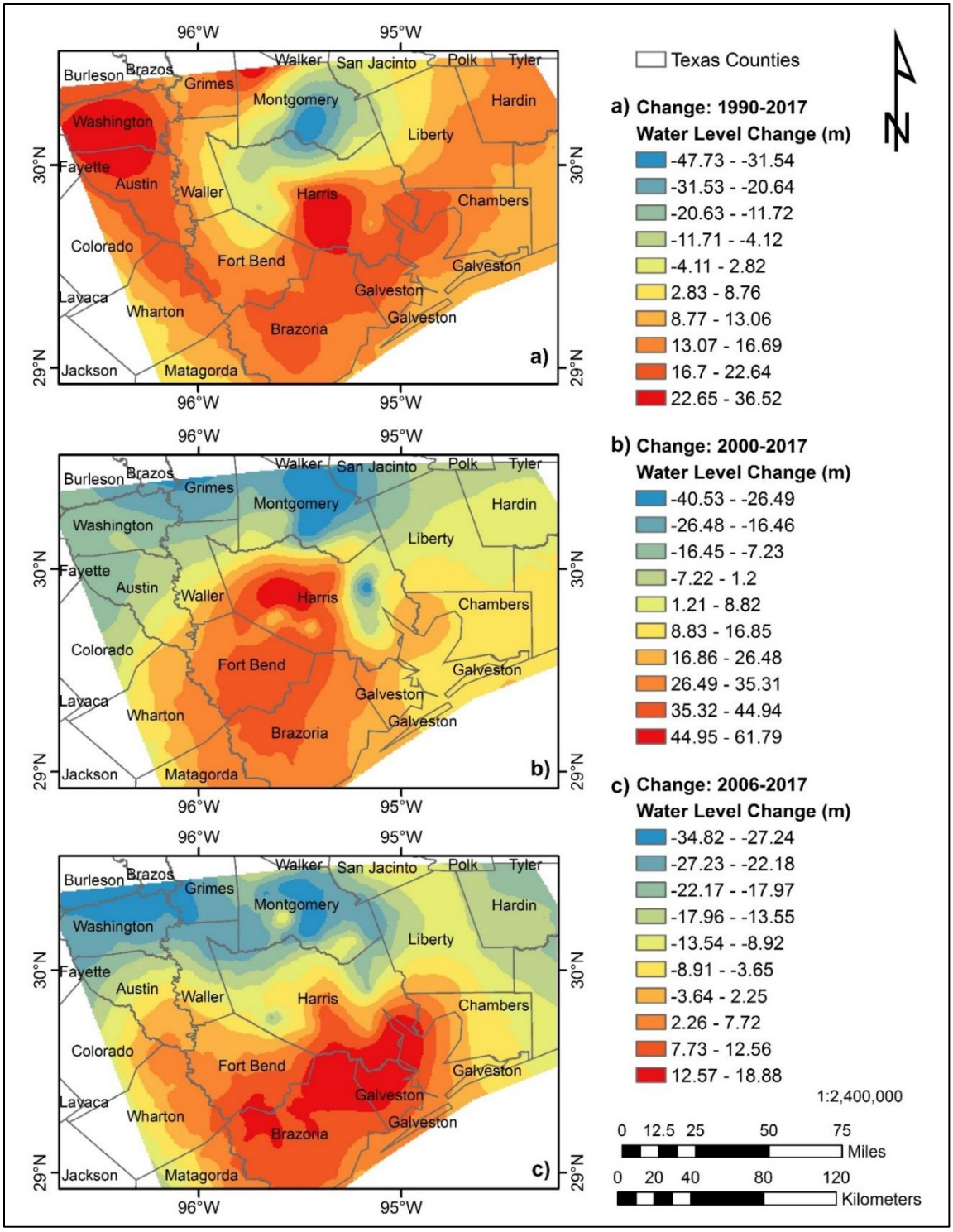

Figure 7: Water level change from a) 1990-2017, b) 2000-2017, and c) 2006-2017 generated using groundwater potentiometric time-series. In all three images, there is a water level decrease in the north and a water level increase in the south.

2.2 GPS Data

Originally, this study set out to processed raw GPS data and independently derive station velocities. Raw GPS data for 68 continuously operating reference stations (CORS) were downloaded from the UNAVCO data archive covering the Houston area from 1990 to September of 2017 (Figure 8). Additional GPS data were provided by the Harris-Galveston Subsidence District (HGSD) for 365 port-a-measure (PAM) stations from 2014-2017. Out of these data, 65 CORS stations and 148 PAM stations had enough data to be processed. PAM station data were first converted into Rinex file format using Trimble's ConvertoRinex application. GPS data were then processed using the Canadian Spatial Reference System (CSRS) Precise Point Positioning (PPP) direct tool provided by Natural Resources Canada's Canadian Geodetic Survey (CGS). CSRS-PPP uses precise GNSS satellite orbit ephemerides to provide positions at the centimeter to decimeter level. This method of GPS processing is highly robust as PPP processing requires fewer reference stations than other methods, the output solution is unaffected by individual reference-station failures, and the same precise orbit and clock data are applicable to users everywhere (National Resources Canada). CSRS-PPP outputs the positioning solution in either CSRS or the International Terrestrial Reference Frame 2008 (ITRF2008) reference frame (option for most global users and the one used in this processing) (Natural Resources Canada).

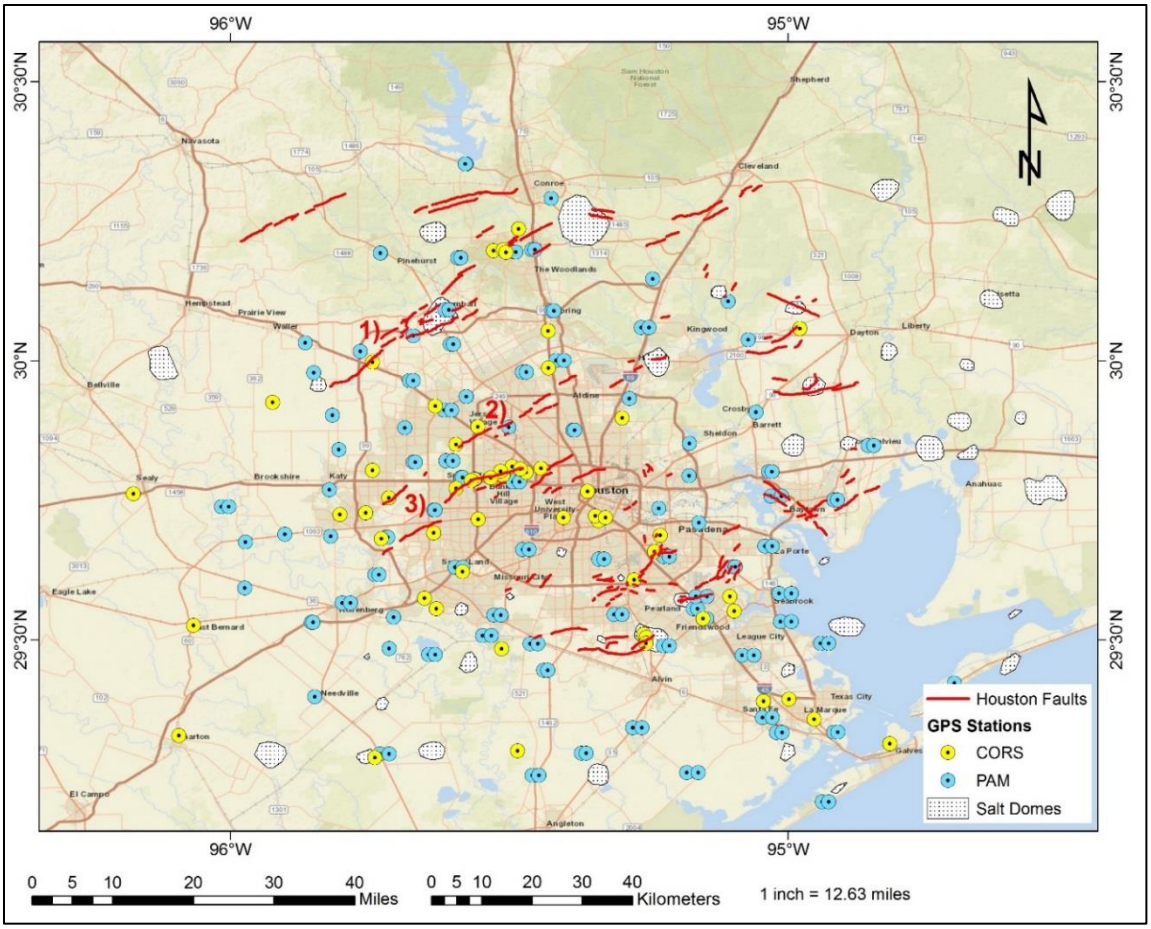

Figure 8: GPS stations independently processed in this study made up of CORS (yellow) and PAM (blue) stations from 1990 to September of 2017.

GPS data were then compiled into an Oracle database and used to calculate station velocities. Station velocity was calculated by first rotating the data into a fixed North American reference frame using a pole-of-rotation calculation and then fitting a first-order polynomial though the GPS observations. The pole-of-rotation calculation was carried out with a python code courtesy of Bennedict Ofeigson of the Icelandic Meteorological Society and plate motion values from Altamimi et al., 2012. The polynomial fit was carried out in MATLAB where coefficients were solved for using a leas-squares approximation; final output were displacement vectors for the easting, northing, and vertical directions (see Appendix).

However, due to inconsintencies in this dataset and the less robust processing methods, GPS data from 1990 to June 2019 were downloaded from the Nevada Geodetic Laboratory (NGL) and used in this study. NGL is a public database of Global Positioning System (GPS) data located within the Nevada Bureau of Mines and Geology at the University of Nevada, Reno (Blewitt et al., 2018). NGL works together with the Department of Geologic Sciences and the Nevada Seismological Laboratory to provide processed GPS data and various GPS derived data products that can be used for both regional and global scale geoscience applications, with the primary goal being to study tectonic and geothermal activity across Nevada. NGL currently operates the Mobile Array of GPS for NEvada Transtension (MAGNET) GPS network. However data products for other GPS station networks are also provided (Blewitt et al., 2018). GPS data are analyzed using the GIPSY-OASIS-II software package provided by the Jet Propulsion Laboratory, Pasadena, California. Processed daily solutions for Continuously Operating Reference Stations (CORS) are compiled in text files and available to users as either (x, y, z) or (easting, northing, up) in either the IGS08 or NA12 coordinate frames (Blewitt et al., 2018).

The IGS08 reference frame is the GPS-based realization of the global secular frame International Terrestrial Reference Frame 2008 (ITRF2008), which an Earth-fixed system with respect to the Earth's center of mass (Blewitt et al., 2013). The NA12 terrestrial reference frame is a plate-fixed frame designed for crustal deformation studies in North America. The NA12 reference frame is based on GPS data from 1996-2012; it is a secular frame defined by 6 Cartesian coordinates of epoch position and velocity of 299 select GPS stations with step-free, or data lacking abrupt jumps, time spans of 4.7 – 16.1 years. There is no net rotation with respect to the stable interior of the North American plate, making it ideal for crustal deformation studies (Blewitt et al., 2013). The origin is also aligned with the IGS08 reference frame such that all vertical motion is with respect to the Earth's center of mass with an accuracy of $\pm$0.5 mm/yr (Blewitt et al., 2013).

For this study, processed GPS data and station velocities in the NA12 reference frame were downloaded for 118 total Continuously Operation Reference Stations (CORS) throughout the greater Houston area (Figure 2). Station velocities are derived using the Median Interannual Difference Adjusted for Skewness (MIDAS) trend estimator as described by Blewitt et al., 2016. Please see the Appendix for a complete list of station velocities. GPS data were then imported into ArcMAP and interpolated surfaces were generated using an Inverse Distance Weighting (IDW) method (Figure 9). GPS vectors were also used to predict surface deformation from 2017-2021, where GPS rates were assumed to be linear.

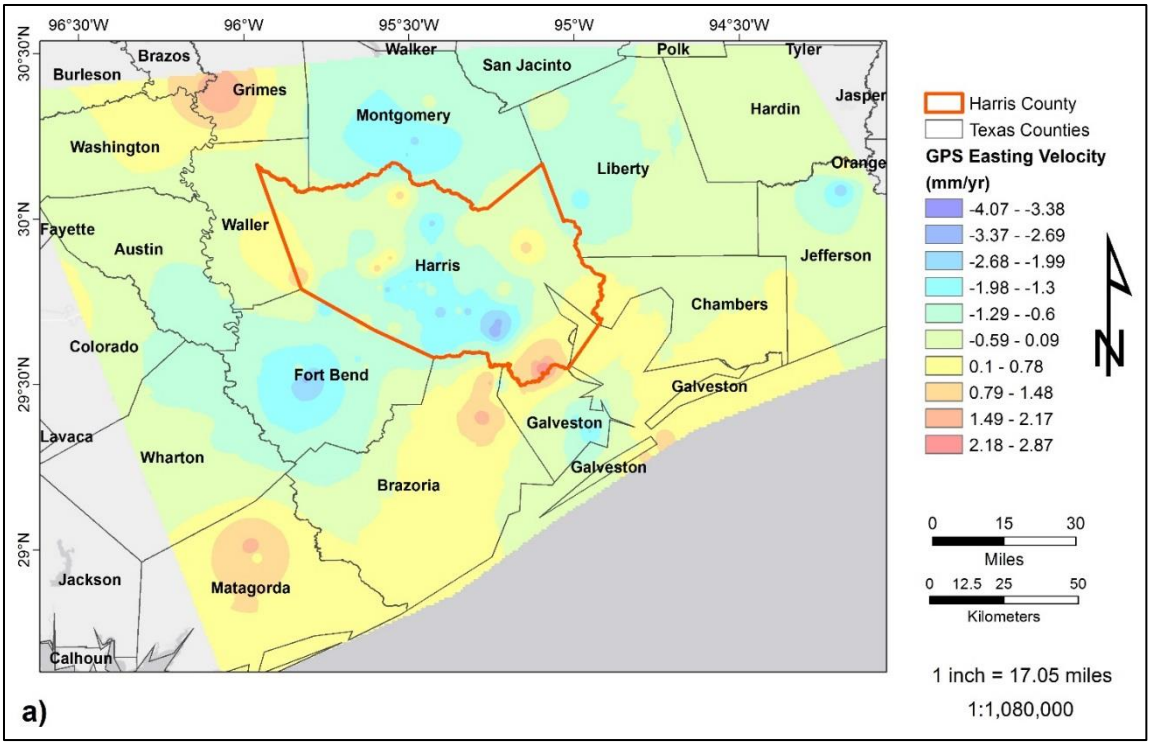
96°30'W
96°W
95°30'W
95°W
94°30'W
30°30'N
30°N
29°30'N
29°N
Brazos
Walker
San Jacinto
Polk
Tyler
Burleson
Grimes
Montgomery
Hardin
Jasper
Washington
Liberty
Orange
Fayette
Waller
Austin
Harris
Jefferson
Chambers
Colorado
Fort Bend
Galveston
Galveston
Lavaca
Wharton
Galveston
Brazoria
Jackson
Matagorda
Calhoun
Harris County
Texas Counties
GPS Easting Velocity
(mm/yr)
-4.07 - -3.38
-3.37 - -2.69
-2.68 - -1.99
-1.98 - -1.3
-1.29 - -0.6
-0.59 - 0.09
0.1 - 0.78
0.79 - 1.48
1.49 - 2.17
2.18 - 2.87
N
0 15 30
Miles
0 12.5 25 50
Kilometers
1 inch = 17.05 miles
1:1,080,000

a)

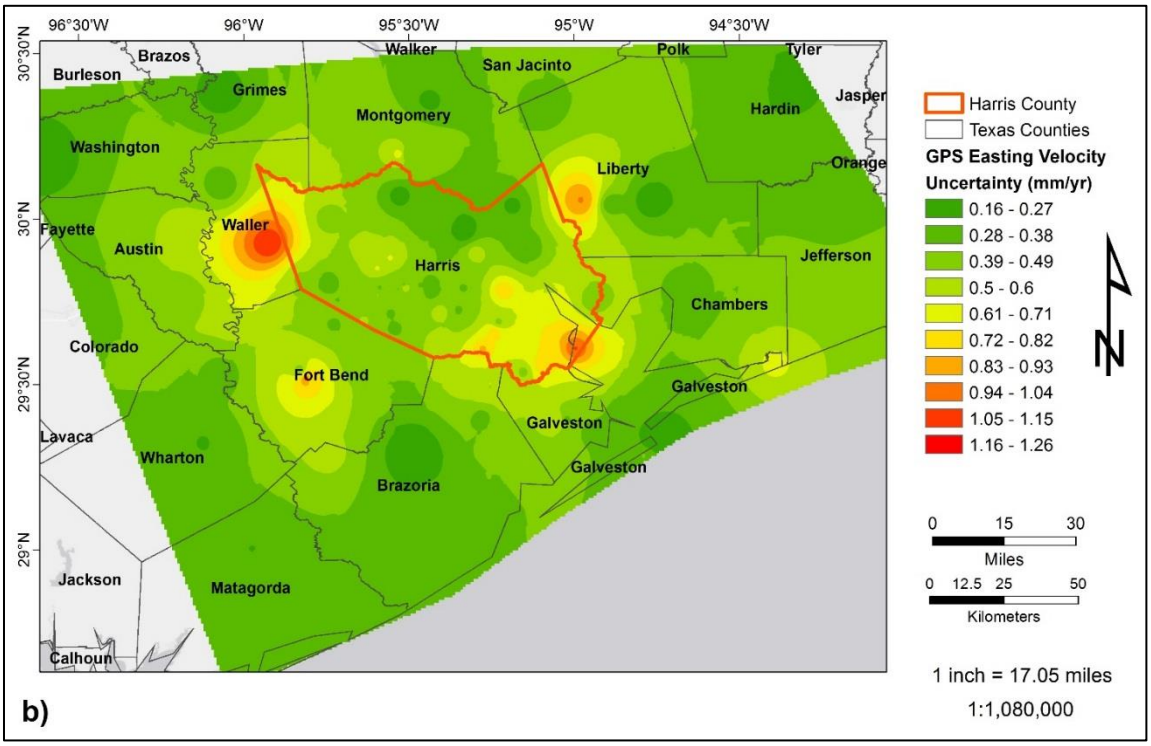
96°30'W
96°W
95°30'W
95°W
94°30'W
30°30'N
30°N
29°30'N
29°N
Brazos
Walker
San Jacinto
Polk
Tyler
Burleson
Grimes
Montgomery
Hardin
Jasper
Washington
Liberty
Orange
Fayette
Waller
Austin
Harris
Jefferson
Chambers
Colorado
Fort Bend
Galveston
Galveston
Lavaca
Wharton
Galveston
Brazoria
Jackson
Matagorda
Calhoun
Harris County
Texas Counties
GPS Easting Velocity
Uncertainty (mm/yr)
0.16 - 0.27
0.28 - 0.38
0.39 - 0.49
0.5 - 0.6
0.61 - 0.71
0.72 - 0.82
0.83 - 0.93
0.94 - 1.04
1.05 - 1.15
1.16 - 1.26
N
0 15 30
Miles
0 12.5 25 50
Kilometers
1 inch = 17.05 miles
1:1,080,000

b)

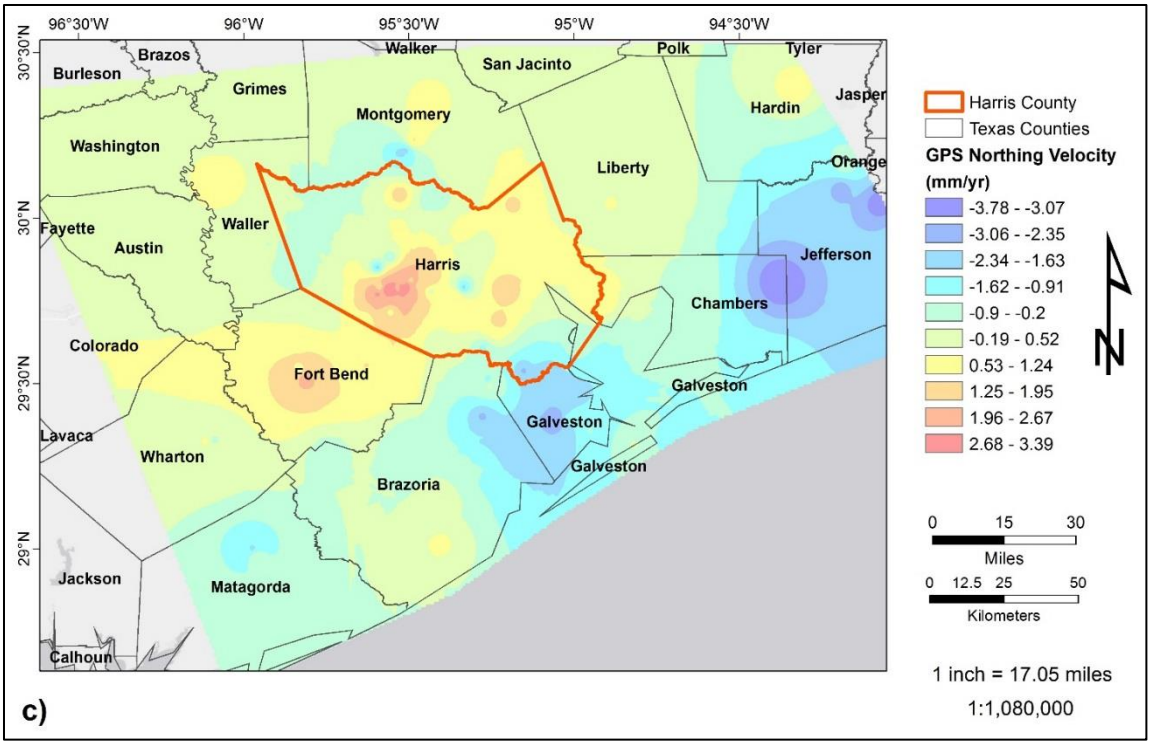
96°30'W
96°W
95°30'W
95°W
94°30'W
30°30'N
30°N
29°30'N
29°N
Brazos
Burleson
Grimes
Walker
San Jacinto
Polk
Tyler
Jasper
Montgomery
Hardin
Washington
Liberty
Orange
Fayette
Austin
Waller
Harris
Jefferson
Chambers
Colorado
Fort Bend
Galveston
Lavaca
Wharton
Brazoria
Jackson
Matagorda
Calhoun
Harris County
Texas Counties
GPS Northing Velocity
(mm/yr)
-3.78 - -3.07
-3.06 - -2.35
-2.34 - -1.63
-1.62 - -0.91
-0.9 - -0.2
-0.19 - 0.52
0.53 - 1.24
1.25 - 1.95
1.96 - 2.67
2.68 - 3.39
N
0 15 30
Miles
0 12.5 25 50
Kilometers
1 inch = 17.05 miles
1:1,080,000

c)

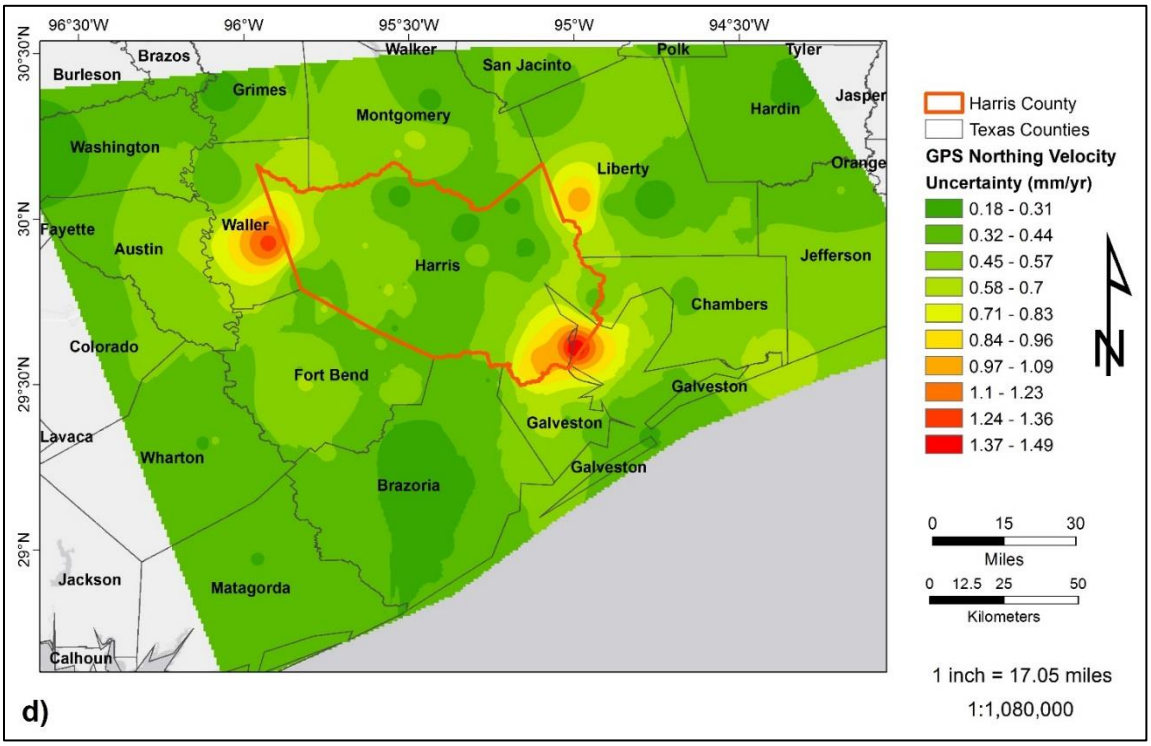
96°30'W
96°W
95°30'W
95°W
94°30'W
30°30'N
30°N
29°30'N
29°N
Brazos
Burleson
Grimes
Walker
San Jacinto
Polk
Tyler
Jasper
Montgomery
Hardin
Washington
Liberty
Orange
Fayette
Austin
Waller
Harris
Jefferson
Chambers
Colorado
Fort Bend
Galveston
Lavaca
Wharton
Brazoria
Jackson
Matagorda
Calhoun
Harris County
Texas Counties
GPS Northing Velocity
Uncertainty (mm/yr)
0.18 - 0.31
0.32 - 0.44
0.45 - 0.57
0.58 - 0.7
0.71 - 0.83
0.84 - 0.96
0.97 - 1.09
1.1 - 1.23
1.24 - 1.36
1.37 - 1.49
N
0 15 30
Miles
0 12.5 25 50
Kilometers
1 inch = 17.05 miles
1:1,080,000

d)

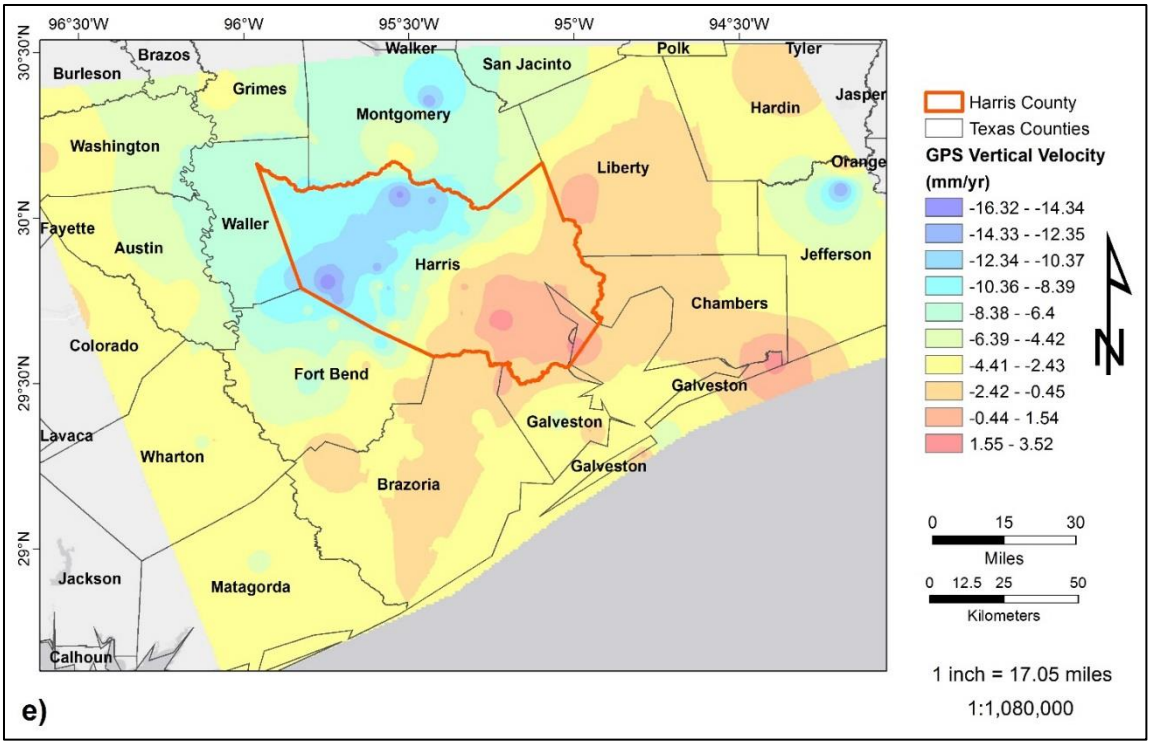

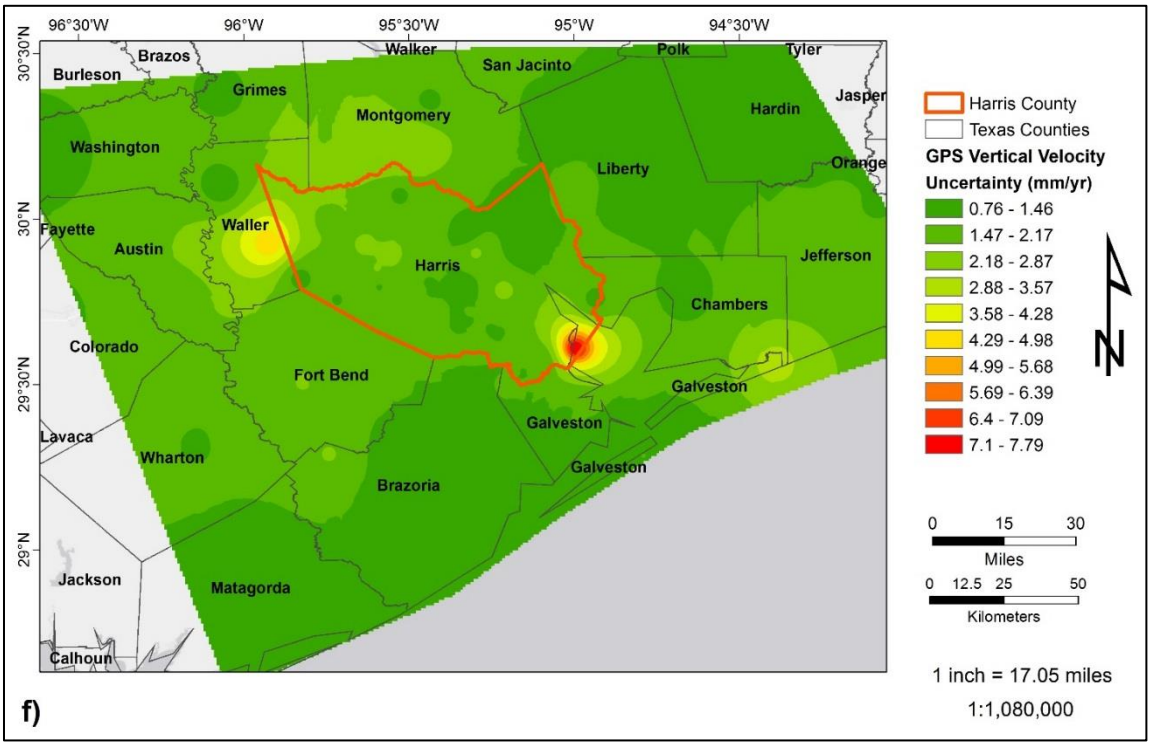

Figure 9: GPS velocity and uncertainty surfaces generated using IDW interpolation method, GPS data from the Nevada Geodetic Laboratory and the MIDAS velocity estimation method. Sub-figures a, c, and e show the GPS velocities in mm/yr for the Easting, Northing, and Vertical components where the red color represent motion in that respective direction and blue represents

motion in the opposite direction. Sub-figures b, d, and f show the uncertainties in mm/yr for the Easting, Northing, and Vertical components where green is low uncertainty and red is high uncertainty. Uncertainty is primarily concentrated towards the boundary of Walker and Harris Counties, and along the boundary of Galveston and Harris Counties across all three components of motion. This corresponds to poor spatial distribution and reduced data coverage in these areas. A subsidence bowl in northern Harris County can be observed in the vertical velocity surface map. This causes nearby areas to deviate from a predominantly southeast track and point towards the center of this subsidence bowl.

2.3 Groundwater Modeling

Groundwater level modeling and predictions from 1990-2027 were performed to evaluate the impact of current withdrawal rates in the future. Modeling was carried out in MATLAB and involved calculating both the high and low-frequency components of groundwater level. The time-series groundwater data from 1990-2017 generate earlier were imported into MATLAB, where an 8th order sum of sines (sin8) fit, as shown below, was used to interpolate values from 1986-2031.

$$y = \sum_{i=1}^{n} a_i \sin(b_i x + c_i)$$

*Equation 2: (*Sum of Sines Equation)

The sin8 fit was the only function capable of handling the strong seasonal (high-frequency) variation of the data, however, because predictions degraded around the edges of the time-series, the data had to be padded by four years at the beginning and end, hence the 1986-2031 time frame. The resulting sin8 fit had an average R-squared factor of ~68% and a correlation coefficient ranging from ~0.3-0.5, indicating that the fit accounts for most of the observed data and that the fit and raw data have a moderately positive linear relationship. The R-squared factor

and correlation coefficient are not higher because of the sinuous nature of the data and because edge artifacts were not fully removed. A simple boxcar filter with cutoffs of ±152.4 m (500 ft) was then applied to remove aberrant water level predictions. Next, a 6th order polynomial function was fit through the sin8 fit so as to model the low-frequency variation and calculate water level for each point from 1990-2027. However the prediction started to degrade around winter 2021. The 6th order polynomial fit had a smaller average R-squared factor of ~50%, but that is expected since it is modeling the low-frequency variation. Another boxcar filter with the same cutoffs as before was also applied to remove aberrant values. Lastly, Kriging interpolation was applied to the prediction results.

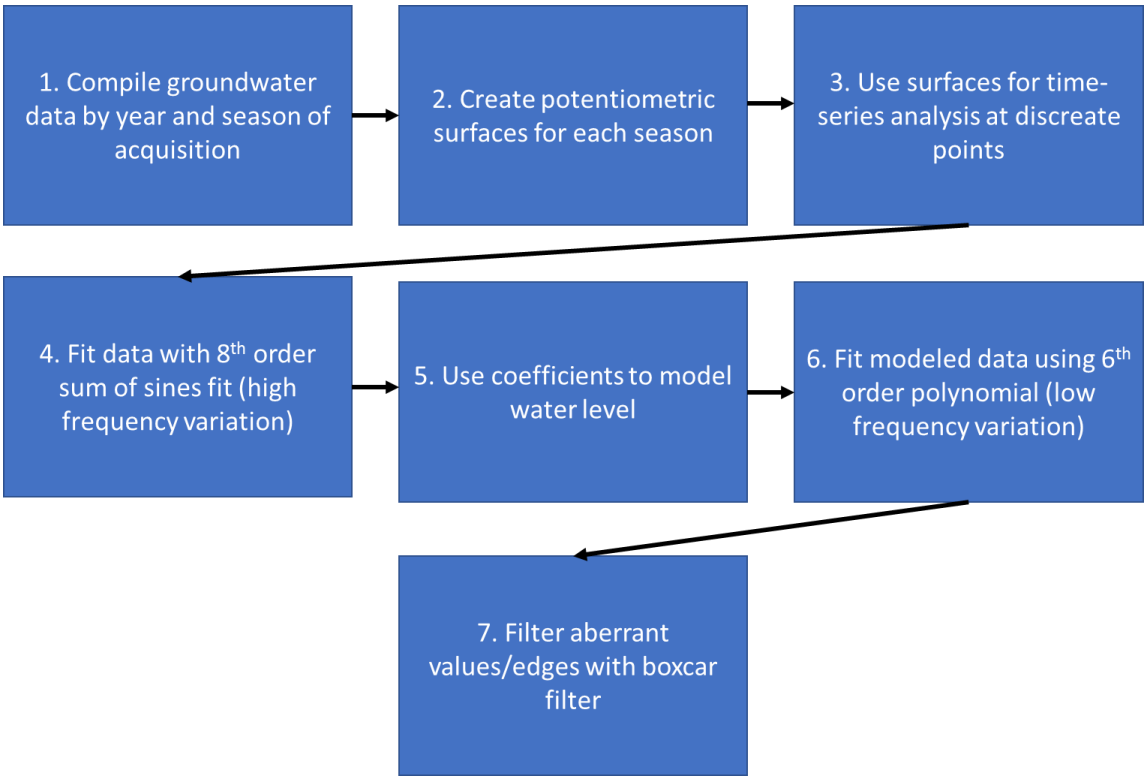

Figure 10: Groundwater prediction workflow.

2.4 Radar Mapping

For this work, we examined the city of Houston, Texas recently following Hurricane Harvey using 7 ascending TOPSAR Sentinel-1 IW (interferometric wide swath) VV polarized images from August 12, 2017, and September 17, 2017, as shown below (Figure 11). While the images share track and frame numbers, the August 30, 2017 (20170830) image had a slightly different footprint, which resulted in no data across the bottom of the image. Despite the missing data, this image was processed and analyzed as it covers the period when the flooding was most severe (Blake and Zelinsky, 2017). These images are acquired in TOPSAR mode and contain three sub-swaths: IW1, IW2, and IW3. Data in each sub-swath is acquired in multiple bursts which create seams in the image. These seams, or demarcations as they are also called, must be removed in TOPSAR processing through the process of debursting (Veci, 2015).

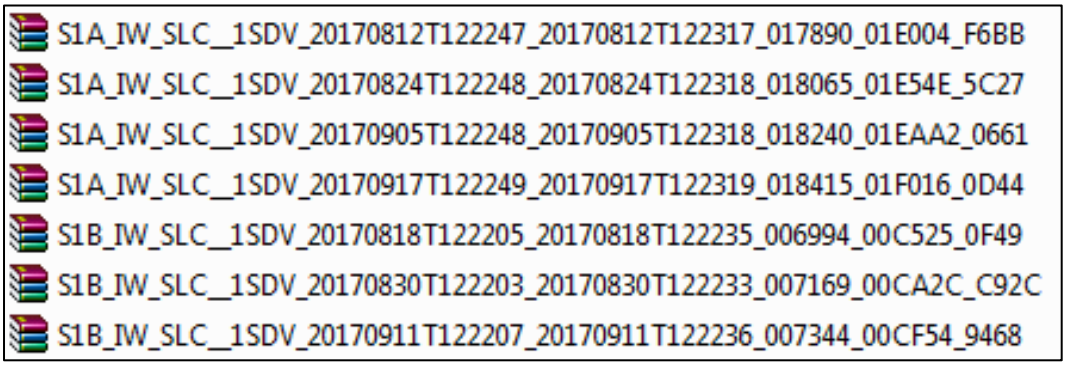

Figure 11: Seven ascending Sentinel-1 IW images.

Radar processing was done using the Sentinel Application Platform (SNAP) software provided by the European Space Agency (ESA) and ENVI software provided by Harris Geospatial Solutions. Radar pre-processing was done by first applying a Sentinel precise orbit files. The

orbital files contain additional information about the position of the satellite during data acquisition such as orbital state vectors, which are used to determine a more precise orbit (Veci, 2015). As the city of Houston is contained within the IW1 and IW2, the TOPSAR images were into the respective sub-swath components to save computing power. Sub-swaths IW1 and IW2 were then radiometrically calibrated to backscatter (Sigma0) and deburst before merging into a single image. The image was then terrain corrected and speckle filtered using a Refined Lee filter. The coherence was calculated by designating the August 12, 2017 pre-flood image as the master for all 6 image pairs; the August 12, 2017 image was also used for backscatter comparison. Visual inspection revealed coregistration issues between the backscatter of images of August 18, 2017 (20170818), August 30, 2017 (20170830), and September 11, 2017 (20170911) due to slight misalignments of satellite orbits. These backscatter images were manually coregistered to the August 12, 2017 (master) image in ENVI using a first-order polynomial wrap method and nearest neighbor resampling. Coregistration information is summarized below in Table 2. False color composite images of RGB: coherence, mean backscatter, and backscatter difference were then created, as shown in Figure 12 and used to identify different endmembers.

Table 2: Coregistration information.

Image	GCPs	RMS error
20170830	50	0.846992
20170818	51	0.773319
20170811	54	0.800342

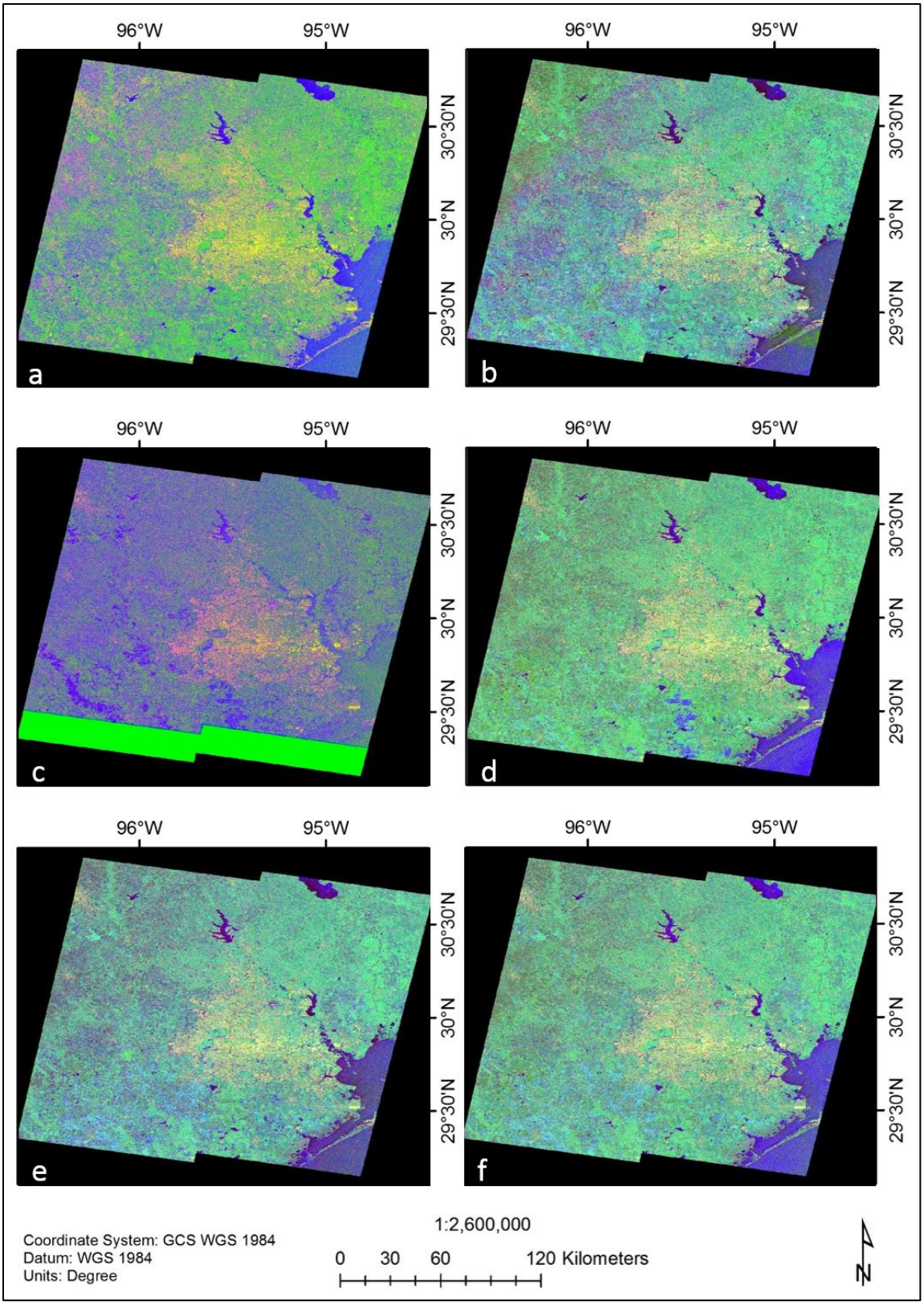

Figure 12: False-color composite images of RGB: coherence, mean backscatter, and backscatter difference for a) August 18, 2017 (20170818), b) August 24, 2017 (20170824), c) August 30, 2017

(20170830), d) September 5, 2017 (20170905), e) September 11, 2017 (20170911), and f) September 17, 2017 (20170917). The base image for coherence and backscatter changes is August 12, 2017. Blue is water (areas of both low backscatter and low coherence), yellow is urban (high backscatter and high coherence), green is vegetation (high backscatter and low coherence), and red is bare soil or roads (low backscatter and high coherence). Bright green area along the bottom edge of Figure 11c represents a lack of data and was excluded from further processing. This same figure shows an increase in red areas over what should be urban settings and an increase in vegetation over what should be water. Both of these changes are a result of loss of coherence and increased texture during this time. Flooding was most severe August 30, with flood waters persisting until late September. The southwest corridor of Houston retained flood water for the longest time.

Cutoff thresholds for endmembers in each image were calculated by analyzing the histograms of the difference and mean backscatter. As the images are made up of flooded and dry areas, the histograms are bimodal, as shown in Figures 13.

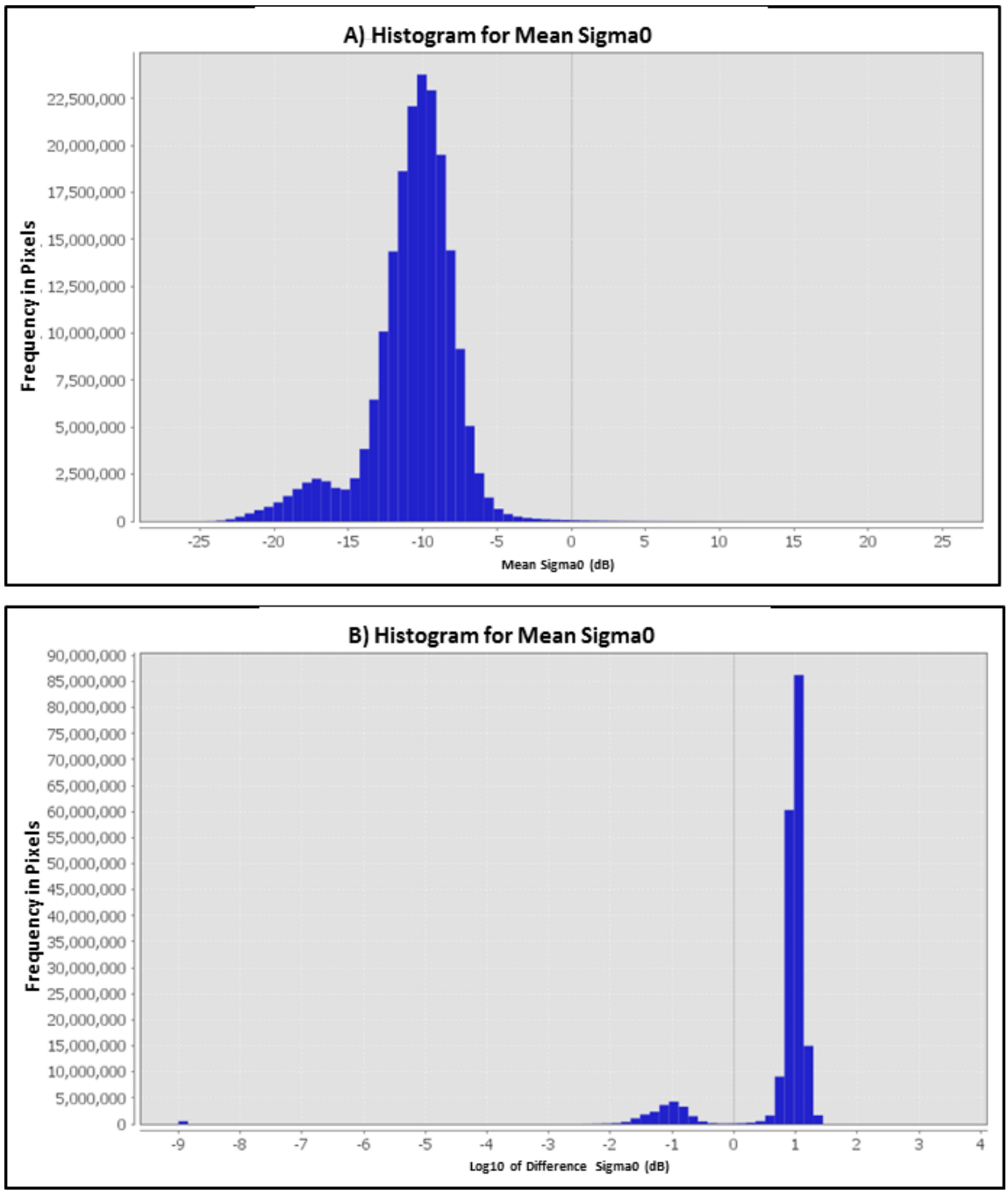

Figure 13: a*) Histogram of backscatter difference showing bimodal distribution associated with flooded areas. b) Histogram of mean backscatter showing bimodal distribution associated with flooded areas.*

Martinis, S., and Rieke, C. (2015) compiled a list of common vegetation types and their associated backscatter range when flooded. For a coastal wetland, the backscatter was found to decrease by 15.1-6.8 dB when flooded; for the Houston area, a cutoff of -13.5 dB was used in this study. For urban areas, the coherence cutoff been identified as 0.48 by Grey et al., 2003**.** The ocean areas in the southeast were then masked using an SRTM 30m DEM, and the images were classified into 1) urban areas, 2) bare soil, 3) water, 4) vegetation, 5) flooded areas, and 6) flooded vegetation. Lastly, a 3x3 arithmetic mean filter was applied to each class to further smooth out any remaining speckle. This filter was chosen because it preserved fine details such as thin streams and flooded streets, while still smoothing the image. Statistics for each image pair were then computed to determine the percentage of each component.

Chapter 3: Results

3.1 GPS and Water Data

Figures 5a-d of seasonal water withdrawal averages from 1990-2017 highlight the typical seasonal (high frequency) variation and show elongate, approximately north-south, concentric patterns centered over the city of Houston. The highest water withdrawal occurs in the fall and winter seasons and is concentrated in northern Harris County, also expanding into parts of Fort Bend, Brazoria, and Galveston Counties. This water withdrawl is likely linked to the recent and rapid growth of cities such as Sugarland, Missouri City, Pearland, and League City. These images delineate the spatial extent and groundwater level change associated with seasonal variation. All aquifer systems undergo reversible surface deformation in response, yet large scale deviations from these baselines will result in irreversible deformation (Galloway et al., 1999).

Figure 6 shows the average rainfall over Harris County from 2011 to 2016. Increased rainfall will result in overloading the local aquifer system and lead to increased subsidence. While the Gulf Coast is known for its wet climate, most of the rain is concentrated around the coast and southern Harris County. This difference in rainfall makes northwest Harris County the most at risk for large scale deviations in aquifer loading, as can occur during storms, hurricanes, and floods. The water level change images in Figure 7 represent low-frequency variation experienced by the aquifer systems and shows large scale concentric patterns centered primarily over northern Harris County. Figure 7a from 1990-2017 shows an increase in the water level over the south and northern Harris County, likely the result of monitoring and control efforts from the Harris County Subsidence District, and a noticeable decrease in the water level over northeast Harris and southern Montgomery counties centered over the Woodlands area. This trend is also apparent in Figures 7b and 7c with an increase in the water level in the south, and a decrease in the water level in the north.

Figure 9 shows the GPS velocity and uncertainty surfaces that were generated using an IDW interpolation method, data from the Nevada Geodetic Laboratory and the MIDAS velocity estimator. Surfaces in Figure 9a, c, and e correspond to GPS velocity in mm/yr along the Easting, Northing, and Vertical directions respectively. Motion along these three principle directions is represented by the red color, while blue color represents motion in the opposite direction. Surfaces in Figure 9b, d, and f correspond to the GPS uncertainties in mm/yr along the Easting, Northing, and Vertical directions respectively. High uncertainty in the final velocity is shown by the red color while low uncertainty is shown by green color. The horizontal components of motion, the Easting and Northing, have the lowest uncertainties with data showing less than 1.5 mm/yr uncertainty. The Vertical uncertainty is much higher, going up to 7.8 mm/yr; however these are in line with the resolution of GPS data. Across all three uncertainty maps, areas of high uncertainty are primarily concentrated on the boundary of Walker and Harris Counties, as well as on the boundary of Galveston and Harris Counties. These areas correspond to poor spatial distribution of GPS stations and reduced data coverage as can be seen in Figure 2.

Figure 9a of the Easting velocity shows stations in Fort Bend, Harris, and Montgomery Counties moving slightly westward. These same areas are shown to move towards the north in Figure 9b and move downwards in Figure 9e. This motion is contrary to stations outside of these areas, where the general trend seems to be a southeastern motion with very little vertical motion. The juxtaposed motion is best explained by the presence of a subsidence bowl as can be seen in Figure 9e. The area undergoing subsidence is spatially distributed as an oblong oval covering most of northern Harris County. Northern Harris County is subsiding as high as 16.32 mm/yr, and shows an average range of ~14-8 mm/yr in downwards motion. As this area is subsiding very quickly, it creates a bowl shape which causes nearby GPS stations to record motion towards the center of the bowl.

Interpolated surfaces were generated for horizontal velocity vectors, vertical velocity vectors, and total velocity vectors which were then overlaid with groundwater change contours from 2006-2017 (Figures 14). Figure 14a shows the rotated GPS total velocity vectors over the Houston area, and highlights the southern track of salt domes and motion along the Long Point-Eureka Heights Fault System. The total GPS velocity surface with overlaying water level change from 2006-2017 is shown in Figure 14b, where the areas with the highest velocities are found to the north and south. The south corresponds to where most of salt domes are located, however it is likely that the high velocity in Grimes County and further north is an interpolation artifact due to too few data points. Large amounts of motion are found in northern Harris County, northwestern Fort Bend County, and central Montgomery County which correspond to areas of water withdrawal. There is much lower motion towards the southwest and northeast sections of the map; however this may be due to too few data points outside of Harris County.

The decomposed GPS velocity into horizontal and vertical components of motion are shown in Figures 14c and 14d. The area of high horizontal motion in Figure 13c are concentrated along the Long Point-Eureka Heights fault system, central Montgomery County, central Fort Bend County, central Jefferson County, and southeast Harris County/Galveston County. Southeast Harris County and Galveston County are located over salt domes and experienced a groundwater increase from 2006-2017. Here horizontal motion is from 3.25-3.76 mm/yr along a southern track. The remaining areas experienced ground water level decrease from 2006-2017, with the most notable being over central Harris County and central Montgomery County. Horizontal motion in these two areas ranges from ~2-3 mm/yr. Motion along the Long Point-Eureka Heights fault system is approximately 3.2-3.7 mm/yr in the horizontal and pointing northwards.

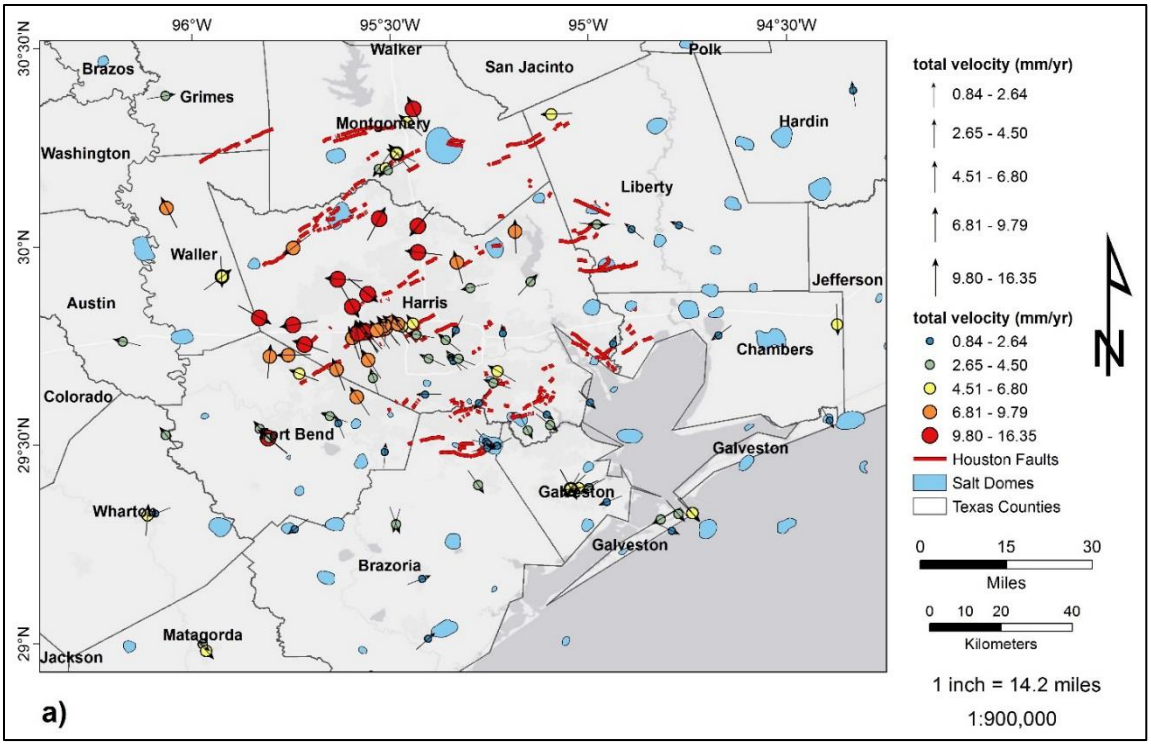
96°W
95°30'W
95°W
94°30'W
30°30'N
30°N
29°30'N
29°N
Brazos
Grimes
Walker
San Jacinto
Polk
Montgomery
Hardin
Washington
Liberty
Waller
Jefferson
Austin
Harris
Chambers
Colorado
Fort Bend
Galveston
Wharton
Brazoria
Matagorda
Jackson
total velocity (mm/yr)
0.84 - 2.64
2.65 - 4.50
4.51 - 6.80
6.81 - 9.79
9.80 - 16.35
total velocity (mm/yr)
0.84 - 2.64
2.65 - 4.50
4.51 - 6.80
6.81 - 9.79
9.80 - 16.35
Houston Faults
Salt Domes
Texas Counties
0 15 30
Miles
0 10 20 40
Kilometers
1 inch = 14.2 miles
1:900,000
a)

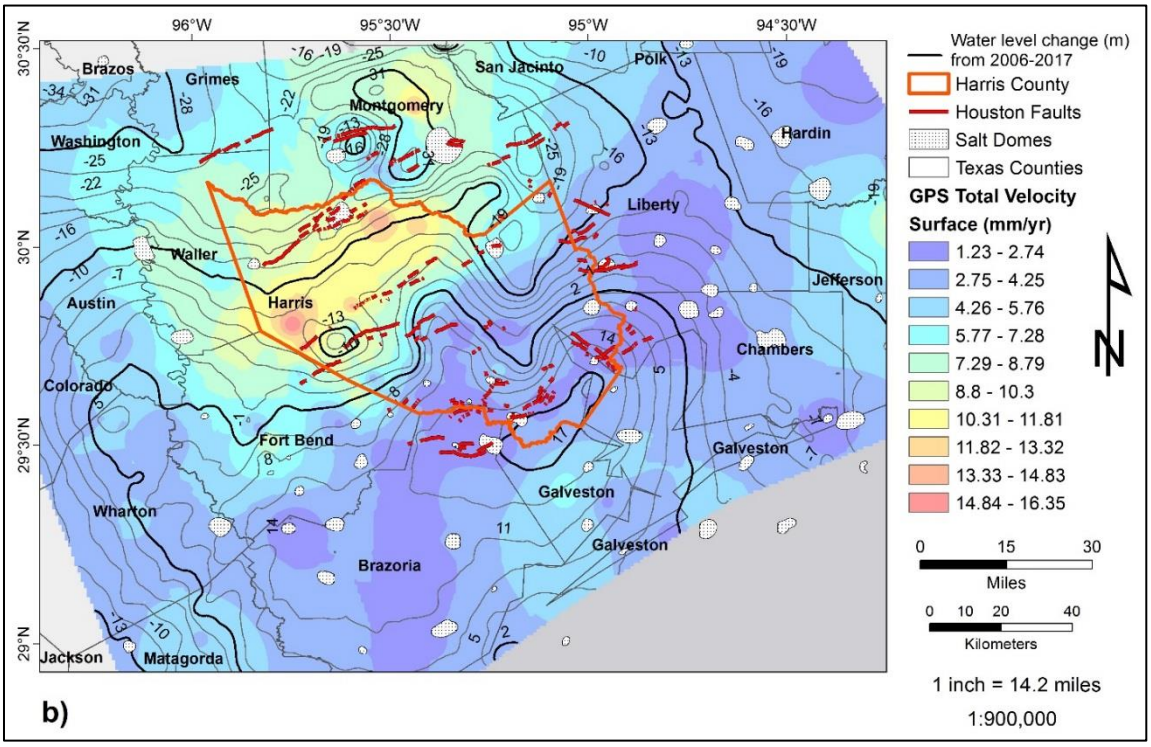
96°W
95°30'W
95°W
94°30'W
30°30'N
30°N
29°30'N
29°N
Brazos
Grimes
San Jacinto
Polk
Montgomery
Hardin
Washington
Liberty
Waller
Jefferson
Austin
Harris
Chambers
Colorado
Fort Bend
Galveston
Wharton
Brazoria
Jackson
Matagorda
Water level change (m) from 2006-2017
Harris County
Houston Faults
Salt Domes
Texas Counties
GPS Total Velocity Surface (mm/yr)
1.23 - 2.74
2.75 - 4.25
4.26 - 5.76
5.77 - 7.28
7.29 - 8.79
8.8 - 10.3
10.31 - 11.81
11.82 - 13.32
13.33 - 14.83
14.84 - 16.35
0 15 30
Miles
0 10 20 40
Kilometers
1 inch = 14.2 miles
1:900,000
b)

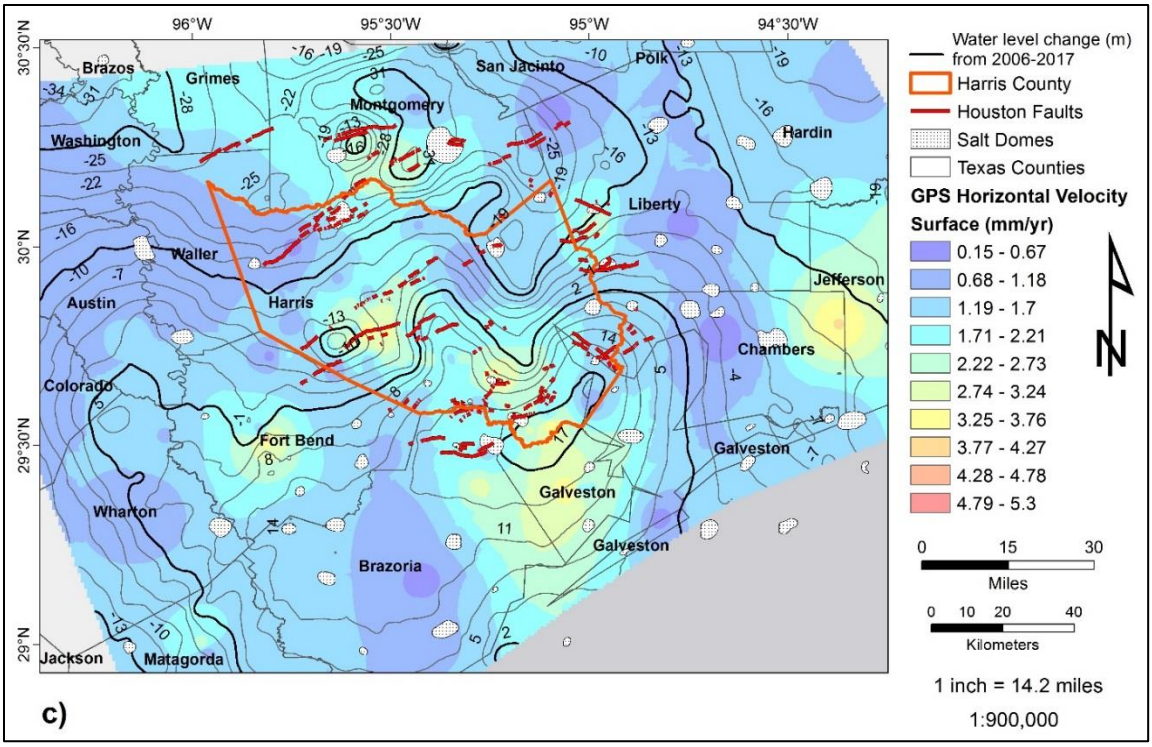

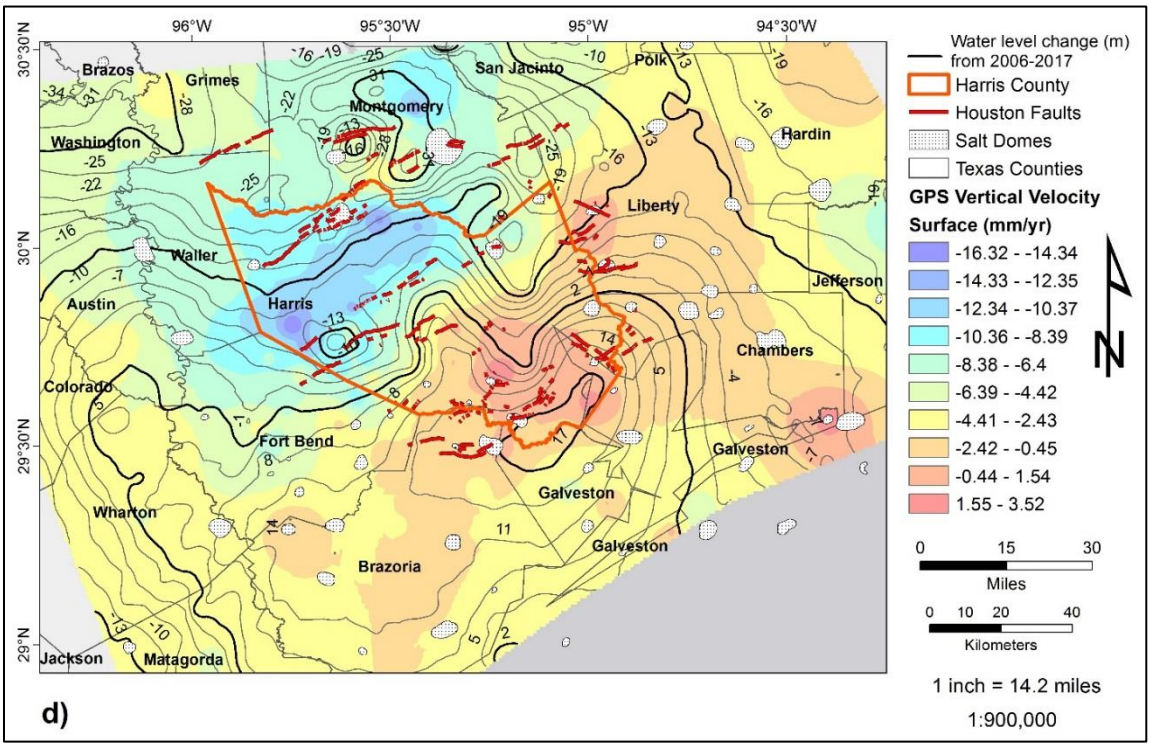

Figure 14: Surfaces in Figures B through D are generated using an Inverse Distance Weighting interpolation and GPS data from the Nevada Geodetic Laboratory in NA12 reference frame. GPS data consist of CORS stations from 1990 to June of 2019. Groundwater changes are shown from 2006 to 2017. a) Plotted GPS total velocity vectors over the Houston area; vectors highlight

southern salt dome movement and fault motion along the Long Point-Eureka Heights fault system. b) GPS Total Velocity Vector Surface (mm/yr) with plotted GPS stations and GPS vectors. c) GPS Horizontal Velocity Vector Surface (mm/yr); areas of high horizontal motion are concentrated along the Long Point-Eureka Heights fault system, central Montgomery County, central Fort Bend County, and central Jefferson County which correspond to a decrease in the water table from 2006-2017. Areas of high horizontal motion are also found in southeast Harris County/Galveston County over salt domes. Here horizontal motion is ~1-3.5 mm/yr along a Southern track. d) GPS Vertical Velocity Vector Surface (mm/yr); it shows the best water level change correlation, with uplift over salt domes of up to 3.5 mm/yr and increasing vertical displacement over the Long Point-Eureka Heights faults system from west to east. Subsidence takes place primarily in northern Harris County, central Montgomery County, and northern Fort Bend County. Differential fault motion corresponds to increase in groundwater from west to east, while subsidence corresponds to a decrease in the water table.

3.2 Radar Mapping and Classification

The false color composite images are shown in Figure 12 where blue color represents areas of low backscatter and low coherence (water), yellow color are areas of high backscatter and high coherence (urban), green color are areas of high backscatter and low coherence (vegetation), and red color are areas of low backscatter and high coherence (bare soil/roads). This simple visual classification works rather well except for the case of Figure 12c (August 30, 2017; 20170830). Figure 12c (August 30, 2017; 20170830) shows green color in the lower right-hand corner that should be classified as water. There is also an abundance of red color in what should be urban areas. Such a drastic change compared to the other images is due to the large coherence and backscatter difference caused by the extreme flooding that occurred at this time. August 30, 2017 (20170830) was characterized by peak hurricane activity and large amounts of rainfall which flooded much of the greater Houston area and decreased the observed backscatter (Blake and Zelinsky, 2017). The increased storm activity had the opposite effect for the Gulf of Mexico where surface texture was increased, causing an increase in the backscatter. To accurately classify this image, threshold values for the difference and mean backscatter had to be relaxed to detect subtle changes. This increase in

surface texture also made it necessary to apply a mask over the sea portion of the images and a smoothing filter to avoid erroneous classification. Note that the green area on the lower part of Figure 12c designates a lack of data and was not considered for classification.

Classified images and statistics are shown in Figures 15-16 and Table 3. In Figure 15, green is vegetation, blue is water, light orange is bare soil, and red are urban areas. As before, the green areas on the lower portion of Figure 15c designated a lack of data and was not considered. The urban areas and bare soil become harder to distinguish in the zoomed-out views as the flooding intensifies due to the increase in backscatter. In these classification images, the water class designates the total amount of detected water and does not differentiate between flooded and normal conditions. The same can be said for the vegetation class, which does not distinguish between dry and flooded vegetation. These classes are broken up into the flooded and dry components in Figure 16. The backscatter differences images are shown for each date along with water under normal conditions (blue), flooded areas of open water (cyan), and areas of flooded vegetation (red). In order to reduce possible misclassification due to the backscatter variability caused by storm conditions, classes were defined as non-overlapping. The water under normal conditions was derived from the August 18, 2017 (20170818) image, before the flooding event.

It is to be noted that during this time rainfall was experienced in the Houston area, which led to very minor flooding as shown in Table 3. Overall, the flooding was most prolonged along the lower left-hand side of the image corresponding to the Brazos River. This area started flooding as early as August 24, 2017 (20170824), and remained in such a state past September 17, 2017 (20170917). From the following images, it does not appear that the San Jacinto River was inundated for very long, despite the rather larger footprint recorded by USGS in-situ measurements. The heavy rainfall, coupled with the long time it took to drain flood on

Houston's southeast corridor, makes the southwest Houston area one to monitor for future surface deformation and possible subsidence. The 4-year prediction from 2017-2021 shows this area deforming by about -1.4 cm under normal conditions. This will likely increase in the presence of extensive flooding, each even likely deforming an additional 1-2 cm if of a similar magnitude/longevity as Hurricane Harvey (Milliner et al., 2018).

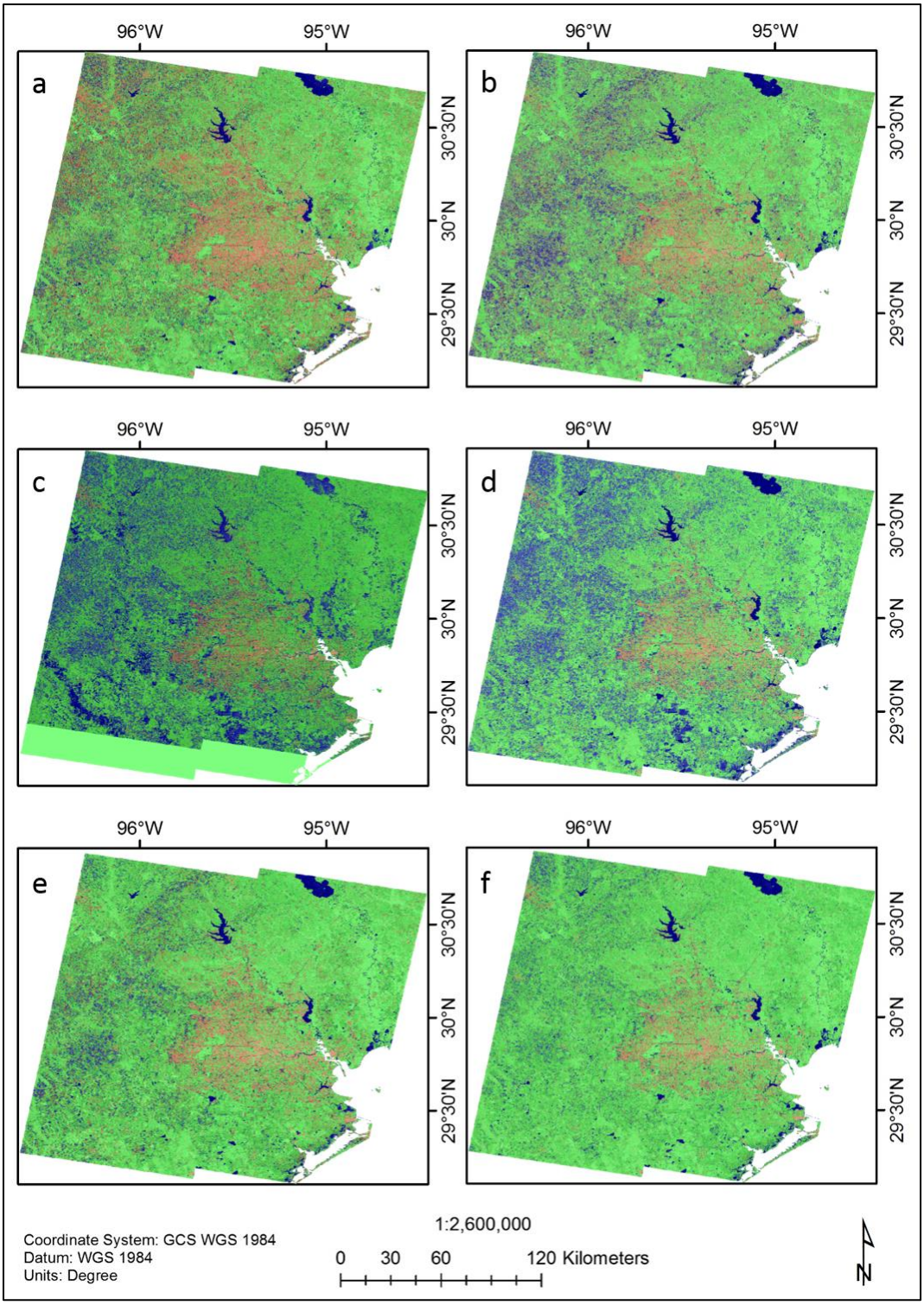

Figure 15: Classification images for a) August 18, 2017 (20170818), b) August 24, 2017 (20170824), c) August 30, 2017 (20170830), d) September 5, 2017 (20170905), e) September 11, 2017 (20170911), and f) September 17, 2017 (20170917). Green is vegetation, blue is water, light orange is bare soil, and red are urban areas. The urban areas and bare soil become harder to distinguish in the zoomed-out views as the flooding intensifies due to the increase in backscatter.

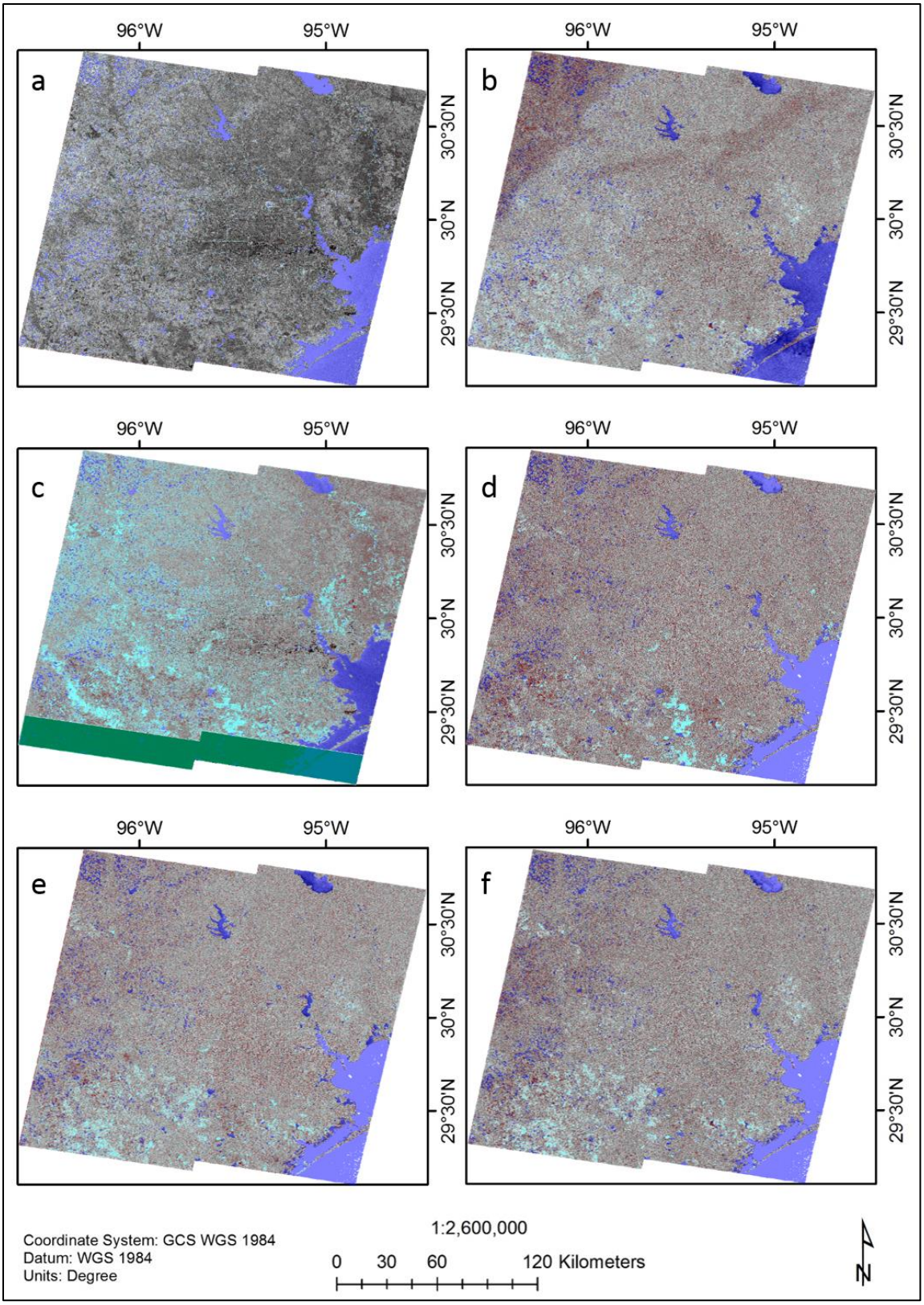

Figure 16: Backscatter difference images where blue is water under normal conditions, cyan is flooded areas, and red is flooded vegetation. Images are as follows: a) August 18, 2017

(20170818), b) August 24, 2017 (20170824), c) August 30, 2017 (20170830), d) September 5, 2017 (20170905), e) September 11, 2017 (20170911), and f) September 17, 2017 (20170917). Note that the green area in Figure 16c is masked out and not considered due to a lack of data.

Table 3: Statistics of radar classification. The green color represents images that did not have to be manually coregistred, while the yellow corresponds to images that had to be coregistered and had a different spatial extent. The open water class is made up of all the detected water in the image, while the flooded class indicated what fraction of the water is due to flooding.

Number of Pixels per Class per Observation						
	20170818	**20170824**	**20170830**	**20170905**	**20170911**	**20170917**
Urban	43551092	23471667	11605876	15931718	15487145	15473941
Bare Soil	428319	1979952	2193911	667754	733382	743799
Vegetation	136199718	143869111	129563744	155656837	154807164	155098518
Open Water	4605115	15406428	41420713	12408451	13756576	13411088
flooded	624900	7781052	33635191	8134308	11789563	7825805
flooded veg	13736425	13639439	21240930	21956440	18197908	15065776
Urban (%)	23.5686	12.7061	6.2808	8.6274	8.3812	8.3766
Bare Soil (%)	0.2318	1.0718	1.1873	0.3616	0.3969	0.4026
Vegetation (%)	73.7074	77.8819	70.1162	84.2916	83.7772	83.9608
Open Water (%)	2.4922	8.3401	22.4157	6.7194	7.4447	7.2599
flooded (%)	0.3382	4.2122	18.2024	4.4049	6.3802	4.2364
flooded veg (%)	7.4338	7.3836	11.4950	11.8899	9.8482	8.1557

Looking at Table 3, the conditions prior to Harvey on August 18, 2017 (20170818) indicate that around 8% of the image is flooded. This aligns with weather reports of heavy rainfall at the time. The amount of flooded areas jumps up drastically from 0.3% to 18% on August 30, 2017 (20170830). This is accompanied by a 4% increase in the flooded vegetation, likely an underestimate due to the complex target and thick tree canopies as discussed previously. By September 5, 2017 (20170905) the flooding has decreased significantly, but the image is still not experiencing pre-Harvey conditions. The classification results before the flooding in August 18, 2017 (20170818) also show that the image is made up of about 74% vegetation.

After the flooding event this number jumped to 84%, an overall increase of ~10%.

It is unlikely that during this time vegetation grew so drastically as to make up for the above change, however the reduction in coherence that was experienced by flooded buildings with high backscatter may have caused them to be misclassified as vegetation (Chini et al., 2019). Similarly, water bodies experienced an increase in surface texture during the storm, which resulted in misclassification as vegetation to a much lesser degree. These changes, along with the increase in vegetated debris following the flooding, can account for the increase in observed vegetation. Moreover, this information tells that around half of the observed buildings in August 18, 2017 (20170818) became inundated to some degree as a result of Hurricane Harvey. A change in the coherence/backscatter also affects the amount of detected bare soil. The bare soil is shown to increase during and after the flooding due to the increase in surface texture caused by the storm, primarily over water bodies. As satellite radar sensitive to target texture, areas that became textured were misclassified as bare soil. This can be avoided by applying a harsher filter over the detected water bodies; however, this information can also be used as a proxy for surface conditions. The largest amount of bare soil was detected in the August 24, 2017 (20170824) and the Augst 30, 2017 (20170830) images, indicating that the storm was most active at these times.

Chapter 4: Discussion

4.1. Deformation Analysis

The water level change from 2006-2017 and 3D GPS velocity vectors in Figure 14 shows a good spatial correlation. A substantial decrease in the groundwater level will cause subsidence, reduce the strength of the aquifer, and possibly lead to non-reversible deformation. Likewise, an increase in the overbearing load will cause subsidence and may cause sediment compaction/porosity loss in the aquifer system (Galloway et al., 1999; Kasmarek et al., 2009; Kasmarek, 2012). Figure 17 shows a zoomed in view of the GPS vertical velocity surface over Harris County. Figure 17a is overlaid with average rainfall contours from 2011-2016, where the southeast portion of the map is receiving the highest average rainfall and the northwest portion is receiving the lowest amount of rain. This difference in rainfall indicates that the aquifer system to the southeast is more resistant to loading. Figure 17b is overlaid with ground water changes from 2006-2017 and shows northern Harris County undergoing as much as -16 mm/yr of vertical deformation. This is coupled with a decrease in the ground water level of over 10 m between 2006-2017. However, long-term ground water trends, such as in Figure 7a and 7b, show an increase in the ground water level.

While this study did not analyze time-series trends for porosity data or soil compaction, it is likely that the observed deformation over northern Harris County is linked to some degree of inelastic deformation. Similar trends are also observed over the Woodlands area (gray star in Figure 17) in Montgomery County. The Woodlands area has experienced a groundwater level drop of over 20 m since 2006-2017, and over 40 m of groundwater level loss from 1990-2017. Yet the current observed subsidence rates are relatively small, only about 6-4 mm/yr. Compared to northern Harris County, this area has experienced more than double the groundwater level loss but has ¼ the subsidence rate. If inelastic deformation is taking place, it is likely only in the

beginning stages in this area. Regardless, continued groundwater pumping over the Woodlands may soon result in this area resembling northern Harris County and experiencing increased rates of subsidence.

Further south there is the increase of groundwater coupled with positive uplift rates. A water level high concentrated over southeast Harris County shows both large vertical (~1-3.5 mm/yr) and horizontal (~3.5 mm/yr) motion. These rates of motion are much higher than similar areas that have also undergone an increase in water level, therefore that cannot be attributed solely to increased groundwater level. Instead, high motion over this area is best explained by the fact that League City happens to overly multiple salt domes along with the Hastings Oil Field. Salt domes being lighter than the surrounding rocks, rise to the surface and cause uplift along with associated faulting (Engelkemeir et al. 2008; Engelkemeir et al., 2010; Khan et al., 2014). The salt domes here also appear to be some the most active, moving at ~3.5 mm/yr along a southern track. However, the Hasting Oil Field is currently operated by Denbury Resources Incorporated, which uses CO_2 injection in the CO_2 Enhancement Oil Recovery (CO_2 EOR) method to recover oil not extracted previously with traditional methods (Denbury Inc., 2011). The CO_2 injection method has previously been shown to increase surface deformation, primarily by causing positive uplift along the vertical direction (Cappa and Rutqvist, 2012; Karegar et al., 2015). For southeast Texas, Karegar et al., 2015 also noted a high degree of correlation between CO_2 injection pressure and observed uplift. Vertical motion in this area ranges from 1-3.5 mm/yr with surrounding regions that have also undergone an increase in ground water are showing no vertical motion or slight subsidence ranging from 1-2 mm/yr. While it is difficult to quantify the amount of vertical motion associated with CO_2 injection or salt dome movement due to GPS being a cumulative measurement, it is likely that the deformation in this area is primarily caused by these factors.

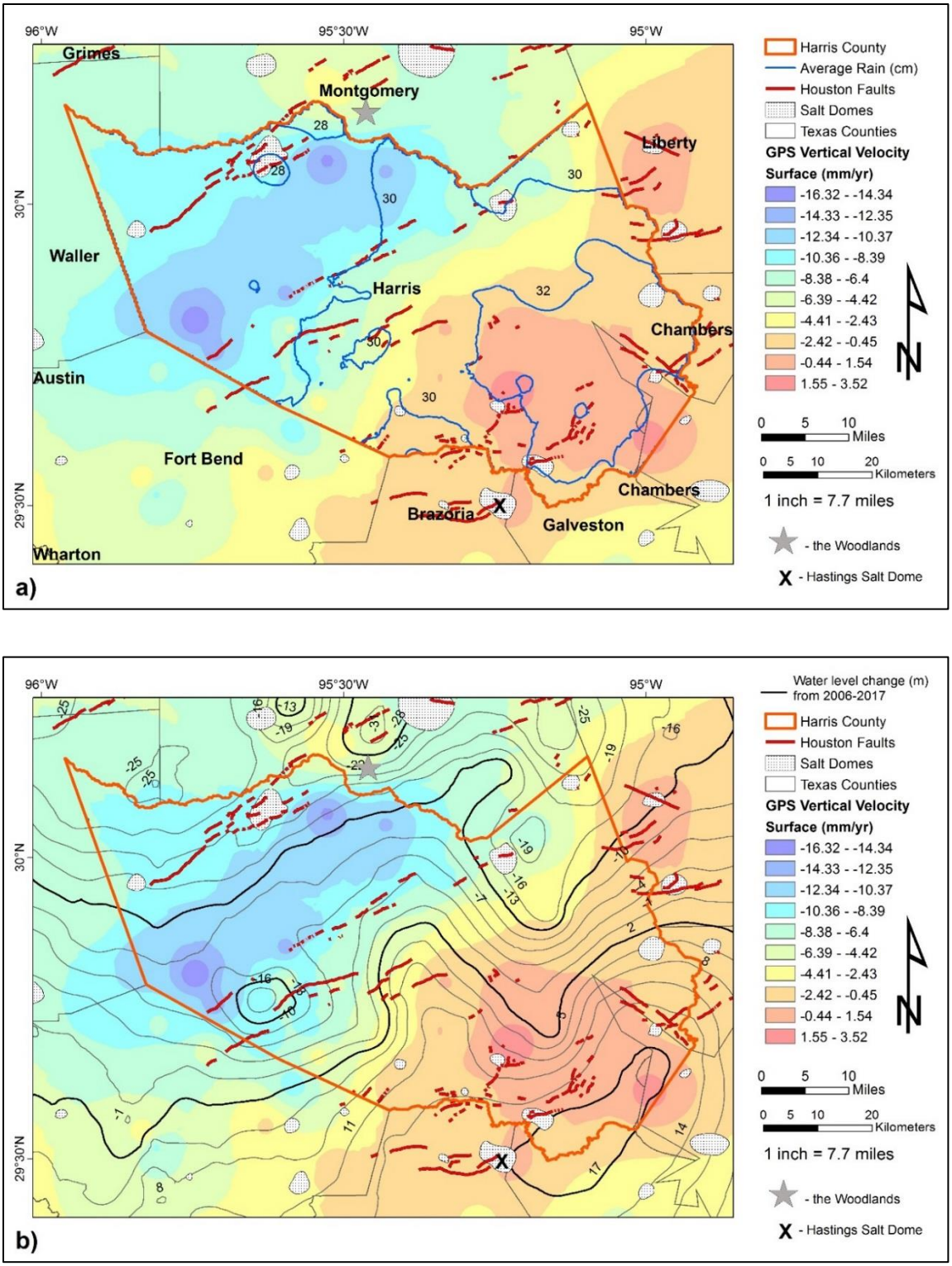

Figure 17: GPS Vertical Velocity Vector Surface (cm/yr) with Water Level Change contours (m); X over Hasting salt dome/League City, gray star over Woodlands area. ***a)*** *Average rain from 2011-2016 showing less rain/smaller loading capacity over northern Harris County and more rain/higher loading capacity over southeast Harris County/Hastings salt dome.* ***b)*** *Ground water level change*

contours from 2006-2017 show uplifting area in southeast Harris County/Hastings salt dome where salt dome movement ranges from 1-3.5 mm/yr upwards. Area between Addick's Conroe and Long-Point-Eureka-Heights Fault systems is likely showing positive uplift due to faults, but uplift is hard to quantify. Northern Harris County (blue circle) is undergoing deformation and subsiding at ~3.7mm/yr. The Woodlands (gray star) is similar to League City and also affected by salt domes whose uplift of up to 5mm/yr is counteracting the 1mm/yr subsidence. In the future this area may resemble northern Harris County.

The high degree of visual correlation between the GPS velocity vectors and the water level change from 2006-2017 also reveals spatial variation in the displacement rate across the fault systems. As shown in Figure 17b, the Long Point-Eureka Heights faults system shows lower rates of vertical deformation towards to east associated with an increase in the water level. Most faults in the Houston area act as fluid barriers; an increase in fluid pressure on one side of the fault is reducing the pressure difference that was previously experienced in this area by long-term groundwater pumping (Kreitler, 1977; Holzer, 1976; Bubey, 2002). Fault related differential compaction is being likely mitigated by an increase in the fluid pressure towards the east, causing the different deformation rates from east to west (Kreitler, 1977; Holzer, 1976).

The predicted groundwater withdrawal increase has further implications for fault reactivation as noted over the Long-Point Eureka-Heights Fault System (Kreitler, 1977; Holzer, 1976). Faults in the Houston area were largely inactive until the last century, with most acting as fluid barriers. However, as pore pressure is reduced and sediment is compacted in the fluid production side due to groundwater pumping, the differential pressure is transferred to the surface and the fault is reactivated (Kreitler, 1977; Holzer, 1976; Burbey, 2002). Fault movement is thus highly correlated with aquifer elasticity in the Houston area. If current ground pumping trends continue, it is likely that faults in the Woodlands and southwest Harris County will become reactivated.

The GPS vertical velocity surface shows the best water level change correlation, and shows uplift over salt domes in southeast Harris County of up to 3.5 mm/yr. Negative vertical motion, or subsidence, is shown primarily over northern Harris County and central Montgomery County as low as -16.3 mm/yr. Areas along the western portion of the Long Point Eureka Heights fault system are showing subsidence ranging from ~10-6 mm/yr, whereas the eastern section only shown subsidence ranging from 4-0.45 mm/yr. This corresponds to an increase in ground water towards the southeast. Smaller subsidence is shown over Fort Bend County of about 4-6 mm/yr, but the lack of well distributed data in this region makes it hard to distinguish the actual extent of the affected area. The high correlation of the ground water trends and vertical deformation data reveals that the resent observed vertical deformation is primarily linked to low frequency variation in the aquifer system, which can cause inelastic deformation.

4.2. Predicted Surface Deformation

The groundwater level prediction degrades around winter 2021, therefore the water level change was only calculated for 2017-2021 (Figure 18). The predicted images all show an increasing area of low water level, particularly over northern Houston, and the Woodlands areas, with a small area towards the south overlaying the most salt domes and increasing water level. The water level change and vertical GPS displacement from 2017-2021 is shown in Figure 18; the predicted groundwater level change largely resembles the pattern observed in the water level change from 2006-2017 (Figure 5b). The Hastings area shows a predicted 1 cm of uplift, largely due to the active salt dome nearby and CO_2 injection.

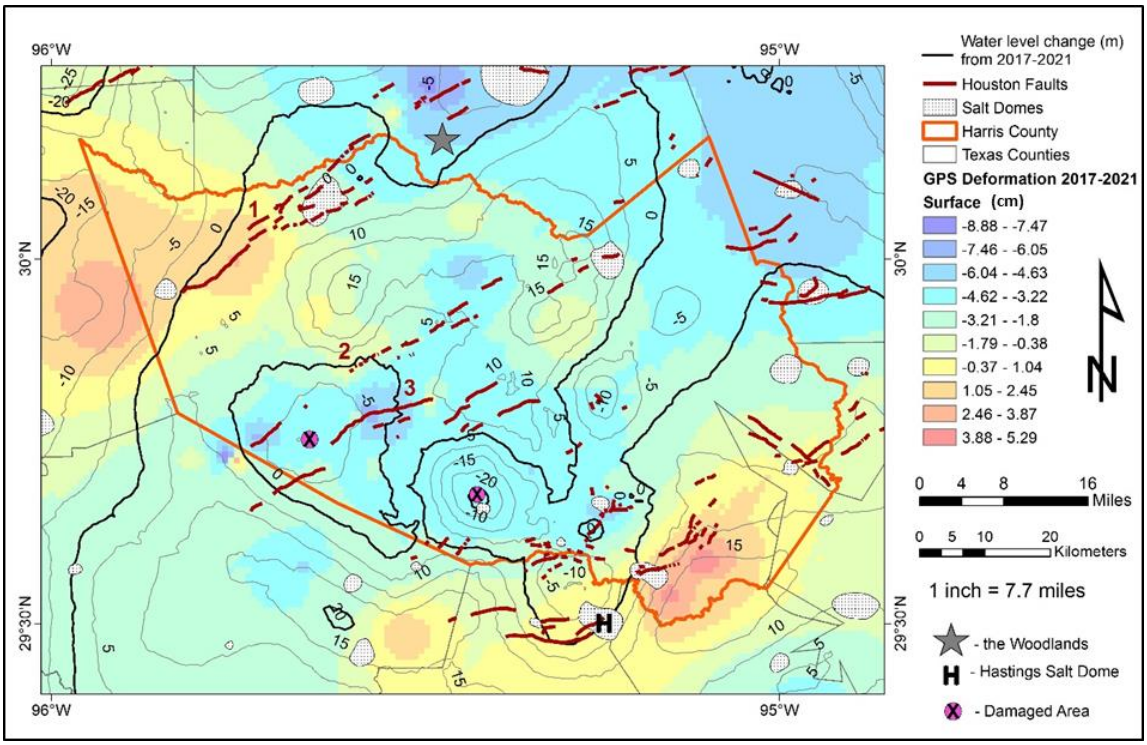

Figure 18: Predicted surface deformation and groundwater level change from 2017-2021 where H is over Hastings Salt Dome/Oil Field, star over Woodland area, cross-hair over damaged area in southwest Harris County, and three main fault systems: 1) Hockley-Conroe Fault System, 2) Addick's Fault System, and 3) the Long Point-Eureka Heights Fault System. The 4-year prediction shows a continued decrease in the water level over the Woodlands area and various parts of Harris County. Deformation is predicted to increase significantly over the damaged areas in southwest Harris County.

The Woodlands area also shows ~3-7 cm of subsidence alongside the predicted water level decrease of ~5 m. Southwest Harris County shows two worrying developments of increased subsidence and decreased water level (cross-hairs in Figure 18). In Figures 14, these areas are relatively small and just starting to show negative water level concentric contours. Further south, the Hastings Salt Dome shows continued increase in water level and increased uplift. This area of uplift is predicted to increase towards areas that are undergoing slight ground water level loss. The active salt dome coupled with CO_2 injection is predicted to overcome the subsidence associated with groundwater withdrawal over these areas in the next 4 years. Uplift is also

predicted to occur in the northwest corner of the map; however, this is likely an interpolation artifact due to poor data coverage outside of Harris County. This prediction indicates that if water withdrawal rates continue at their current level, deformation as seen in northern Houston will likely also occur in the Woodlands and possibly over southwest Harris County; areas undergoing subsidence will continue to expand but be slightly offset by uplift associated with CO_2 injection and salt domes in the south.

4.3. Inconsistencies in GPS Data

While raw GPS dataset that was processed independelty in this study provided many more GPS observations, they were generally of lower quality than the NGL dataset largely due to the reduced time of observation. For example, PAM stations make up most of the observations in this dataset. However, as these are mobile stations that are only intermittently operating for a few days to a few weeks a year, they are much less reliable than CORS data and more likely to capture seasonal variation rather than long-term displacement rates (Blewitt and Lavallée, 2002; Blewitt et al., 2016). This can cause variability between measurements and bias velocity estimates even over nearby areas, as can be seen by the different pointing directions in Figure 19a. For PAM stations, large seasonal variation is a primary concern and cannot be filtered out due to limitations in temporal coverage. Even with data collected across multiple years, the source signal is likely aliased, and GPS derived velocity results are of reduced accuracy when compared to CORS stations (Blewitt and Lavallée, 2002; Blewitt et al., 2016).

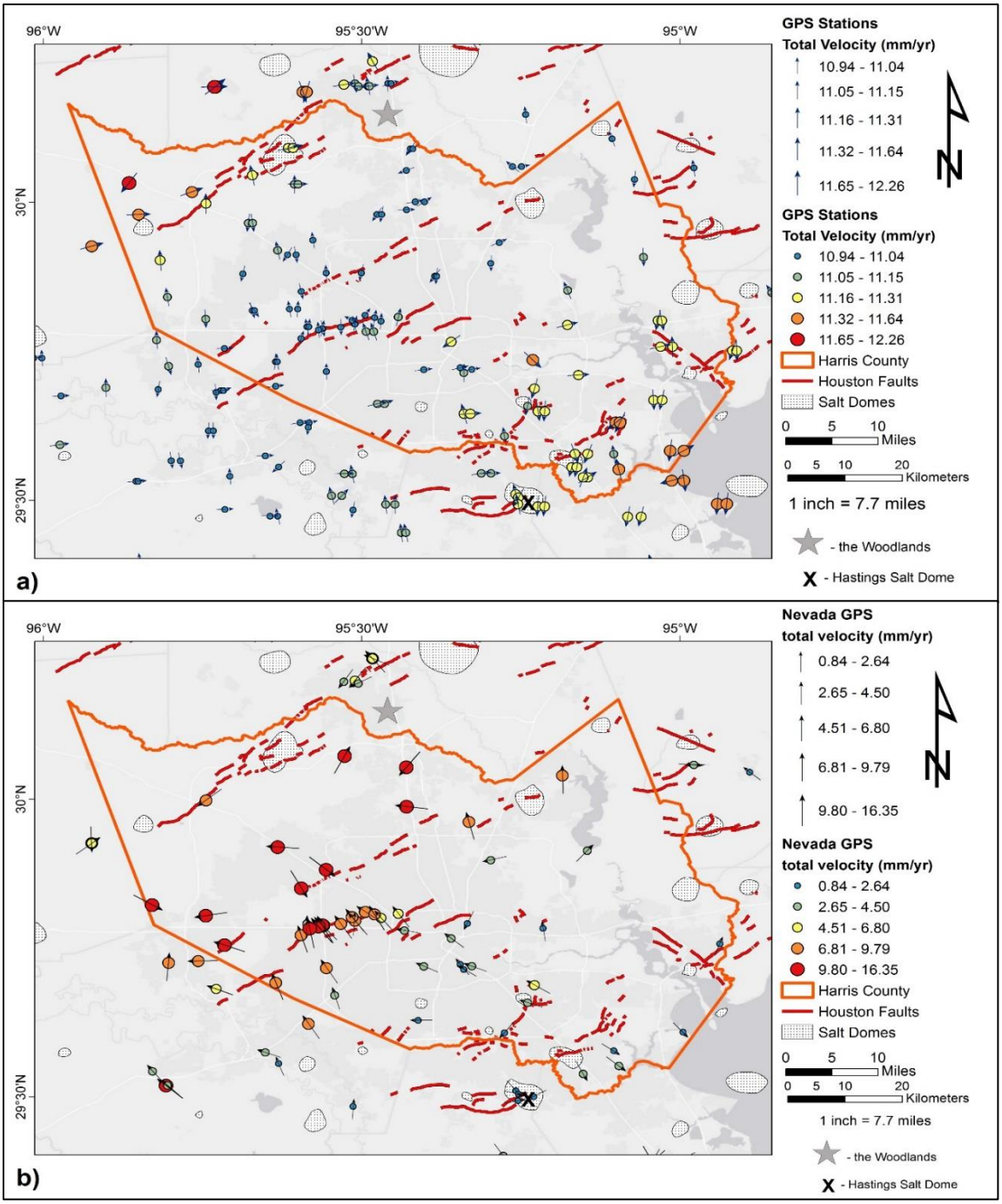

Figure 19: Plotted GPS total velocity in mm/yr for a) independently processed data and b) Nevada data. Difference between the temporal span, reference frames, and processing methods resulted in different GPS velocity estimates. However, both datasets show relatively similar trends of southern moving vectors over southeast Harris County and northern moving vectors over the Long Point-Eureka Heights fault system.

On the other hand, a large part of CORS data over central Harris County are relatively new and only span back to 2013 or later. In 2011 the Houston area CORS GPS network consisted of only 38 stations, 6 of which were no longer operational. To overcome the poor data distribution, fifteen new stations were added in 2012 and 2013 respectively, followed by 28 stations in 2014, and 18 stations in 2015 (Figure 20). No new stations were added following 2015. Out of the 118 CORS stations to have been established throughout the greater Houston area, only 98 are still operational as of June 2019. The recent growth of the Houston CORS network meant that at the time of processing in 2017, only 25 out of the 107 operating stations had data spanning back more than 6 years. In other words, only 25 stations could provide robust GPS solutions not affected by seasonal variation or other factors.

The method for calculating station velocity is also not as robust as the MIDAS trend estimator. A least-squares trend works well for normally distributed data; however, performance has been shown to degrade in the presence of outliers, data discontinuities, and abrupt jumps or steps in the data. For short time-series, the least-squares method has also been shown to produce velocity estimates correlated with seasonal variation (Blewitt et al., 2016). On the other hand, the MIDAS estimator works by calculating the median between data pairs separated by 1 year, which reduces the effects of seasonal variation and step discontinuities in the data. MIDAS reduces velocity bias by removing data outliers and recomputing the median; trend uncertainty is also computed in the final output (Blewitt et al., 2016). Tested MIDAS velocities have a root-mean-square (RMS) accuracy of +0.33 mm/yr in the horizontal and +1.1 mm/yr in the vertical directions respectively. The least-squares and MIDAS velocities have been shown to vary by up to 3.5 mm/yr in synthetic tests; this number may be higher for actual GPS data (Blewitt et al., 2016).

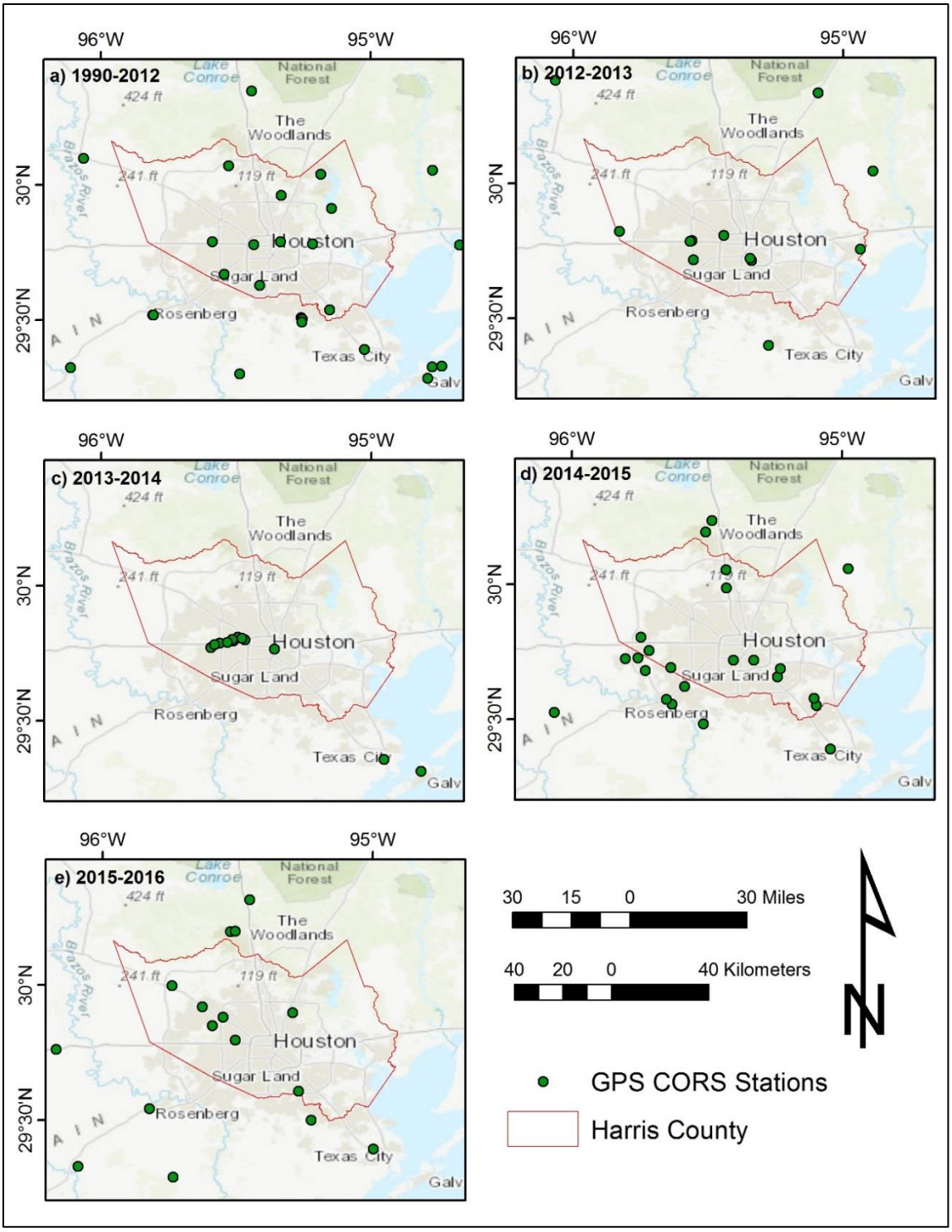

Figure 20: Time series view of CORS GPS stations added each year across the greater Houston area. Sub-views showing stations added during that time period where a) 1990-2012, b) 2012-2013, c) 2013-2014, d) 2014-2015, and e) 2015-2015.

Due to the increased temporal coverage and more robust processing methods, this study adopted the GPS data available from NGL and used these for interpretation alongside the ground and surface water data. However, processed GPS results and images are included in the appendix section for reference. Differences between the NGL GPS data and the GPS data processed in this study arise due to the difference in temporal coverage, spatial reference frame, and processing methods. Even with these differences, it is to be noted that CORS stations have relatively similar movement directions across both datasets. Southeast Harris County showed southern moving vectors, whereas central Harris County shows northern moving vectors along the Long Pont-Eureka Heights fault system.

4.4. Radar Mapping Validation

Radar classification results were validated by comparing to urban areas from the City of Houston GIS Portal and derived flooded extents made up of flooded areas and flooded vegetation to USGS in-situ measurements as show in Figures 21-23. Building footprints for the city of Houston from August of 2016 were downloaded from the City of Houston GIS Portal. The dataset is comprised of 649,510 recoded buildings listed as either existing, demolished, new, possibly changed, or unknown. These data were imported into ArcMap along with the urban classes derived from the August 18, 2017 (20170818) image. This image was selected because it was the furthest from the flooding occurrence and thus had the least amount of water or surface texture that might obscure features. The difference in resolution, spatial extent, and time between the datasets did not allow for a direct one-to-one comparison; only a qualitative analysis could be made. However, the radar imagery as shown in Figure 21, shows good agreement with the building footprint data over both residential and urban areas. While the radar data has a resolution of 14x14 m, it is still able to detect sub-pixel features such as houses and buildings over both residential (Figure 21a) and urban areas (Figure 21b).

The two datasets have good agreement overall, but the detection of urban features becomes more difficult over complex targets such as thick vegetation where both endmembers may exhibit high coherence and backscatter. This is primarily an issue in residential areas and does not affect the larger urban core of the city of Houston.

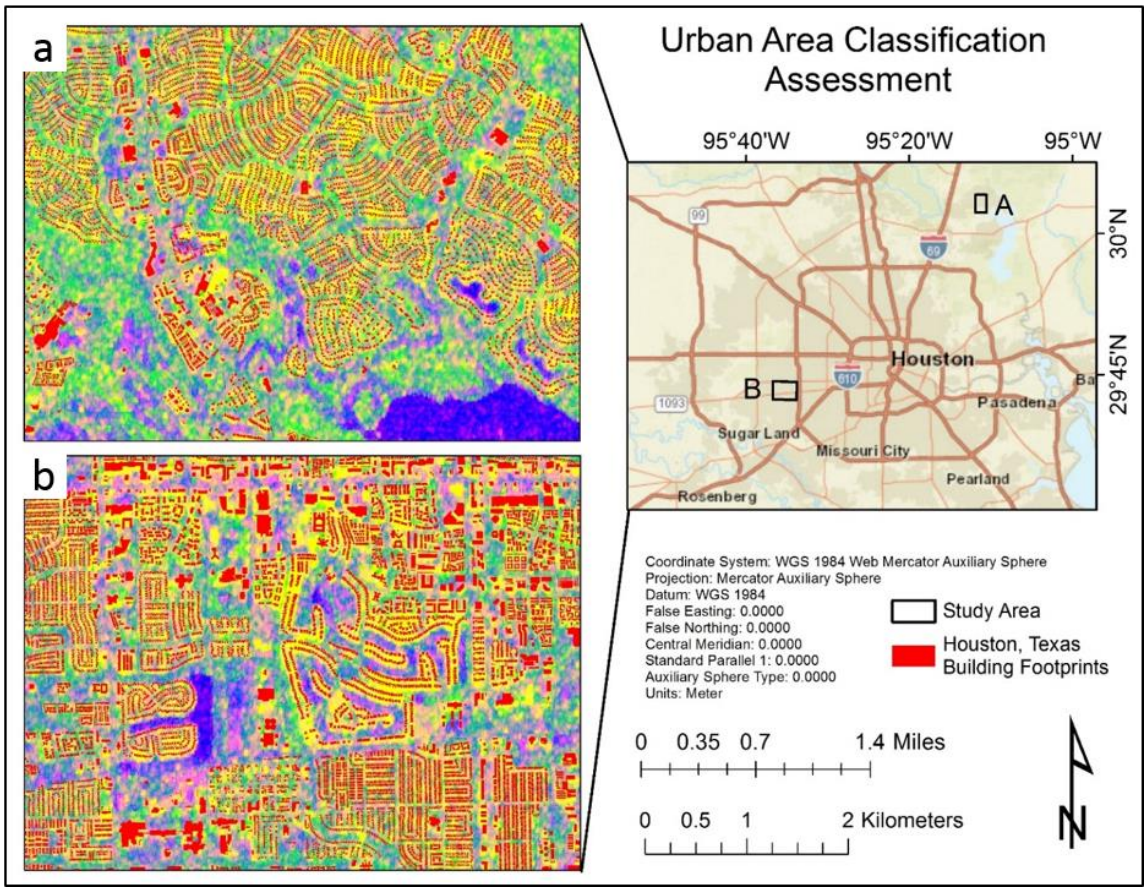

Figure 21: Urban area classification validation showing the August 18, 2017 radar imagery in RGB: coherence, mean Sigm0, and difference Sigma0 where blue areas are water, red are bare soil/streets, green is vegetation, and yellow corresponds to urban areas. Red polygon indicates building footprint data from the City of Houston GIS Portal. Study areas over primarily residential (a) and primarily urban (b) environments are shown for comparison. While the radar data has a resolution of 14x14 m, it is still able to detect sub-pixel features such as houses and buildings. The two datasets have good agreement overall, but the detection of urban features becomes more difficult over complex targets such as thick vegetation.

Watson et al., 2018 provide in-situ flood measurements in shapefile format over various rivers across the Houston area. For this study, data over the upper Brazos River and the San Jacinto River were analyzed in ArcMap as they had the best image overlap. The cumulative flooded areas derived from all processed imagery over unobstructed areas show proper alignment with the in-situ measurements, as shown in Figures 22 and 23. Small scale features such as ox-bow lakes and inundated streets are readily made out. Discrepancies between the satellite and in-situ measurements arise over more complex targets, primarily over vegetation. As vegetation is a complex target and changes rapidly, only the August 30, 2017 (20170830) and September 5, 2017 (20170905) images were used for comparison with the in-situ data; these dates correspond to the most severe flooding. Comparing the flooded vegetation, it is more detectable in images when surface texture is not a dominate component and where there is no thick canopy. While image for August 30, 2017 (20170830) experienced more flooding, flooded vegetation is much harder to detect because of the tumulus ground conditions. In fact, a similar outline like the USGS in-situ measurements in Figures 22 and 23 can be faintly made out on the difference images of Augut 18, 2017 (20170818) and August 24, 2017 (20170824).

A possible method to reduce speckle while preserving image quality could be coregistation of all images and applying a temporal filter, as demonstrated by White et al., 2015 for wetland mapping. Figures 22 and 23 lack detected flooded vegetation along the river edges, but farmlands are well detected. This phenomenon likely occurs because most farm crops lack a thick canopy that acts to block the radar signal, unlike the typical environment along riverbanks. Flooded vegetation in these areas would be more detectable with a longer wavelength system such as L-band which would allow for further tree canopy penetration; the satellite image would also be less sensitive to small-scale backscatter changes (Wegmuller

and Werner, 1995; Henderson and Lewis, 1998). Vegetation mapping may similarly be improved by utilizing a different polarization such as HH or HV (Xia and Henderson, 1997).

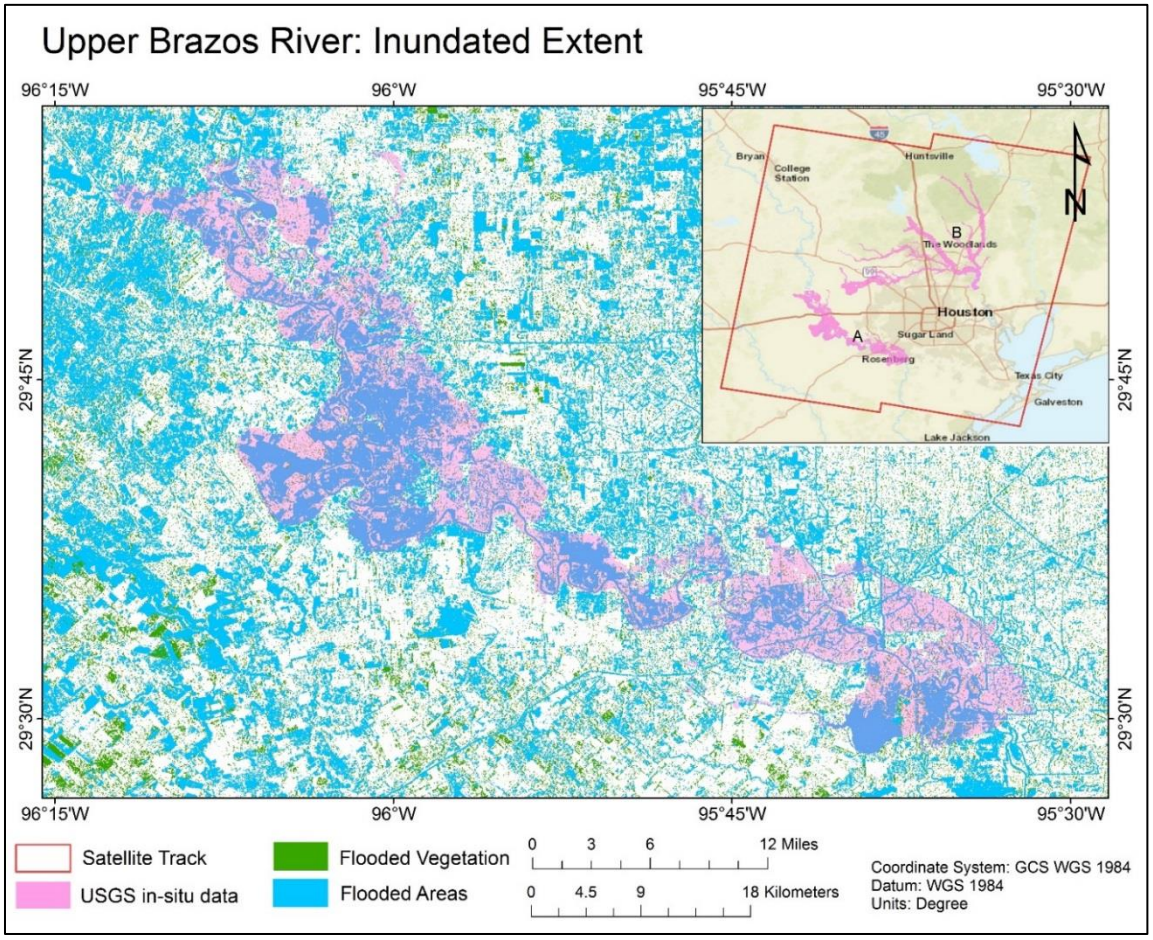

Figure 22: The inundated extent of the Upper Brazos River from in-situ measurements shown in pink, and radar data shown in blue and green. The blue corresponds to the cumulative flooded areas detected across all imagery, while the green corresponds to areas of flooded vegetation from August 30, 2017 (20170830) and September 5, 2017 (20170905). Flooded extents of the A) Upper Brazos River and B) the San Jacinto River are shown in the upper right-hand sub-view.

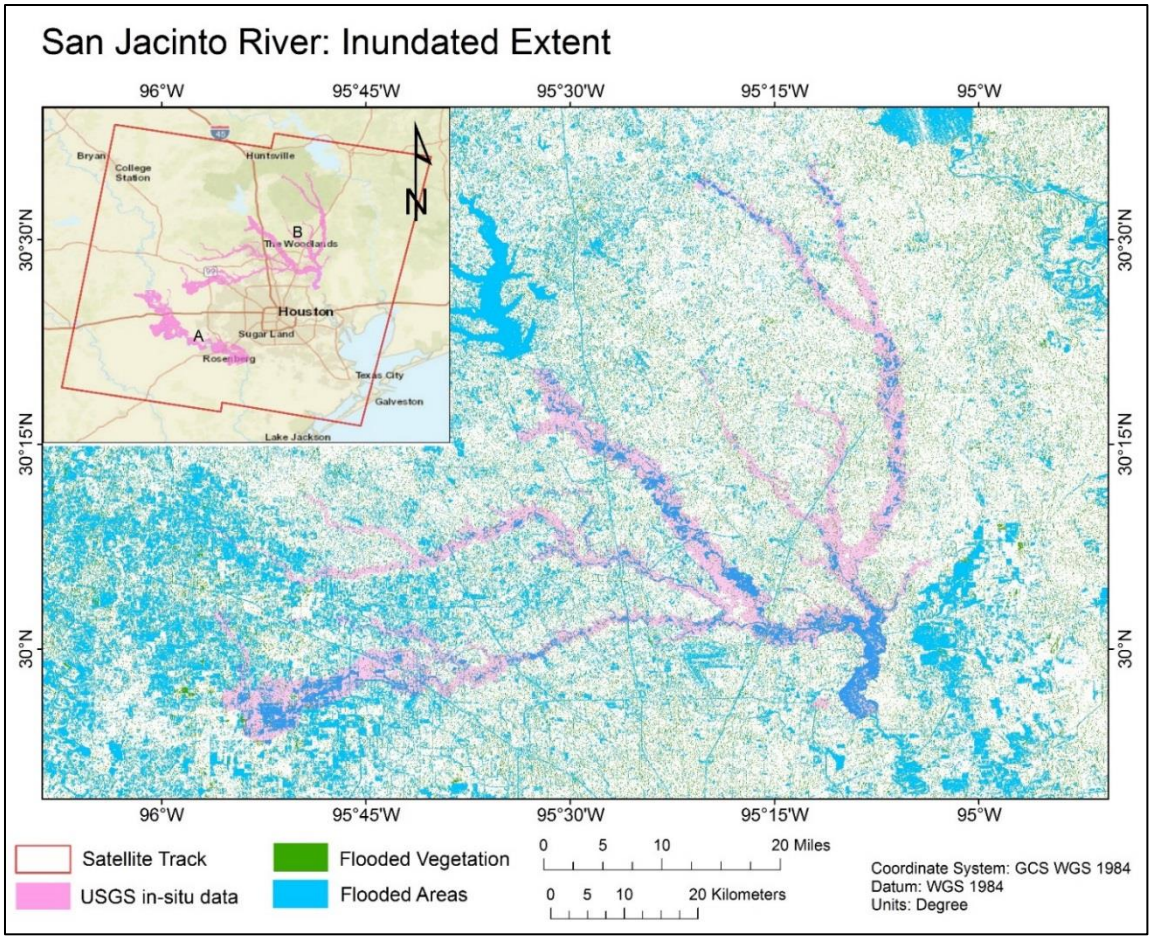

Figure 23: The inundated extent of the San Jacinto River from in-situ measurements show in pink, and radar data shown in blue and green. The blue corresponds to flooded areas, or open water, while the green corresponds to areas of flooded vegetation from August 30, 2017 (20170830) and September 5, 2017 (20170905). Flooded extents of the A) Upper Brazos River and B) the San Jacinto River are shown in the upper right-hand sub-view.

While this mapping approach shown promise, it is still dependent on the user defined threshold. Similarly to the gray-threshold technique, the threshold is the single most important factor for improving accuracy and providing quality results in a short time. The processing scheme could be improved by creating stricter guidelines for classification or by utilizing universal threshold standards. While not tested in this work, unsupervised and supervised classification algorithms might also be employed for a consistent and semi-automated approach. However, this required knowledge of the number of endmembers present, their spatial distribution, etc., which

may or may not be available. To maintain a self-consistent approach, the use of neural networks and machine learning may be utilized given that the study area is large enough to be detected (Li et al., 2019). However, even with such sophisticated methods, it may still be challenging to accurately classify images acquired at different times due to the high variability of backscatter. The lack of quantitative error analysis to this and other remote sensing-based flood detection techniques is another hurdle to overcome. Currently, there is only limited ground-truth data available that makes it hard to discern the performance of different thresholds/methods in less than general terms.

However, despite the following limitations space borne radar data shows great potential for mapping natural hazards like floods and can provide real-time solutions to aid in decision making. Unlike optical remote sensing techniques, it can penetrate though storm clouds and tree canopy; it does not require daytime condition to operate. By exploiting the high temporal resolution of data, the change in backscatter and coherence components between two or more images can be derived. These data can be used to quickly identify and map endmembers, similarly to multispectral datasets. The large availability of data also allows for time-series analysis and change detection. Additional benefits of radar data include being able to map the surface deformation and soil moisture associated with floods, without the need for time consuming in-situ measurements. As the data are acquired from space, it is not prone to shortages associated with natural disasters. Thus, SAR data and the technique presented in this work will likely become an indispensable tool for flood analysis and other natural hazard studies.

Chapter 5: Conclusions

The Houston area consists of both geologic and anthropogenic elements which contribute to the observed deformation. Naturally occurring southern moving salt domes, thrust faults, storms, flooding, and human-induced subsidence all contribute to surface deformation. Currently, the Houston area is experiencing deformation in northern Harris County due to excessive groundwater withdrawal, which likely is or may become non-reversible in the future. This has increased susceptibility to subsidence from flooding and storms, events that are likely to become more common as global climate patterns change. Salt domes and CO_2 injection are primarily controlling deformation rates towards the south. The local aquifer system located in Houston's southwest corridor is currently more robust, having suffered much less ground water withdrawal. However, prolonged flooding in this area, such those caused by Hurricane Harvey, pose a risk of sediment compaction and flood-induced subsidence. Predicted surface deformation in the next four years shows the Woodlands and southwest Harris County undergoing subsidence, which may also have implications for fault reactivation.

REFERENCES

Altamimi, Z., Métivier, L., & Collilieux, X. (2012). ITRF2008 plate motion model. *Journal of Geophysical Research: Solid Earth*, *117*(B7).

ARIA Flood Extent Map of Harvey from Sentinel-1 SAR Data. NASA Earth Science Disaster Program. Source: https://disasters.nasa.gov/hurricane-harvey-2017/aria-flood-extent-map-harvey-sentinel-1-sar-data

Blake, E. S., & Zelinsky, D. A. (2017). National Hurricane center tropical cyclone report: Hurricane Harvey. *AL092017, National Oceanic and Atmospheric Administration*.

Blewitt, G., & Lavallée, D. (2002). Effect of annual signals on geodetic velocity. *Journal of Geophysical Research: Solid Earth*, *107*(B7), ETG-9.

Blewitt, G., Hammond, W. C., & Kreemer, C. (2018). Harnessing the GPS data explosion for interdisciplinary science. *Eos*, *99*.

Blewitt, G., Kreemer, C., Hammond, W. C., & Gazeaux, J. (2016). MIDAS robust trend estimator for accurate GPS station velocities without step detection. *Journal of Geophysical Research: Solid Earth*, *121*(3), 2054-2068.

Blewitt, G., Kreemer, C., Hammond, W. C., & Goldfarb, J. M. (2013). Terrestrial reference frame NA12 for crustal deformation studies in North America. *Journal of Geodynamics*, *72*, 11-24.

Burbey, T. J. (2002). The influence of faults in basin-fill deposits on land subsidence, Las Vegas Valley, Nevada, USA. *Hydrogeology Journal*, *10*(5), 525-538.

Cappa, F., & Rutqvist, J. (2012). Seismic rupture and ground accelerations induced by CO2 injection in the shallow crust. *Geophysical Journal International*, *190*(3), 1784-1789.

Chini, M., Pelich, R., Pulvirenti, L., Pierdicca, N., Hostache, R., & Matgen, P. (2019). Sentinel-1 InSAR Coherence to Detect Floodwater in Urban Areas: Houston and Hurricane Harvey as A Test Case. *Remote Sensing*, *11*(2), 107.

City of Houston GIS Portal. The City of Houston, Official Site for Houston, Texas. Source: http://mycity.houstontx.gov/home/index.html.

Dartmouth Flood Observatory. Space-based Measurement, Mapping, and Modeling of Surface Water For Research, Humanitarian, and Water Management Applications. https://floodobservatory.colorado.edu/

Denbury Resources Incorporation. (2011). Handout.pdf. http://www.midwesterngovernors.org/EOR/Denbury_West_Hastings_Field_Unit_

Engelkemeir, R. M., & Khan, S. D. (2008). Lidar mapping of faults in Houston, Texas, USA. *Geosphere*, *4*(1), 170-182.

Engelkemeir, R., Khan, S. D., & Burke, K. (2010). Surface deformation in Houston, Texas using GPS. *Tectonophysics*, *490*(1), 47-54.

Galloway, D. L., Jones, D. R., & Ingebritsen, S. E. (1999). *Land subsidence in the United States* (Vol. 1182). US Geological Survey.

Giustarini, L., Hostache, R., Matgen, P., Schumann, G. J. P., Bates, P. D., & Mason, D. C. (2012). A change detection approach to flood mapping in urban areas using TerraSAR-X. *IEEE transactions on Geoscience and Remote Sensing*, *51*(4), 2417-2430.

Grey, W. M. F., Luckman, A. J., & Holland, D. (2003). Mapping urban change in the UK using satellite radar interferometry. *Remote sensing of Environment*, *87*(1), 16-22.

Henderson, F. M., & Lewis, A. J. (1998). Principles and applications of imaging radar. Manual of remote sensing: Volume 2.

Holzer, T. L. (1976, December). Ground failure in areas of subsidence due to ground-water decline in the United States. In *Proceedings of the Anaheim Symposium*.

Karegar, M. A., Dixon, T. H., Malservisi, R., Yang, Q., Hossaini, S. A., & Hovorka, S. D. (2015). GPS-based monitoring of surface deformation associated with CO 2 injection at an enhanced oil recovery site. *International Journal of Greenhouse Gas Control*, *41*, 116-126.

Kasischke, E. S., Melack, J. M., & Dobson, M. C. (1997). The use of imaging radars for ecological applications—a review. *Remote sensing of environment*, *59*(2), 141-156.

Kasmarek, M. C. (2012). *Hydrogeology and simulation of groundwater flow and land-surface subsidence in the northern part of the Gulf Coast aquifer system, Texas, 1891-2009* (No. 2012-5154). US Geological Survey.

Kasmarek, M. C., & Lanning-Rush, J. (2004). *Water-level altitudes 2004 and water-level changes in the Chicot, Evangeline, and Jasper aquifers and compaction 1973-2003 in the Chicot and Evangeline aquifers, Houston-Galveston region, Texas* (No. 2004-1084). US Geological Survey.

Kasmarek, M., Gabrysch, R., and Johnson, M. (2009). Estimated landsurface subsidence in Harris County, Texas, 1915–17 to 2001, USGS Sci. Invest. Map 3097, USGS, Reston, VA.

Kearns, T. J., Wang, G., Bao, Y., Jiang, J., & Lee, D. (2015). Current land subsidence and groundwater level changes in the Houston Metropolitan Area (2005–2012). *Journal of Surveying Engineering*, *141*(4), 05015002.

Khan, S. D., Huang, Z., & Karacay, A. (2014). Study of ground subsidence in northwest Harris county using GPS, LiDAR, and InSAR techniques. *Natural hazards*, *73*(3), 1143-1173.

Khan, S. D., Stewart, R. R., Otoum, M., & Chang, L. (2013). A geophysical investigation of the active Hockley Fault System near Houston, Texas. *Geophysics*, *78*(4), B177-B185.

Kreitler, C. W. (1977). Fault Control of Subsidence, Houston, Texas a. *Groundwater*, *15*(3), 203-214.

Lee, J. S., & Pottier, E. (2009). *Polarimetric radar imaging: from basics to applications*. CRC press.

Li, Y., Martinis, S., & Wieland, M. (2019). Urban flood mapping with an active self-learning convolutional neural network based on TerraSAR-X intensity and interferometric coherence. *ISPRS Journal of Photogrammetry and Remote Sensing*, *152*, 178-191.

Martinis, S., & Rieke, C. (2015). Backscatter analysis using multi-temporal and multi-frequency SAR data in the context of flood mapping at River Saale, Germany. *Remote Sensing*, *7*(6), 7732-7752.

Meta, A., Prats, P., Steinbrecher, U., Mittermayer, J., & Scheiber, R. (2008, June). TerraSAR-X TOPSAR and ScanSAR comparison. In *7th European Conference on Synthetic Aperture Radar* (pp. 1-4).

Milliner, C., Materna, K., Bürgmann, R., Fu, Y., Moore, A. W., Bekaert, D., ... & Argus, D. F. (2018). Tracking the weight of Hurricane Harvey's stormwater using GPS data. *Science advances*, *4*(9), eaau2477.

Natural Resources Canada PPP direct tool. (2016). https://www.nrcan.gc.ca/earth-sciences/geomatics/geodetic-reference-systems/tools-applications/10925#ppp

Pitman, J. K. (2010). Reservoirs and petroleum systems of the Gulf Coast.

Potin, P., Rosich, B., Grimont, P., Miranda, N., Shurmer, I., O'Connell, A., ... & Krassenburg, M. (2016, June). Sentinel-1 mission status. In *Proceedings of EUSAR 2016: 11th European Conference on Synthetic Aperture Radar* (pp. 1-6). VDE.

Qu, F., Lu, Z., Zhang, Q., Bawden, G. W., Kim, J. W., Zhao, C., & Qu, W. (2015). Mapping ground deformation over Houston–Galveston, Texas using multi-temporal InSAR. *Remote Sensing of Environment*, *169*, 290-306.

Sentinel-1. ESA Sentinel Online. Source: https://sentinel.esa.int/web/sentinel/missions/sentinel-1/overview.

Shen, X., Wang, D., Mao, K., Anagnostou, E., & Hong, Y. (2019). Inundation Extent Mapping by Synthetic Aperture Radar: A Review. *Remote Sensing*, *11*(7), 879.

Torres, R., Snoeij, P., Geudtner, D., Bibby, D., Davidson, M., Attema, E., ... & Traver, I. N. (2012). GMES Sentinel-1 mission. *Remote Sensing of Environment*, *120*, 9-24.

US Department of Commerce, NOAA, National Weather Service. (2017, June 26). National Weather Service National Headquarters. Retrieved September 29, 2017, from http://forecast.weather.gov/product.php?site=NWS&issuedby=LCH&product=PSH&format=CI&pid=201709051836.

Veci, L. (2015). Interferometry Tutorial. *Array Systems. Available online: http://sentinel1. s3. amazonaws. com/docs/S1TBX% 20Stripmap% 20Interferometry% 20with% 20Sentinel-1% 20Tutorial. pdf (accessed on 12 August 2017)*.

Watson, K. M., Harwell, G. R., Wallace, D. S., Welborn, T. L., Stengel, V. G., & McDowell, J. S. (2018). *Characterization of peak streamflows and flood inundation of selected areas in southeastern Texas and southwestern Louisiana from the August and September 2017 flood resulting from Hurricane Harvey* (No. 2018-5070). US Geological Survey.

Wegmuller, U., & Werner, C. L. (1995). SAR interferometric signatures of forest. *IEEE Transactions on Geoscience and Remote Sensing*, *33*(5), 1153-1161.

White, L., Brisco, B., Dabboor, M., Schmitt, A., & Pratt, A. (2015). A collection of SAR methodologies for monitoring wetlands. *Remote sensing*, *7*(6), 7615-7645.

Xia, Z. G., & Henderson, F. M. (1997). Understanding the relationships between radar response patterns and the bio-and geophysical parameters of urban areas. *IEEE Transactions on Geoscience and Remote Sensing*, *35*(1), 93-101.

Zilkoski, D. B., Hall, L. W., Mitchell, G. J., Kammula, V., Singh, A., Chrismer, W. M., & Neighbors, R. J. (2003). The Harris-Galveston coastal subsidence district/national geodetic survey automated global positioning system subsidence monitoring project. In *Proceedings of the US Geological Survey Subsidence Interest Group Conference* (pp. 13-28). US Geological Survey.

APPENDIX

List of GPS Stations processed by the Nevada Geodetic Laboratory (NGL). Data are in NA12 reference frame with velocities calculated using the MIDAS method.

station	start time	stop time	vel_east (mm/yr)	vel_north (mm/yr)	vel_up (mm/yr)	unc_east (mm/yr)	unc_north (mm/yr)	unc_up (mm/yr)
'ADKS'	2002.1383	2019.3457	0.056	0.79	-2.916	0.312	0.368	0.964
'ALEF'	2014.256	2019.4141	-0.271	0.697	-9.286	0.512	0.455	1.989
'ALVN'	2012.46	2017.2402	1.711	-2.441	-3.046	0.329	0.336	1.277
'ANG5'	2003.4442	2019.4114	-0.193	-0.664	-1.743	0.184	0.206	0.814
'ANG6'	2003.4251	2019.4114	0.384	-1.051	-3.226	0.146	0.162	0.714
'AULT'	2015.5537	2019.4141	-0.46	-0.352	-8.777	0.441	0.5	1.967
'CFHS'	2015.5921	2019.4141	-1.021	0.077	-11.659	0.514	0.575	2.308
'CFJV'	2015.77	2019.4141	0.918	-0.735	-11.443	0.616	0.557	2.62
'CMFB'	2014.4066	2019.4141	-1.184	0.448	-5.391	0.356	0.372	1.531
'COH1'	2009.0157	2017.7194	-0.387	1.265	-3.234	0.351	0.285	1.53
'COH2'	2009.0021	2019.4141	-1.639	-0.001	-1.473	0.569	0.358	1.518
'COH4'	2009.0021	2011.6906	-0.32	1.959	1.04	0.81	0.531	2.501
'COH6'	2009.0021	2015.4935	-0.035	1.363	-7.06	0.244	0.284	1.144
'COTM'	2015.0938	2019.4141	-1.706	-0.958	-3.636	0.49	0.551	1.698
'CSTA'	2013.1444	2015.3238	0.254	3.973	-0.642	0.652	0.618	2.345
'CSTE'	2015.3812	2019.4141	-2.439	3.01	-8.959	0.533	0.627	2.121
'DEN1'	2011.7755	2019.2389	1.106	-1.316	-1.722	0.56	0.264	1.12
'DEN2'	2011.7755	2017.0842	2.139	-0.544	-0.782	0.649	0.362	1.202
'DEN3'	2011.7755	2019.2389	0.925	0.19	-0.801	0.466	0.347	1.052
'DEN4'	2015.822	2019.2142	-1.595	-0.842	1.596	0.531	0.472	2.016
'DISD'	2015.4771	2019.4141	-0.935	-0.718	-0.824	0.526	0.443	2.205
'DMFB'	2014.768	2019.4141	-0.768	1.153	-9.69	0.435	0.452	1.873
'DWI1'	2009.3881	2019.4141	0.737	0.643	-2.452	0.292	0.304	1.274
'FSFB'	2014.3682	2019.4141	-0.523	1.291	-1.763	0.408	0.434	1.487
'GAL2'	1997.577	2003.0609	1.158	-1.45	-5.989	0.223	0.353	1.202
'GAL7'	1996.0356	2003.5209	0.833	-0.83	-4.981	0.212	0.271	0.983
'GSEC'	2015.7536	2019.4141	-1.253	-1.8	-2.686	0.71	0.614	2.904
'HCC1'	2012.9117	2019.4141	-1.839	3.332	-10.707	0.418	0.701	1.692
'HCC2'	2013.1362	2019.0856	-2.251	2.452	-11.352	0.575	0.526	2.09
'HPEK'	2014.3929	2018.3929	-1.31	0.459	-13.486	0.38	0.396	1.427
'HSMN'	2013.295	2019.4141	-1.143	1.326	-6.257	0.363	0.328	1.441
'JGS2'	2012.46	2019.4141	-0.723	0.569	-1.613	0.291	0.325	1.235
'KKES'	2015.5948	2019.4141	1.157	-2.007	-13.636	0.621	0.521	2.235
'KPCD'	2016.4381	2019.0801	0.755	0.558	-8.775	1.016	1.006	4.714
'KPCS'	2016.4381	2019.0801	0.034	-0.949	-4.617	1.282	1.539	4.647
'LCBR'	2010.5352	2016.0903	-0.162	0.464	-2.304	0.211	0.203	1.128
'LCI1'	2012.46	2019.4141	-1.287	1.77	-4.402	0.34	0.355	1.344
'LGC1'	2013.5277	2019.4141	0.026	-3.658	-4.363	0.32	0.408	1.386

'LKHU'	1996.3395	2019.3621	0.92	0.999	-2.535	0.272	0.265	0.838
'MDWD'	2013.3005	2019.4141	-0.967	2.865	-7.71	0.5	0.493	1.94
'ME01'	2015.4634	2017.6646	-0.858	-1.057	-1.31	0.851	0.488	2.004
'MEPD'	2014.037	2019.4141	-3.132	1.03	1.162	0.803	0.541	1.301
'MRHK'	2014.3929	2019.4141	-0.841	-0.134	-16.332	0.32	0.326	1.485
'NASA'	2014.1985	2019.1239	2.894	-2.307	-0.817	0.792	1.037	1.69
'NETP'	2002.1355	2019.4141	-0.895	-1.872	-0.085	0.372	0.399	1.006
'OKEK'	2014.5736	2019.4141	0.045	0.504	-8.046	0.465	0.358	1.503
'PA00'	1996.0082	2018.9405	1.3	-2.455	-1.639	0.45	0.897	1.425
'PWES'	2015.217	2019.4114	-2.017	-2.61	-4.045	0.444	0.495	2.526
'RDCT'	2013.5578	2019.4114	-2.19	1.516	-8.38	0.478	0.376	1.498
'ROD1'	2007.0007	2019.4141	0.951	1.765	-14.745	0.191	0.203	1.193
'RPFB'	2014.7707	2019.4114	0.089	1.007	-1.593	0.373	0.538	1.494
'SESG'	2014.6749	2019.4114	-2.082	0.248	-10.873	0.327	0.418	1.809
'SHSG'	2014.7187	2019.4114	-0.698	-0.848	-12.634	0.329	0.388	2.001
'SISD'	2015.1732	2019.4114	-1.188	0.295	-3.831	0.439	0.462	1.956
'SPBH'	2013.3005	2019.4114	-1.559	2.081	-7.849	0.319	0.366	1.666
'STS1'	2012.46	2015.3046	0.541	-1.109	-1.296	0.554	0.539	1.813
'TDAM'	2013.4319	2019.4114	-0.12	-0.074	-3.083	0.302	0.319	1.249
'THSU'	2012.95	2019.4114	-1.268	0.774	0.22	0.396	0.301	1.143
'TSFT'	2013.3771	2019.4114	-1.355	2.288	-7.615	0.415	0.41	1.752
'TXAC'	2011.1211	2019.4141	-0.325	-0.248	-2.368	0.305	0.417	1.011
'TXAG'	2005.577	2019.4141	0.4	0.158	-2.354	0.281	0.27	0.837
'TXB1'	2013.1882	2019.4141	0.136	-1.143	-0.752	0.355	0.442	1.599
'TXB2'	2012.46	2019.4141	-2.326	-2.776	-14.297	0.343	0.446	1.63
'TXB6'	2012.46	2018.2341	0.438	1.128	-1.958	0.424	0.378	1.256
'TXBC'	2009.4018	2019.4141	2.093	-1.82	-2.437	0.266	0.397	1.034
'TXBM'	1996.3368	2013.8042	0.272	-0.093	-3.039	0.246	0.27	0.857
'TXCF'	2012.46	2017.2074	0.477	0.687	-1.01	0.303	0.391	1.566
'TXCM'	2010.4339	2019.4141	-0.002	0.278	-2.834	0.224	0.208	1.127
'TXCN'	2005.577	2019.4141	-0.329	0.701	-14.176	0.188	0.193	0.939
'TXCV'	2012.6626	2019.4141	-0.485	-0.014	-5.725	0.326	0.32	1.21
'TXED'	2009.4209	2019.4141	0.437	-0.359	-0.827	0.227	0.258	1.03
'TXGA'	2005.577	2019.4141	0.349	-0.4	-3.472	0.207	0.231	0.885
'TXGV'	2007.1266	2011.5483	1.021	-0.475	0.067	0.393	0.422	1.494
'TXH2'	2016.0876	2019.2909	0.619	-1.053	1.895	0.628	0.676	3.117
'TXHE'	2005.577	2019.4141	-0.476	0.91	-7.06	0.315	0.312	1.066
'TXHS'	2012.46	2019.4141	-0.667	1.023	-9.244	0.361	0.413	1.672
'TXHU'	1996.0465	2007.9617	-1.215	0.23	-3.462	0.33	0.32	1.386
'TXKO'	2011.7673	2019.4141	-0.114	0.865	-1.024	0.242	0.281	1.23
'TXKY'	2012.46	2017.2402	1.448	-0.801	-11.654	0.478	0.334	1.135
'TXLI'	2005.577	2019.4141	-0.435	0.172	-1.484	0.173	0.179	0.862
'TXLM'	2005.577	2019.4141	-1.232	-0.51	-4.686	0.194	0.168	0.888

'TXLQ'	2013.0568	2019.4141	-2.044	-0.855	-0.298	0.308	0.381	1.196
'TXMG'	2013.306	2019.4141	0.398	-0.448	-5.668	0.308	0.273	1.368
'TXNV'	2012.46	2019.4141	1.893	0.308	-4.066	0.213	0.264	1.235
'TXPH'	2015.3101	2019.4141	-1.077	-1.384	-2.799	0.592	0.558	2.359
'TXPT'	2011.2608	2019.4141	-0.962	-2.058	-6.405	0.343	0.489	1.321
'TXPV'	2010.2888	2019.4141	0.32	0.174	-0.755	0.234	0.226	1.175
'TXRN'	2015.2033	2019.4141	-0.826	0.947	-2.778	0.397	0.409	2.069
'TXRO'	2005.577	2011.4387	-4.986	4.137	-11.777	1.524	1.012	3.361
'TXRS'	2011.1211	2019.4141	-0.481	0.434	-3.415	0.233	0.227	1.072
'TXSP'	2016.4517	2019.4141	0.515	-0.551	2.457	1.052	1.494	7.852
'TXTG'	2015.4634	2019.4141	-0.627	-0.148	-3.276	0.551	0.519	2.311
'TXWH'	2010.423	2019.4141	0.06	0.702	-5.337	0.23	0.235	1.046
'TXWI'	2015.4771	2019.4141	0.159	-3.785	-3.427	0.436	0.53	1.998
'TXWN'	2015.0007	2019.4141	-0.99	-0.395	-2.205	0.358	0.489	1.968
'UH01'	2012.742	2019.4114	-0.917	1.19	-1.787	0.322	0.444	1.346
'UH02'	2015.0007	2019.3593	-1.213	1.094	-5.652	0.377	0.427	2.162
'UHC0'	2014.1355	2019.1239	3.904	-7.049	-4.815	0.774	1.126	1.612
'UHC1'	2014.1355	2019.1239	-3.521	-3.409	-3.937	0.597	0.576	1.434
'UHC2'	2014.1355	2019.1239	-0.529	-0.919	-4.313	0.364	0.432	1.442
'UHC3'	2014.1355	2019.1239	-0.574	-0.093	-5.613	0.46	0.444	1.418
'UHCL'	2014.2396	2019.4114	1.339	-0.877	0.473	0.721	1.082	1.591
'UHCR'	2014.1218	2019.1184	-1.773	-0.029	-9.313	0.455	0.617	1.503
'UHDT'	2013.5606	2019.4114	-1.59	1.269	-2.016	0.391	0.344	1.412
'UHEB'	2014.5927	2019.4114	-0.747	0.885	-3.036	0.32	0.346	1.594
'UHEP'	2014.3628	2019.3922	-2.533	0.977	-1.874	0.486	0.439	1.631
'UHF1'	2014.3874	2019.4114	-1.008	1.192	-7.388	0.494	0.53	2.963
'UHJF'	2014.3874	2019.4114	-3.075	1.388	-4.708	0.433	0.738	2.342
'UHL1'	2014.3546	2019.4114	1.012	-0.086	3.313	1.252	1.412	1.807
'UHRI'	2014.3272	2019.4114	-2.271	1.033	-3.679	0.594	0.392	1.755
'UHSL'	2014.1821	2019.4114	-1.402	0.496	-3.691	0.416	0.365	1.62
'UHWL'	2014.3546	2019.3812	-3.796	0.086	-1.563	0.629	0.71	1.54
'UTEX'	2012.4928	2019.4114	-2.72	3.393	-10.272	0.425	0.621	1.664
'WCHT'	2013.2923	2019.4114	-0.536	2.641	-10.886	0.494	0.594	1.884
'WDVW'	2013.3169	2019.4114	-1.723	2.507	-6.714	0.355	0.535	1.538
'WEPD'	2014.0753	2019.4114	-2.806	1.671	3.603	0.46	0.501	1.507
'WHCR'	2014.7762	2019.4114	-2.032	-1.036	-3.058	0.422	0.482	2.257
'ZHU1'	2003.039	2019.4141	-0.229	0.828	-8.967	0.168	0.209	0.824

List of GPS stations processed independently using a least-squares trend.

Station	Longitude	Latitude	Easting (cm/yr)	Northing (cm/yr)	Vertical (cm/yr)	Type

1	-95.57693919	30.35301453	0.233	-0.805	0.798	PAM
2	-95.57885656	30.3530145	-0.258	-0.328	1.080	PAM
3	-95.42432721	30.29111078	-0.301	-0.686	0.841	PAM
4	-95.73022264	30.19342937	0.566	0.682	0.848	PAM
5	-95.73114667	30.19342935	0.037	1.116	0.507	PAM
6	-95.5921887	30.18483271	0.291	-0.894	-0.646	PAM
7	-95.58681102	30.18483271	-0.197	-0.738	-0.846	PAM
8	-95.48999306	30.19480793	-0.153	0.839	0.704	PAM
9	-95.48813	30.19480789	0.151	1.028	0.379	PAM
10	-95.45894483	30.19897085	-0.022	0.574	0.940	PAM
11	-95.45395597	30.19897087	0.177	0.503	0.964	PAM
12	-95.6152969	30.09116232	0.278	1.022	-0.393	PAM
13	-95.60780139	30.09116236	0.271	0.877	-0.658	PAM
14	-95.42354439	30.08955321	-0.178	-0.279	1.048	PAM
15	-95.41982944	30.08955331	-0.178	-0.144	1.075	PAM
16	-95.2424857	30.14703	-0.122	1.081	0.119	PAM
17	-95.10694361	30.10646155	-0.169	0.457	-0.979	PAM
18	-95.26307532	30.05969828	-0.176	0.151	1.074	PAM
19	-95.249255	30.05969828	0.113	0.543	0.948	PAM
20	-95.07146542	30.0381248	-0.103	-0.966	-0.513	PAM
21	-95.8652249	30.03216301	-0.277	-0.372	1.093	PAM
22	-95.85036582	29.97903777	0.041	1.110	-0.348	PAM
23	-95.76665413	30.01716567	0.360	0.963	0.511	PAM
24	-95.67171345	30.04535739	-0.145	0.741	0.824	PAM
25	-95.6056575	30.02996919	-0.010	1.054	0.355	PAM
26	-95.60005914	30.02996922	0.011	1.055	-0.353	PAM
27	-95.67822855	29.96493469	-0.136	-1.069	0.259	PAM
28	-95.67155903	29.96493472	0.132	-0.968	0.524	PAM
29	-95.47627157	29.97967694	-0.057	-0.088	-1.092	PAM
30	-95.46883694	29.97967695	-0.064	-0.374	-1.030	PAM
31	-95.41586662	30.00065407	0.156	0.797	-0.736	PAM
32	-95.40153236	30.00065399	0.127	0.191	-1.072	PAM
33	-95.57665211	29.93629584	-0.168	1.087	0.014	PAM
34	-95.8167708	29.90261578	-0.069	0.909	0.650	PAM
35	-95.6868626	29.88013016	-0.180	-0.791	0.747	PAM
36	-95.61662159	29.91187514	-0.170	-0.287	-1.049	PAM
37	-95.60322111	29.91187519	0.108	-0.616	-0.906	PAM
38	-95.50076219	29.88139488	-0.165	-0.757	-0.780	PAM
39	-95.38545335	29.87589578	-0.189	-0.255	1.053	PAM
40	-95.3825245	29.87589577	-0.029	-0.318	1.053	PAM
41	-95.2842013	29.93254509	0.208	0.435	0.992	PAM
42	-95.05728876	29.90802912	0.051	-1.036	0.393	PAM
43	-95.80534789	29.84111797	-0.108	0.655	0.893	PAM

44	-95.82218678	29.76901913	-0.062	1.047	0.348	PAM
45	-95.67188791	29.81849975	0.126	-0.444	0.998	PAM
46	-95.6684125	29.81849978	0.158	-0.245	1.060	PAM
47	-95.61338321	29.82081159	0.124	-0.717	-0.824	PAM
48	-95.60065007	29.8208116	-0.053	-0.896	-0.635	PAM
49	-95.58591021	29.79120761	0.155	-0.793	0.746	PAM
50	-95.58362028	29.79120756	-0.069	-0.545	0.952	PAM
51	-95.49320308	29.78319202	0.215	-0.633	0.882	PAM
52	-95.48141583	29.78319203	0.127	-0.401	1.023	PAM
53	-95.17673576	29.85202488	-0.241	0.601	-0.908	PAM
54	-95.17720049	29.79418734	0.297	1.080	0.075	PAM
55	-95.0343892	29.8014697	-0.196	-0.922	-0.605	PAM
56	-95.02878694	29.80146975	0.203	-1.102	-0.011	PAM
57	-94.85604269	29.84834263	-0.279	0.413	0.996	PAM
58	-94.84594229	29.84834268	0.101	0.491	0.994	PAM
59	-96.01566323	29.73869637	0.123	1.090	0.126	PAM
60	-96.00232937	29.73869651	-0.049	0.827	-0.730	PAM
61	-95.97244064	29.67539266	0.011	0.159	1.092	PAM
62	-95.97418738	29.59328828	0.149	1.020	-0.398	PAM
63	-95.90191652	29.68925149	-0.020	1.100	0.112	PAM
64	-95.81955353	29.68591314	-0.147	-0.983	0.479	PAM
65	-95.72181855	29.6840606	0.021	0.416	1.019	PAM
66	-95.71729694	29.68406061	0.167	0.452	0.989	PAM
67	-95.63534888	29.73248722	-0.145	-0.873	-0.656	PAM
68	-95.63296917	29.73248722	0.175	-0.958	-0.516	PAM
69	-95.74041602	29.61665973	-0.058	-0.900	-0.634	PAM
70	-95.733245	29.61665972	0.018	-1.041	-0.363	PAM
71	-95.59686484	29.63039197	0.177	0.951	-0.527	PAM
72	-95.58278898	29.63039222	0.087	0.368	-1.035	PAM
73	-95.47550241	29.66190812	0.217	0.845	-0.685	PAM
74	-95.46427778	29.66190828	0.224	0.529	-0.948	PAM
75	-95.33928306	29.64524778	-0.282	1.082	0.056	PAM
76	-95.32924917	29.64524783	0.077	1.116	-0.036	PAM
77	-95.23120503	29.73555949	0.235	-0.231	1.092	PAM
78	-95.22295415	29.64927473	0.133	-0.918	-0.630	PAM
79	-95.21223361	29.64927467	-0.077	-1.088	-0.261	PAM
80	-95.15959559	29.71018218	0.059	0.876	0.703	PAM
81	-95.03056898	29.75779264	0.170	0.746	0.826	PAM
82	-95.01154056	29.75779261	-0.044	1.070	0.347	PAM
83	-94.91763189	29.75121935	-0.331	-1.004	-0.400	PAM
84	-94.91105047	29.75121938	0.023	-1.022	-0.481	PAM
85	-95.04133286	29.66822356	0.068	-1.115	-0.158	PAM
86	-95.02801359	29.66822356	-0.215	-1.072	-0.279	PAM

87	-95.1010125	29.63070579	-0.335	-0.298	1.041	PAM
88	-95.0942643	29.63070579	-0.193	-0.421	1.034	PAM
89	-95.85479107	29.53176617	0.083	0.641	0.892	PAM
90	-95.85118472	29.53176611	0.056	0.777	0.779	PAM
91	-95.79917167	29.56638935	0.151	-1.081	0.142	PAM
92	-95.78474528	29.56638528	0.155	-0.731	0.809	PAM
93	-95.70730668	29.54060279	-0.079	0.957	-0.542	PAM
94	-95.71493193	29.48476476	0.025	0.473	-0.997	PAM
95	-95.6441071	29.47365563	0.003	1.072	-0.264	PAM
96	-95.63228398	29.47365568	-0.177	0.760	-0.781	PAM
97	-95.5474124	29.50786559	-0.203	0.773	-0.767	PAM
98	-95.53139722	29.50786561	0.148	0.134	-1.089	PAM
99	-95.52724526	29.54446293	0.025	1.006	0.460	PAM
100	-95.51482306	29.54446296	-0.190	1.038	-0.333	PAM
101	-95.46249832	29.49329485	-0.112	1.009	-0.441	PAM
102	-95.44795889	29.49329489	-0.003	0.684	-0.870	PAM
103	-95.4378823	29.44563461	-0.112	1.020	0.421	PAM
104	-95.43080833	29.44563469	-0.206	1.062	0.246	PAM
105	-95.3120749	29.5454668	0.084	0.517	0.979	PAM
106	-95.29709665	29.54546684	0.035	0.920	0.620	PAM
107	-95.22356765	29.48991212	-0.062	-1.098	-0.203	PAM
108	-95.21254306	29.48991219	-0.113	-1.099	0.175	PAM
109	-95.15223578	29.5386185	0.065	0.022	1.122	PAM
110	-95.14521815	29.53861854	0.242	0.363	1.036	PAM
111	-95.1698031	29.5557654	-0.258	-1.037	-0.339	PAM
112	-95.16221513	29.55576543	-0.211	-1.101	-0.022	PAM
113	-95.16513506	29.57809857	0.309	-0.935	0.546	PAM
114	-95.14500056	29.57809858	-0.243	-0.659	0.880	PAM
115	-95.08244045	29.47261518	-0.193	-1.114	-0.007	PAM
116	-95.06114238	29.47261514	-0.255	-1.080	0.213	PAM
117	-95.01324324	29.53290549	-0.256	-0.072	-1.103	PAM
118	-94.99402326	29.5329054	0.095	-0.739	-0.856	PAM
119	-95.01555002	29.58313747	-0.041	-0.356	1.080	PAM
120	-94.99380611	29.58313751	0.261	0.443	1.014	PAM
121	-94.94162505	29.49417744	-0.099	-1.119	0.201	PAM
122	-94.92677806	29.49417733	-0.101	-0.941	0.637	PAM
123	-95.84837822	29.39801979	-0.148	0.980	-0.483	PAM
124	-95.73134755	29.29565914	-0.196	-0.536	-0.948	PAM
125	-95.71530472	29.29565911	0.056	-1.082	-0.226	PAM
126	-95.45847729	29.25773073	0.239	-0.532	0.954	PAM
127	-95.44627161	29.25773074	0.054	-0.466	1.015	PAM
128	-95.37030522	29.29685053	0.305	0.879	-0.636	PAM
129	-95.3618962	29.29685049	-0.012	0.919	-0.651	PAM

130	-95.2781482	29.34258044	0.204	-1.095	-0.163	PAM
131	-95.26182046	29.34258042	-0.299	-0.851	0.674	PAM
132	-95.18152126	29.26241364	0.005	-0.080	1.133	PAM
133	-95.16075706	29.2624136	-0.217	0.031	1.114	PAM
134	-95.04546766	29.36089036	0.335	1.060	-0.209	PAM
135	-95.02772528	29.36089053	0.093	0.583	-0.965	PAM
136	-95.02071249	29.33452157	-0.346	-0.241	-1.059	PAM
137	-95.01024535	29.33452156	-0.261	-0.207	-1.090	PAM
138	-94.91777856	29.33508074	-0.160	-1.120	0.121	PAM
139	-94.91032339	29.33508071	-0.182	-1.065	0.359	PAM
140	-94.7015285	29.4224457	0.347	-1.015	0.374	PAM
141	-95.67676173	29.05807639	-0.268	0.750	0.812	PAM
142	-95.66112954	29.05807638	0.162	1.115	0.159	PAM
143	-95.47127028	29.03479898	0.321	0.291	-1.050	PAM
144	-95.46106679	29.03479899	0.120	-0.504	-1.011	PAM
145	-95.11059615	29.09324702	0.361	0.730	-0.801	PAM
146	-95.09351417	29.09324706	-0.313	0.121	-1.091	PAM
147	-94.93832664	29.21031551	0.225	0.603	0.941	PAM
148	-94.92686667	29.2103155	0.023	0.837	0.773	PAM
ALEF	-95.635052	29.691833	0.120	0.951	0.538	CORS
ANG1	-95.48507419	29.30147522	0.235	1.069	-0.187	CORS
AULT	-95.744665	29.997772	-0.010	1.021	-0.474	CORS
CFHS	-95.631934	29.919234	-0.198	0.942	0.543	CORS
CFJV	-95.55584	29.881648	-0.071	1.090	0.124	CORS
CMFB	-95.728793	29.681363	0.061	-0.903	0.627	CORS
COTM	-94.998199	29.39384	0.286	0.739	-0.800	CORS
CSTA	-95.511599	29.795872	0.160	-0.754	0.783	CORS
CSTE	-95.510738	29.795637	-0.080	-0.412	1.018	CORS
DEN1	-95.258008	29.510413	-0.261	1.044	0.305	CORS
DEN2	-95.253958	29.504882	-0.209	-0.391	1.027	CORS
DEN3	-95.254638	29.493718	-0.198	1.005	-0.453	CORS
DISD	-95.740414	29.289266	0.036	-0.194	-1.088	CORS
DMFB	-95.583739	29.622647	-0.161	-1.042	0.310	CORS
FSFB	-95.630447	29.556183	-0.157	-0.153	1.078	CORS
GSEC	-95.528092	30.197301	0.152	0.828	0.742	CORS
HCC1	-95.561221	29.787869	-0.098	0.503	0.971	CORS
HCC2	-95.562019	29.788385	-0.138	-0.746	0.795	CORS
HPEK	-95.715723	29.754878	0.068	1.063	-0.287	CORS
HSMN	-95.469616	29.80035	-0.086	-1.085	-0.137	CORS
KKES	-95.594934	29.850327	0.166	-0.775	-0.763	CORS
KPCD	-95.923971	29.926014	0.276	0.961	0.547	CORS
ICI1	-95.442498	29.807472	-0.237	-1.062	-0.224	CORS
MDWD	-95.595211	29.771379	-0.148	-0.531	0.951	CORS

ME01	-95.275714	29.60754	-0.158	0.941	0.568	CORS
MEPD	-95.239591	29.658082	-0.203	-1.054	0.297	CORS
MRHK	-95.745145	29.804143	0.049	-0.791	0.782	CORS
NASA	-95.096219	29.551953	-0.249	1.008	0.452	CORS
OKEK	-95.803313	29.725025	0.200	-0.682	0.850	CORS
PA00	-95.152235	29.538619	0.065	0.022	1.122	CORS
PWES	-95.51057	30.198988	0.178	-1.082	0.194	CORS
RDCT	-95.494717	29.810418	-0.107	-0.157	-1.081	CORS
RPFB	-95.513654	29.48417	-0.161	-0.889	0.627	CORS
SESG	-95.429619	29.987468	0.013	0.948	-0.553	CORS
SHSG	-95.430054	30.053611	-0.197	-0.079	1.081	CORS
SISD	-96.173876	29.762193	-0.299	-0.569	0.991	CORS
SPBH	-95.515036	29.801905	0.115	-0.063	1.090	CORS
TDAM	-94.816952	29.314057	-0.087	-1.029	-0.361	CORS
THSU	-95.339906	29.714008	-0.002	0.648	0.901	CORS
TSFT	-95.479964	29.806286	-0.105	-0.726	0.820	CORS
TXHS	-95.555509	29.716078	-0.017	1.085	0.178	CORS
TXLQ	-94.952851	29.357965	0.299	-0.751	-0.778	CORS
TXMG	-95.963553	28.982896	0.007	0.836	-0.720	CORS
TXTG	-95.297383	29.897517	-0.015	-1.098	0.068	CORS
TXWN	-96.092053	29.328757	0.026	-0.365	1.043	CORS
UH01	-95.345395	29.722465	0.147	0.569	-0.930	CORS
UHC0	-95.04385247	29.39037472	-0.271	1.100	0.035	CORS
UHC1	-95.04396558	29.39036642	-0.306	1.089	0.076	CORS
UHC2	-95.04392908	29.39036864	-0.295	1.093	0.061	CORS
UHC3	-95.04389056	29.39037147	-0.283	1.096	0.049	CORS
UHCL	-95.104165	29.577737	-0.143	1.065	0.271	CORS
UHCR	-95.75677	29.728071	-0.113	1.077	-0.197	CORS
UHDT	-95.359441	29.76596	-0.264	-0.198	1.068	CORS
UHEB	-96.066039	29.526312	0.041	0.950	-0.574	CORS
UHEP	-95.327123	29.719465	0.082	0.487	-0.984	CORS
UHF1	-95.483098	30.23625	-0.250	0.447	-0.989	CORS
UHJF	-95.48307	30.236273	-0.268	0.495	-0.966	CORS
UHL1	-94.978463	30.057646	-0.094	0.650	0.877	CORS
UHRI	-95.402517	29.719227	0.105	0.800	0.744	CORS
UHSL	-95.651539	29.574673	0.035	1.026	0.406	CORS
UHWL	-94.978434	30.057639	-0.095	0.653	0.873	CORS
UTEX	-95.567817	29.785887	0.083	-0.880	-0.652	CORS
WDVW	-95.533073	29.790389	-0.009	0.512	-0.973	CORS
WEPT	-95.22873319	29.68773042	-0.293	-1.082	-0.032	CORS
WHCR	-95.505396	30.194322	0.025	1.021	0.439	CORS

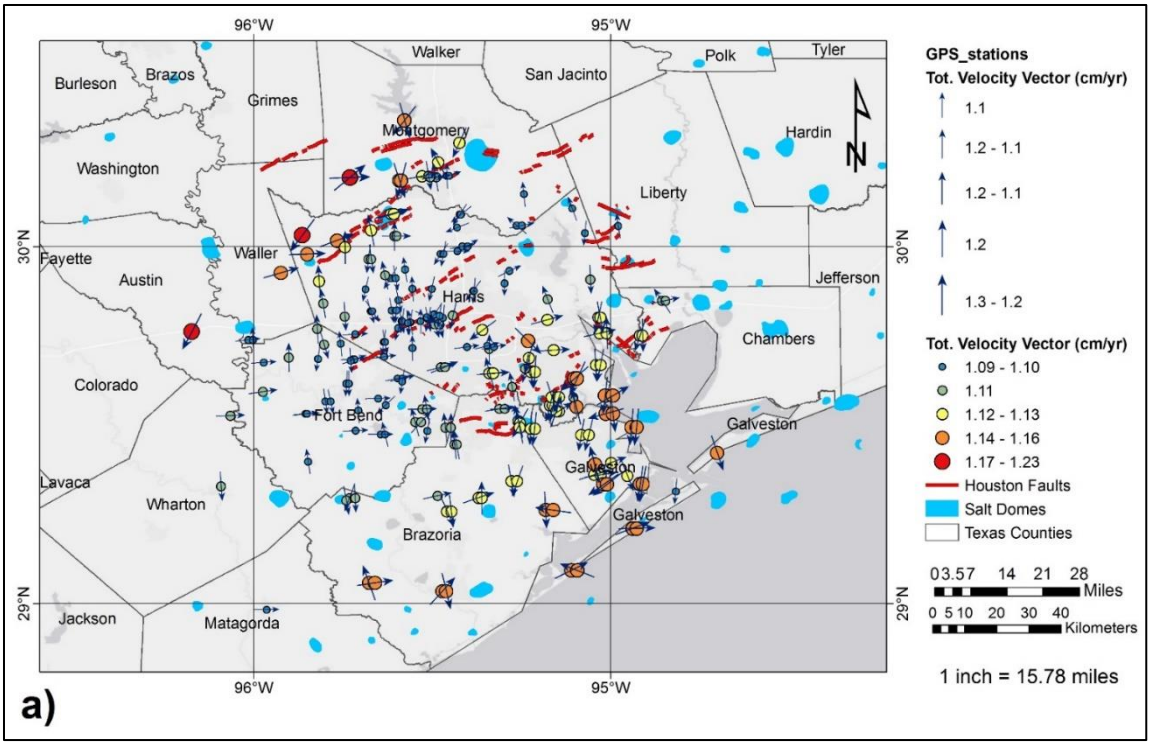
96°W
95°W
30°N
29°N
Walker
Polk
Tyler
Burleson
Brazos
San Jacinto
Grimes
Montgomery
Hardin
Washington
Liberty
Waller
Fayette
Austin
Jefferson
Harris
Chambers
Colorado
Fort Bend
Galveston
Lavaca
Wharton
Brazoria
Jackson
Matagorda
GPS_stations
Tot. Velocity Vector (cm/yr)
1.1
1.2 - 1.1
1.2 - 1.1
1.2
1.3 - 1.2
Tot. Velocity Vector (cm/yr)
1.09 - 1.10
1.11
1.12 - 1.13
1.14 - 1.16
1.17 - 1.23
Houston Faults
Salt Domes
Texas Counties
0 3.5 7 14 21 28 Miles
0 5 10 20 30 40 Kilometers
1 inch = 15.78 miles
a)

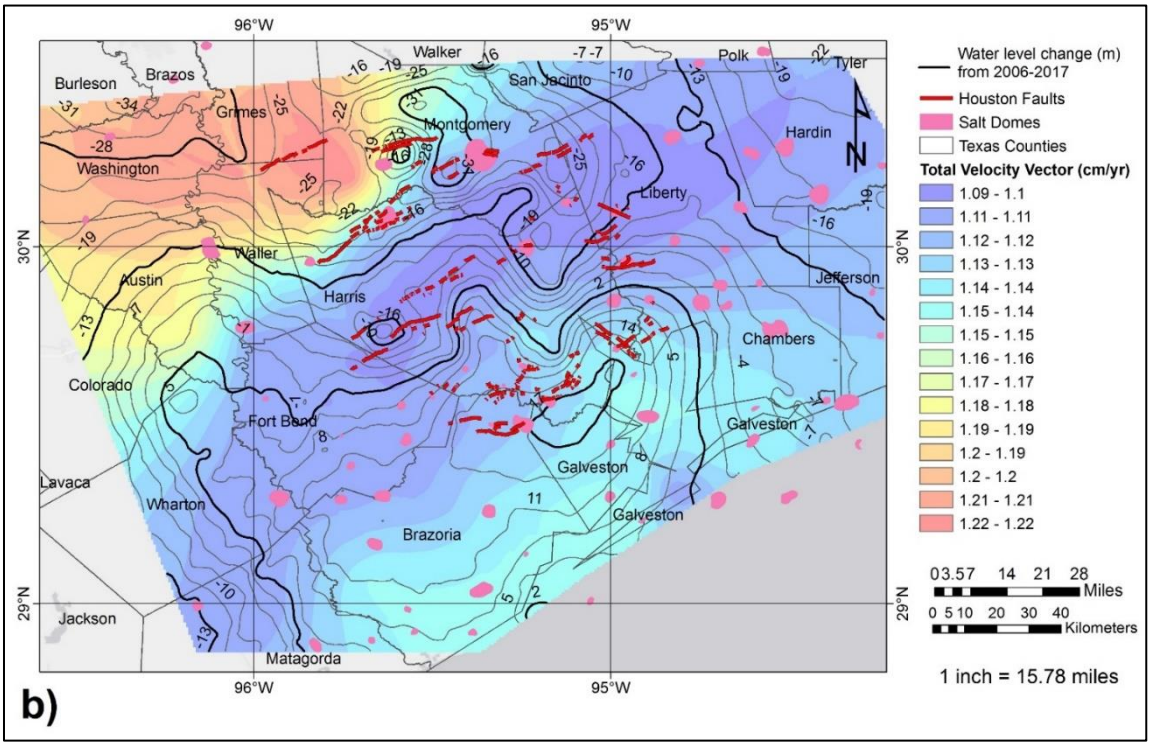
96°W
95°W
30°N
29°N
Walker
Polk
Tyler
Burleson
Brazos
San Jacinto
Grimes
Montgomery
Hardin
Washington
Liberty
Waller
Austin
Jefferson
Harris
Chambers
Colorado
Fort Bend
Galveston
Lavaca
Wharton
Brazoria
Jackson
Matagorda
Water level change (m) from 2006-2017
Houston Faults
Salt Domes
Texas Counties
Total Velocity Vector (cm/yr)
1.09 - 1.1
1.11 - 1.11
1.12 - 1.12
1.13 - 1.13
1.14 - 1.14
1.15 - 1.14
1.15 - 1.15
1.16 - 1.16
1.17 - 1.17
1.18 - 1.18
1.19 - 1.19
1.2 - 1.19
1.2 - 1.2
1.21 - 1.21
1.22 - 1.22
0 3.5 7 14 21 28 Miles
0 5 10 20 30 40 Kilometers
1 inch = 15.78 miles
b)

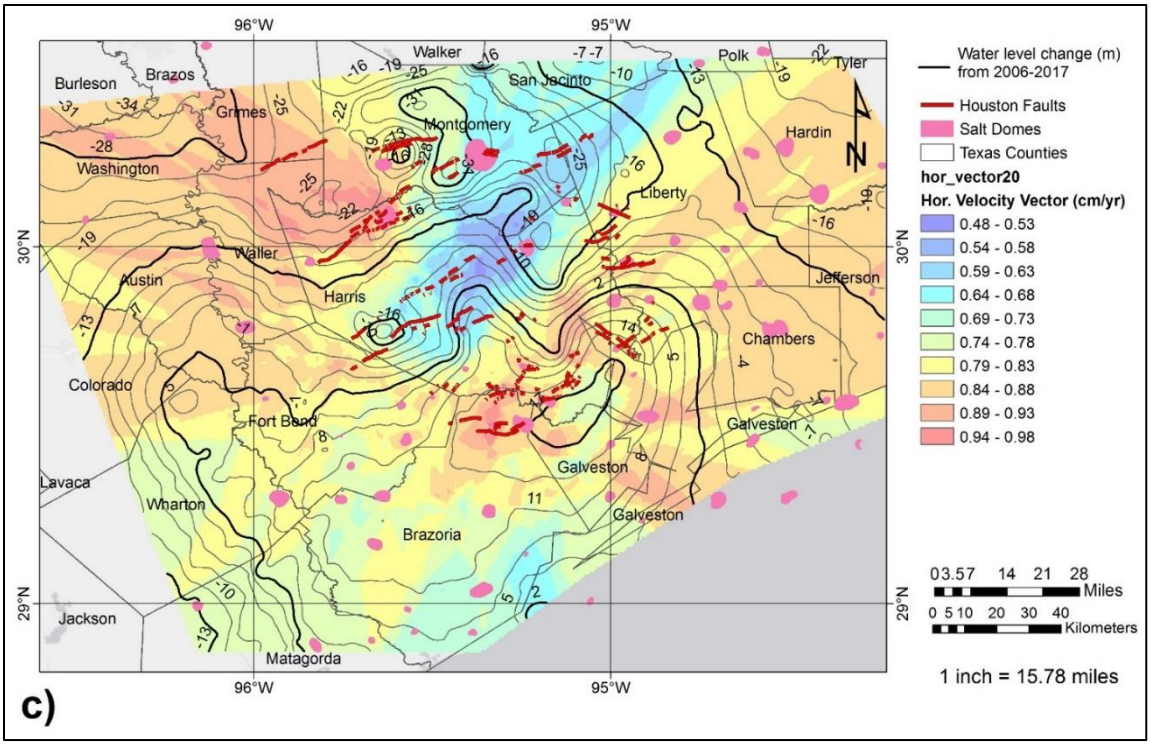

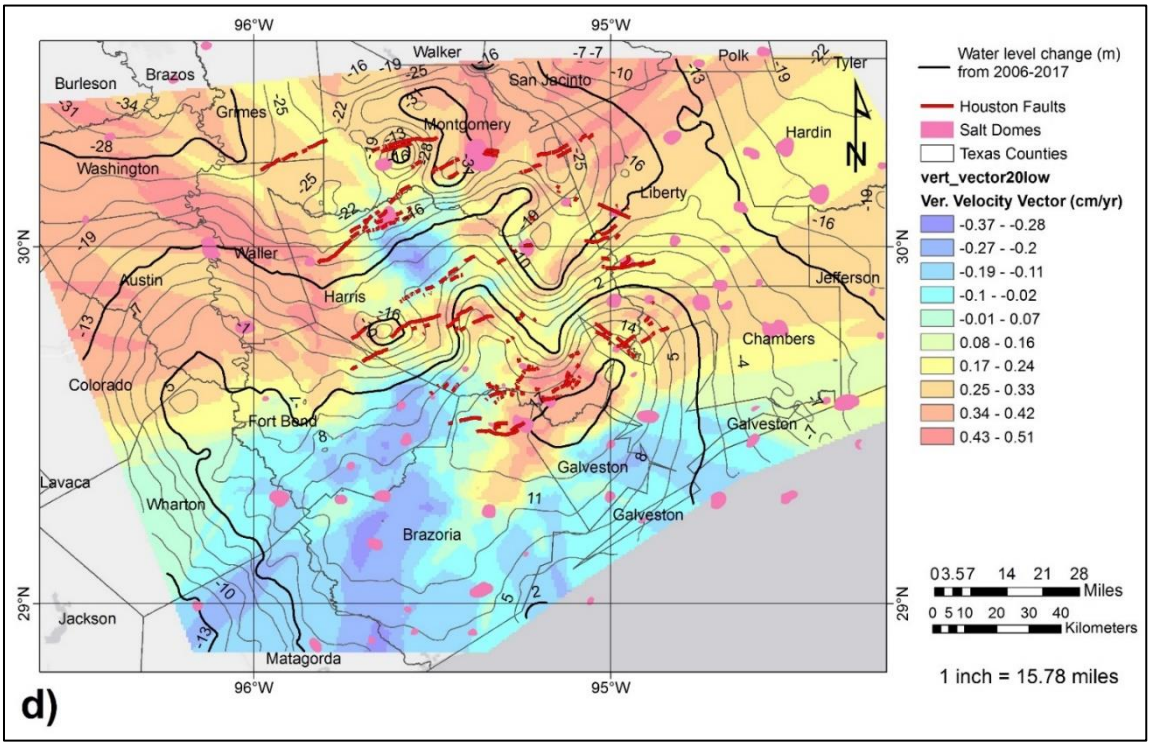

Figure I: Surfaces in sub-figures a-d are generated using a 20-point ordinary Kriging interpolation. GPS data consists of both CORS and PAM stations from 1990 to September of 2017 which were independently processed using least-squares fit. Ground water data changes were calculated using a time-series analysis approach between 2006 to 2017. ***a)*** *Plotted rotated GPS total velocity vectors over the Houston area; vectors highlight southern salt dome movement and fault motion.* ***b)*** *GPS Total Velocity Vector Surface*

*(cm/yr) with plotted GPS stations and GPS vectors. c**)** GPS Horizontal Velocity Vector Surface (cm/yr); area of low horizontal motion is concentrated in northern Harris County which corresponds to a decrease in the water table from 2006-2017. Areas of high horizontal motion are concentrated over salt domes, particularly in the south over the Hasting salt dome/League City. Here horizontal motion is ~10 mm/yr along a Southern track. d**)** GPS Vertical Velocity Vector Surface (cm/yr); it shows the best water level change correlation, uplift over salt domes of up to 5 mm/yr, and increasing vertical displacement over the Long Point-Eureka Heights faults system of ~2.5 mm/yr associated with an increase in the water level. Rather than causing increased subsidence, the added water is likely acting as a lubricant to the fault zone and aiding rocks slip past one another as differential pressure is decreased.*

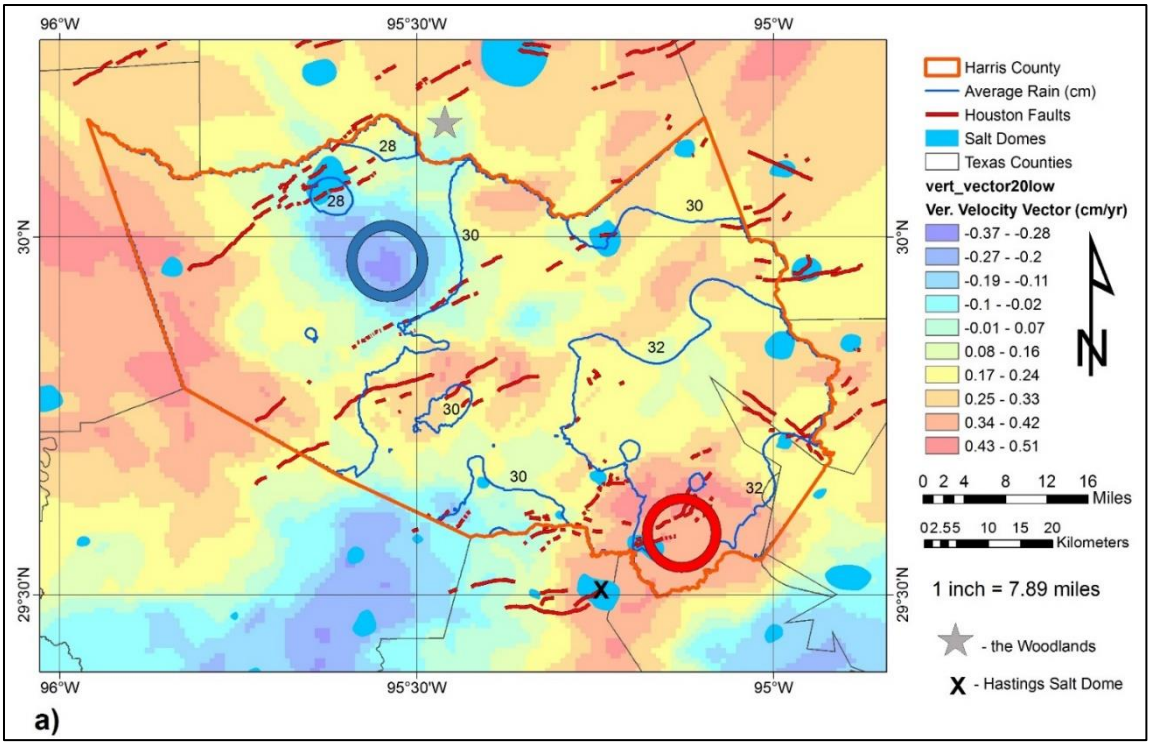

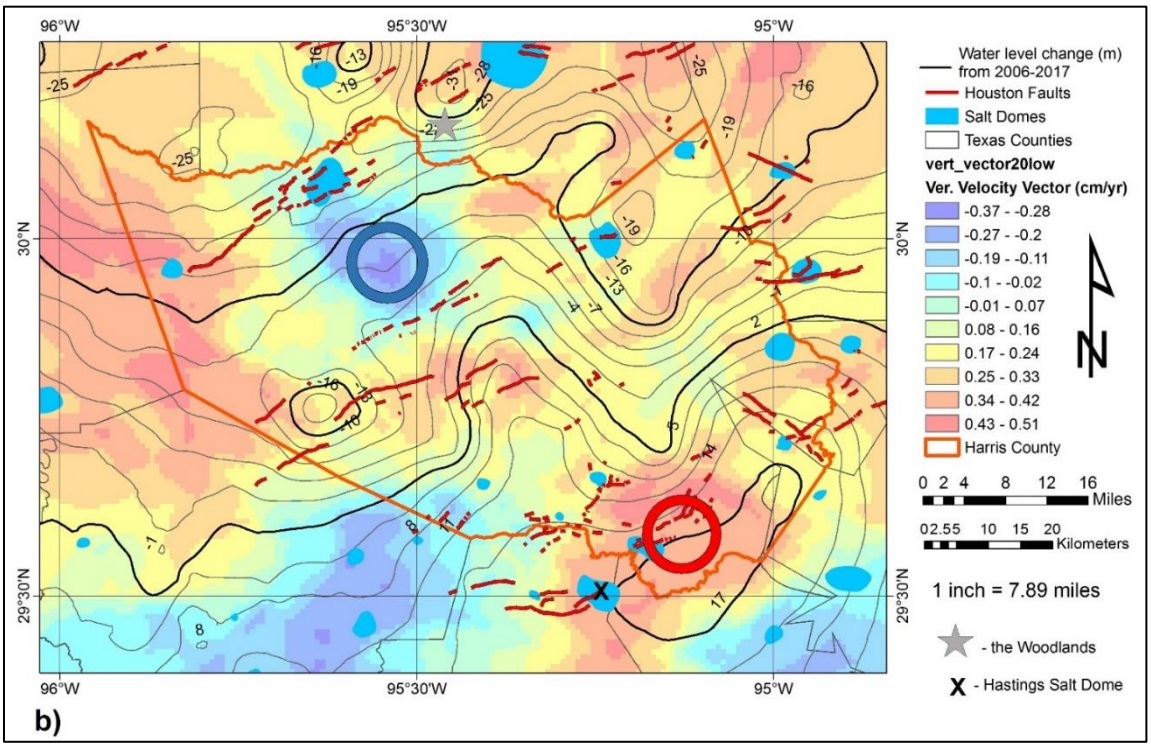

Figure II: GPS Vertical Velocity Vector Surface (cm/yr) generated though independent processing along with Water Level Change contours (m); X over Hasting salt dome/oil field, gray star over Woodlands area. ***a)*** *Average rain from 2011-2016 showing less rain/smaller loading capacity over northern Harris County (blue circle) and more rain/higher loading capacity over League City/Hastings salt dome (red circle).* ***b)*** *Ground*

water level change contours from 2006-2017 show uplifting area in League City/Hastings salt dome (red circle) where salt dome movement ranges from 2.6-5 mm/yr. Area between Addick's Conroe and Long-Point-Eureka-Heights Fault systems is likely showing positive uplift due to faults, but uplift is hard to quantify. Northern Harris County (blue circle) is undergoing non-reversible deformation and subsiding at ~3.7mm/yr. The Woodlands (gray star) is similar to League City and also affected by salt domes whose uplift of up to 5mm/yr is counteracting the 1mm/yr subsidence. In the future this area may resemble northern Harris County.

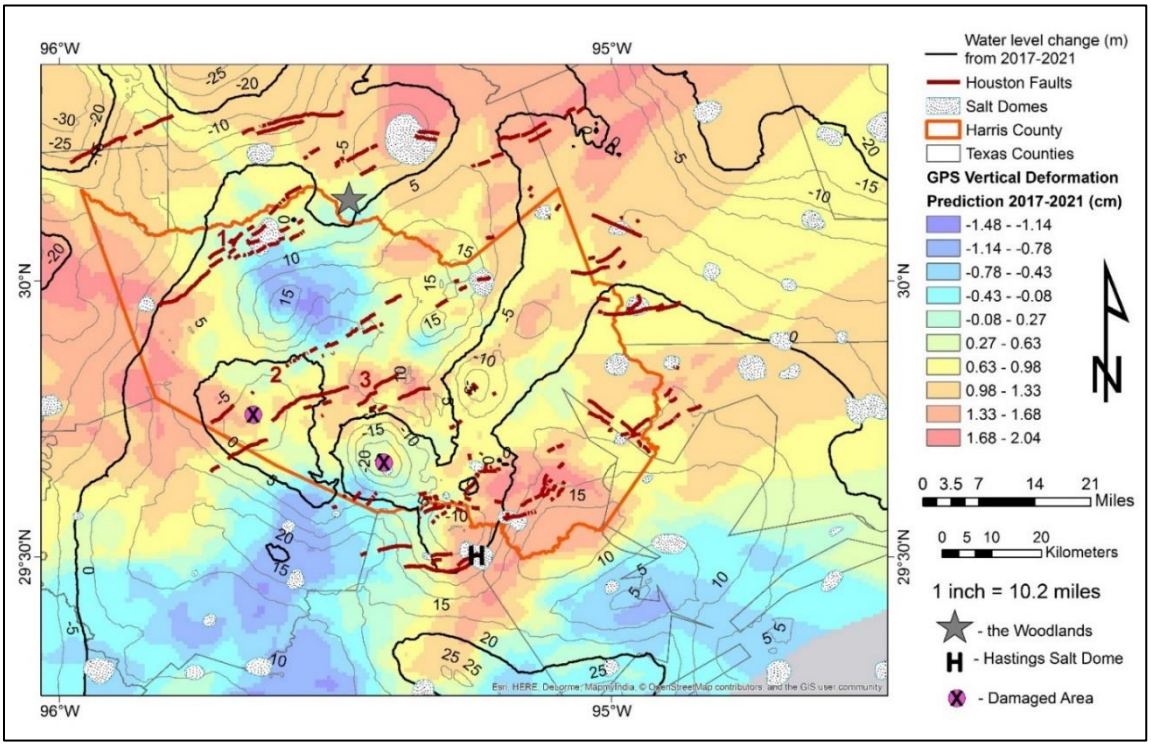

Figure III: Predicted surface deformation using GPS data independently processed and groundwater level change from 2017-2021, where H is over Hastings Salt Dome/Oil Field, star over Woodland area, cross-hair over damaged area in southwest Harris County, and three main fault systems: 1) Hockley-Conroe Fault System, 2) Addick's Fault System, and 3) the Long Point-Eureka Heights Fault System. The 4-year prediction shows a continued decrease in the water level over the Woodlands area and various parts of Harris County. Deformation is predicted to increase significantly over the damaged areas in southwest Harris County.